Dynamics and Scaling of Self-Excited Passive Vortex Generators for Underwater Propulsion

Thesis by

Robert Wells Whittlesey

In Partial Fulfillment of the Requirements

for the Degree of

Doctor of Philosophy

California Institute of Technology

Pasadena, California

2013

(Defended May 14th, 2013)

Dedicated to my dad

Great is our LORD *and mighty in power;*
his understanding has no limit.

Psalm 147:5

Acknowledgments

Let me begin by saying that my presence at Caltech has never been by my own doing, but by His. I have been thoroughly blessed in my time at Caltech, both in and out of lab, and I feel extremely fortunate to have been able to conduct research here.

Many, many thanks go to my advisor, John. I cannot believe sometimes the level of patience he must have mustered to edit my papers (perhaps yet another act of God), but I enjoyed being his student my entire time at Caltech. His level of intellect coupled with his humor makes him a great individual, and I have truly appreciated working alongside him. I thank the committee members, Mory, Beverley, and Professor Shepherd, for giving their time to meet with me and provide their comments on my work. I would also like to thank Professor Dan Stilwell and his graduate student Brian McCarter for generously lending the AUV used in these experiments and assisting with its use. The use of their AUV saved me countless hours of designing and manufacturing my own.

I thank my colleagues at Caltech for their friendship and encouragement during the sometimes exciting, sometimes painful, ride that defines graduate school: Clara O'Farrell, Daniel and Claire Thomas, Daniel Araya, Monica Martinez-Ortiz, Matthias Kinzel, Janna Nawroth, Kelly Sutherland, Nicholaus Parziale, Jason Rabinovitch, Mumu Xu, Jacob Notbohm, Keith Patterson, Sebastian Liska, et al.

I also thank my in-laws, Adonijah and Benedicta Ogbonnaya. To my father-in-law,

thank you for lending your wife. To my mother-in-law, I have absolutely no idea how our family would function without you. Thank you so very very much for taking care of our daughter, Zikora. You have such an enthusiasm that brings a smile to so many people. This thesis would surely have not been completed (or rather, would have been only fractionally as good) without your help.

My family, of David, my mom, Susan, and dad, Tom, I thank you for putting up with me venturing away from home when I first went to undergrad, but I think you have somewhat benefited by Caltech's convenient location for vacations. I would like to dedicate this thesis in memory of my dad, who unexpectedly passed away nearly two years ago. I know he was always proud of my accomplishments, both big and small, but I just know he would have been over the moon to see me graduate. I also thank you mom and dad for helping develop my scientific skills as a kid—allowing me to take apart all sorts of things just to see what was inside, to blow circuits (on occasion), to play in the dirt just because, and to read and read and read.

To my daughter, Zikora, you probably will not remember this time, but thank you for letting daddy go to work each day! Your smile and giggles are so cute, and I love you so very much!

Lastly, I would like to thank my wife, Amara. You are such an amazing blessing to me and our family. Your knowledge is vast, your caring heart is without end, and your love is wonderful. I am so amazingly blessed that you call me your husband, and it brings me great joy that we get to be together until death parts us. I thank you so very much for your love and encouragement during my graduate studies. Thank you for giving us our beautiful daughter and being a wonderful mother. You are my wife of noble character—you are worth far more than rubies.

Abstract

A series of experiments was conducted on the use of a device to passively generate vortex rings, henceforth a passive vortex generator (PVG). The device is intended as a means of propulsion for underwater vehicles, as the use of vortex rings has been shown to decrease the fuel consumption of a vehicle by up to 40% (Ruiz 2010).

The PVG was constructed out of a collapsible tube encased in a rigid, airtight box. By adjusting the pressure within the airtight box while fluid was flowing through the tube, it was possible to create a pulsed jet with vortex rings via self-excited oscillations of the collapsible tube. A study of PVG integration into an existing autonomous underwater vehicle (AUV) system was conducted. A small AUV was used to retrofit a PVG with limited alterations to the original vehicle. The PVG-integrated AUV was used for self-propelled testing to measure the hydrodynamic (Froude) efficiency of the system. The results show that the PVG-integrated AUV had a 22% increase in the Froude efficiency using a pulsed jet over a steady jet. The maximum increase in the Froude efficiency was realized when the formation time of the pulsed jet, a nondimensional time to characterize vortex ring formation, was coincident with vortex ring pinch-off. This is consistent with previous studies that indicate that the maximization of efficiency for a pulsed jet vehicle is realized when the formation of vortex rings maximizes the vortex ring energy and size.

The other study was a parameter study of the physical dimensions of a PVG. This study

was conducted to determine the effect of the tube diameter and length on the oscillation characteristics such as the frequency. By changing the tube diameter and length by factors of 3, the frequency of self-excited oscillations was found to scale as $f \sim D_0^{-1/2} L_0^0$, where D_0 is the tube diameter and L_0 the tube length. The mechanism of operation is suggested to rely on traveling waves between the tube throat and the end of the tube. A model based on this mechanism yields oscillation frequencies that are within the range observed by the experiment.

Contents

List of Figures

List of Tables

Nomenclature

Latin Symbols

A	tube cross-sectional area [m^2], page 28
A_0	tube cross-sectional area without external pressure [m^2], page 28
A_V	cross-sectional area of AUV [m^2], page 53
A_{out}	area of the jet nozzle exit [m^2], page 7
a	stroke amplitude [m], page 2
C_D	drag coefficient, page 53
C_P	pressure coefficient, page 90
C_p	power coefficient from Ruiz, Whittlesey & Dabiri (2011), page 7
C_p'	power coefficient from Ruiz (2010), page 69
c	Moens-Korteweg wavespeed [m s^{-1}], page 107
D_0	tube diameter [m], page 17
E	Young's modulus [N m^{-2}], page 17
$\overline{\dot{E}_{ex}}$	rate of shedding of excess kinetic energy [W], page 6

F formation number, page 3

$\overline{F}_T$ time-averaged jet thrust [N], page 6

F_D drag force [N], page 38

f frequency [Hz], page 2

h tube-wall thickness [m], page 17

I electric current [A], page 7

J PVG chamber height and depth [mm], page 81

K PVG chamber length [mm], page 81

K_P bending stiffness parameter for finite tubes [N m^2], page 83

$K_{P,\infty}$ bending stiffness parameter for infinite tubes [N m^2], page 83

L length of piston travel [m], page 3

L_0 tube length [m], page 16

l_t length from the collapsible tube throat to the downstream end [m], page 108

n azimuthal mode of tube collapse, page 30

$\vec{n}$ outward-facing normal, page 2

P_1 pressure at the upstream end of the collapsible tube [Pa], page 81

P_2 pressure at the downstream end of the collapsible tube [Pa], page 81

P_d driving pressure [N m^2], page 86

P_e chamber pressure [Pa], page 81

P_t transmural pressure [N m^2], page 86

R_v ratio of freestream to jet velocities from Krueger *et al.* (2006), page 50

Re_j nozzle Reynolds number, page 56

S wetted area of vehicle [m^2], page 69

St Strouhal number for animal propulsion, page 2

St' Strouhal number for the PVG, page 157

St'_c Strouhal number based on the Moens-Korteweg wavespeed, page 158

T AUV throttle setting, page 22

T' tube tension [N], page 17

$\hat{t}$ formation time for self-propelled pulsed jets, page 49

$\hat{t}_{GRS}$ vortex ring formation time from Gharib *et al.* (1998), page 48

$\hat{t}_{KDG}$ vortex ring formation time from Krueger, Dabiri & Gharib (2003), page 48

t_p piston discharge time [s], page 48

U_∞ velocity of the vehicle or animal [m s^{-1}], page 2

U_j jet velocity [m s^{-1}], page 6

$\overline{U_p}$ average piston velocity, page 48

V electric voltage [V], page 7

$\overline{V_c}$ average co-flow velocity [m s^{-1}], page 48

V_c chamber volume [m^3], page 25

V_t tube volume [m^3], page 25

Greek Symbols

α' Wormersley number, page 157

α_{xx} added mass coefficient for the vortex ring in the axial direction, page 76

β tube collapse factor (cf. appendix B), page 25

Γ vortex circulation [m^2 s^{-1}], page 2

η Froude efficiency, page 6

η_0 Froude efficiency for τ = 0 s, page 60

$\overline{\eta}_6$ average Froude efficiency for τ = 6 s, page 62

η_P propulsive efficiency (Moslemi & Krueger 2010, 2011), page 6

η_R pulsed jet efficiency from Ruiz *et al.* (2011), page 76

λ ratio of chamber volume to tube volume, page 25

ρ fluid density [kg m^{-3}], page 7

σ Poisson's ratio, page 83

τ PVG chamber fill time [s], page 28

τ_{crit} critical value of τ, page 55

ω vorticity [s^{-1}], page 2

Chapter 1

Introduction

1.1 Vortices in Nature

Nature yields a seemingly unending array of animals that travel through fluid environments by flying and swimming. As animals propel themselves, many create vortices in their wake. These vortices can take many forms and are dependent on the morphology of the generating animal. Flying animals, such as bats, birds, and insects, have vortex rings as a prominent feature in their wake based on experimental observation (Brodsky 1991; Dickinson 1996; Ellington 1978; Hedenström *et al.* 2007; Rayner 1979a, b, 1988; Spedding, Rayner & Pennycuick 1984; Tian *et al.* 2006). Swimming animals such as eels and fish (Bainbridge 1961; Lighthill 1960; Rosen 1959; Wu 1961), frogs (Johansson & Lauder 2004), birds (Johansson & Norberg 2003), and even swimming insects (Brackenbury 2001, 2002, 2003, 2004) have also been reported to have vortex structures in their wake and the locomotive performance of swimming insects is well matched by vortex-based models (Whittlesey 2011).

We can characterize the kinematics of the locomotion of a particular animal by examining the stroke frequency. The frequency of jetting, flapping, rowing, or undulating can be

expressed in nondimensional form as the Strouhal number,

$$St = \frac{fa}{U_\infty}, \tag{1.1}$$

where f is the stroke frequency, a is the stroke amplitude, and U_∞ is the speed of the vehicle or animal. Taylor *et al.* (2003) found that despite the significant differences in size, morphology, and stroke kinematics between insects, birds, bats, sharks, fish, and dolphins, they all cruised in a fairly narrow range of St = 0.2–0.4 with a peak at 0.3. This has been suggested by Dabiri (2009) to be a direct consequence of the vortex structure formation in the wake; specifically, a consequence of wake-structure optimization.

Because of the ubiquity of vortices in the wake of these animals and the suggestion that these vortices may be optimized for efficient propulsion, it is appropriate to consider the consequences of a vortex-dominated wake. However, before we address that, let us first enter into a discussion on some of the fundamentals of vortices and their properties.

1.2 Vortex Pinch-off

The strength of a vortex element is known as the vortex circulation and is defined as

$$\Gamma \equiv \int_Q \omega \cdot \vec{n} \; dQ, \tag{1.2}$$

where Q is the area of integration, ω is the vorticity of the fluid, $\vec{n}$ is the outward-facing normal to the area of integration (Saffman 1995, pg. 8). Gharib *et al.* (1998) showed that there is a limit to the amount of circulation a vortex ring can contain. For their experiments, Gharib *et al.* (1998) created vortex rings using a piston-cylinder arrangement where ejections

of greater amounts of fluid yielded larger vortex rings with increased circulation. However, at a critical value of the circulation, the vortex ring would no longer accept any more vorticity and would instead "pinch-off" from the shear layer that was feeding it—wherein the shear layer would create subsequent secondary vortices. Gharib *et al.* (1998) expressed the amount of fluid ejected as a volume of a cylinder with diameter D_0 and length L equal to the distance the piston traveled. This can be expressed in a nondimensional form as L/D_0 and is called the formation time, $\hat{t}_{GRS}$. Gharib *et al.* (1998) found that the critical value of the formation time for vortex ring pinch-off, known as the formation number, F, is approximately equal to 4. Formation times less than the formation number yield solitary rings whereas formation times greater than the formation number yield a primary ring with a trailing jet behind.

1.3 Vortex Rings as Propulsion

Analytical work considering the influence of vortices on animal locomotion was conducted by Siekmann (1962) who considered 2D vortex dipoles and later by Weihs (1977) who considered axisymmetric vortex rings. Weihs found an analytical expression predicting the thrust of a pulsed jet compared to an equal mass flux rate continuous jet. This expression, which depends on the spacing between subsequent vortex rings, predicts a thrust increase of 25%–60% for pulsed jets that use a formation time of 4 and a thrust increase of over 100% for small ring spacing. This analytical work appears to have been largely ignored until relatively recently, with a plethora of experimental and numerical work exploring the concept of using vortex rings for propulsion in just the last decade.

Krueger (2001) used a piston-cylinder arrangement mounted to a force balance to explore the vortex ring formation process. He found an increase in thrust production ranging

from 20% to 90%, with the maximal thrust enhancement for very short stroke ratios and relatively low pulsing frequencies. Krueger (2001) also developed a model to explain the mechanism behind the increase in thrust. The model showed that an increase in pressure at the nozzle exit for a pulsed jet, which does not exist for a steady jet, was responsible for the improvement in thrust. This "nozzle exit over-pressure," as it was called, accelerated two classes of fluid: the ambient fluid that is entrained in the vortex ring and the ambient fluid surrounding the vortex ring, expressed as the added mass of the vortex bubble. The ambient fluid entrainment and added mass of the vortex bubble are not present in continuous jets and represent fundamental mechanisms through which vortex rings enhance propulsion.

Choutapalli (2007) studied a free continuous jet, a free pulsed jet, and a pulsed jet in a thrust augmenting ejector using air as the working fluid. With the ejector, he found that thrust could be increased up to 130%. Choutapalli's experiments used a "flow chopper"—a rotating plate with six holes in it that are of equal diameter to the exit nozzle. As this plate was driven by a motor, it would rotate and with each rotation of the plate six pulses of air would be ejected. However, the pulses generated were not like that of Krueger (2001), as the setup created a base mean flow with significant perturbations overlaid (i.e., it was not a fully pulsed jet where the jet velocity is zero between pulses).

Concomitant with the aforementioned studies is a body of work exploring synthetic jets. These jets are zero-mass flux in a time-averaged sense as they are driven by reciprocating diaphragms, generally by piezoelectric actuators on the microscale and magnetic actuators (e.g., an acoustic loudspeaker) for larger scales. Synthetic jets have been studied for some time and have been well reviewed by Glezer & Amitay (2002). They originally were studied for use in flow control applications; but Muggeridge & Hinchey (1992) suggested the use of a synthetic jet for propulsion. Later, Müller *et al.* (2000b) published data on thrust

production characteristics of synthetic jets (Müller *et al.* 2001, 2000a). Müller *et al.* (2000b) was followed by a series of studies using larger scale synthetic jets for propelling small underwater vehicles (Polsenberg Thomas *et al.* 2005*a*, *b*). However, all of the work studying synthetic jets in regards to propulsion has only considered the use of synthetic jets for very low speed propulsion. For example, Polsenberg Thomas *et al.* (2005*a*) describes a design for a hypothetical vehicle that would travel on the order of 5 cm s^{-1} (approximately 0.2 body lengths per second). Mohseni et al. has built on this foundation and explored the use of synthetic jets quite extensively for propulsion (Finley & Mohseni 2004; Krieg *et al.* 2005; Krieg & Mohseni 2008, 2010; Krishnan & Mohseni 2009*a*, *b*; Mohseni 2004, 2006). The studies by Mohseni et al., however, have only focused on using synthetic jets for maneuvering purposes and have not used them as the primary means of propulsion on a given vehicle.

Several studies have been done using a squid-based biomimetic platform called "robosquid" (Krueger *et al.* 2008; Moslemi 2010; Moslemi & Krueger 2009, 2010, 2011; Nichols 2011; Nichols, Moslemi & Krueger 2008). The benefit of this platform, compared to the synthetic jet work, is that this was a completely self-propelled vehicle which used vortex rings as its sole source of propulsion. The "robosquid" was propelled using vortex rings from a piston-cylinder arrangement where the piston was driven by a stepper motor. Check valves in the piston and in the vehicle body allowed for the piston to return to its starting position before initiating the next pulse while minimizing the amount of fluid ingested through the nozzle exit. The advantage of this type of an experiment is that a transition from merely measuring the thrust produced to measuring the hydrodynamic efficiency of the vehicle can be made. Another benefit of this system is the opportunity to independently control the frequency of pulsation, jet speed, and stroke length of the pulses. In general, the results from "robosquid" showed an increase of up to 20% in the hydrodynamic efficiency of the

vehicle using vortex rings over a theoretical vehicle using a continuous jet; the efficiency of the vehicle was defined as

$$\eta_P \approx \frac{\overline{F}_T \overline{U}_\infty}{\overline{F}_T \overline{U}_\infty + \overline{\dot{E}}_{ex}}, \tag{1.3}$$

where $\overline{F}_T$ is the time-averaged jet thrust and $\overline{\dot{E}}_{ex}$ is the rate at which excess kinetic energy is shed into the system. They conducted DPIV measurements of the vehicle wake and used the vorticity field to calculate $\overline{F}_T$ and the kinetic energy in the wake after jet termination provided the value for $\overline{\dot{E}}_{ex}$. To calculate an efficiency relative to a steady jet, the equivalent steady-state jet velocity, U_j, was calculated from the average thrust of the vehicle and the steady jet efficiency was calculated using the Froude efficiency, defined as

$$\eta \equiv \frac{2}{1 + \frac{U_j}{U_\infty}}, \tag{1.4}$$

where U_j is the average jet velocity and U_∞ is the speed of the vehicle (Prandtl 1952, pgs. 221–228). Thus the Froude efficiency for the "robosquid" vehicle is an equivalent steady jet efficiency, as the system is incapable of operating with a steady jet. The measured increases in efficiency were maximized for smaller stroke ratio pulses and higher frequencies (nondimensionalized by the pulse duration) for the "robosquid" vehicle.

Ruiz (2010) also studied a vortex-enhanced, self-propelled vehicle (also Ruiz *et al.* 2011). Ruiz's vehicle also used vortex rings as a fundamental element in its propulsion, however the vortex rings were created using a much different mechanism. Ruiz's vehicle was based around a submarine with an internal propeller. This is similar to a pump jet with inlets spaced azimuthally around the body of the submarine. In order to generate the pulsed flow to create vortex rings, Ruiz (2010) incorporated a rotating shell at the inlet section which was driven by the propeller shaft. By adjusting the shape of the rotating shell, Ruiz (2010)

was able to modulate the inlet area and subsequently affect the resulting flow through the nozzle. This created a steady jet with large perturbations and the formation of vortex rings in the wake of the vehicle.

While Ruiz's vehicle did not have as many parameters to control as "robosquid," as the shell rotation (and thus pulsation frequency) was directly tied to the propeller speed (and thus jet velocity), the design of vehicle allowed for a direct comparison of steady versus unsteady propulsion, as the rotating shell could be removed to provide a canonical steady jet. The results of the Froude efficiency measurements showed that Ruiz's vehicle obtained up to a 50% increase in efficiency using the unsteady jet with vortex rings over the steady jet case. Ruiz (2010) also investigated the overall vehicle efficiency as measured by the power coefficient,

$$C_p = \frac{IV}{\frac{1}{2}\rho A_{out} U_\infty^3}, \tag{1.5}$$

where I is the motor current, V is the motor voltage, ρ is the density of the test fluid (water), and A_{out} is the area of the jet nozzle exit. The value of C_p is a nondimensional expression of the electrical power input into the system, which quantifies the electrical power required to maintain the kinetic energy of the system. When the C_p of the unsteady case was compared to the steady case without the rotating shell, Ruiz's vehicle showed the potential to reduce the energy input into the system by over 30% while maintaining the same vehicle speed. This was the first and so far the only experiment to show that the benefits of vortex ring propulsion extend beyond thrust or hydrodynamic efficiency improvements but also into a full systematic definition of efficiency, akin to a "well-to-wheels" analysis. One of the downsides of the work of Ruiz (2010) is that the vehicle only occupied a narrow range of formation time, and the potential to explore a broader range of formation times would also

be beneficial.

Another approach to using vortex rings for propulsion can be found by adopting a biomimicry approach, where researchers directly mimic the body forms and mechanisms from nature. Under this approach there have been numerous efforts at creating pulsed jet vehicles, such as those mimicking jellyfish (Nawroth *et al.* 2012; Tadesse *et al.* 2010, 2012; Villanueva, Smith & Priya 2011; Yeom & Oh 2009), octopus (Serchi *et al.* 2013), and cuttlefish (Wang, Wang & Li 2011) in addition to the "robosquid" platform previously discussed (Nichols *et al.* 2008). If one extends the notion of a vortex-ring enhanced vehicle to include propulsion via the control of vortex structures and not just rings, this list becomes considerably larger with attempts at mimicking penguins (Man *et al.* 2012), tuna (Anderson & Chhabra 2002), carp (Ichiklzaki & Yamamoto 2007), knifefish (Low 2006), generic fish (Hu 2006), lamprey (Ayers *et al.* 2000), bees (Finio & Wood 2012; Wood 2008), and stingrays (Valdivia y Alvarado *et al.* 2010).

1.4 Pulsed Jet Generation Mechanisms

Two primary mechanisms have been used for generating pulsed jets: piston actuation and flow chopping. The former mechanism was used for the "robosquid" vehicle (Nichols *et al.* 2008) (and to a degree, synthetic jets can be considered a variant of this) while the latter for the work of Choutapalli (2007) and Ruiz (2010). There are trade-offs to each. The benefit of the piston mechanism is that there is control over the pulse length (both in time and space, and hence control over jet velocity) and velocity program (e.g., a square-wave or a sinusoid; cf. Krueger (2001)). However, it is difficult to make a proper comparison between a steady jet and a pulsed jet from a piston-actuated vehicle as the vehicle is intrinsically incapable of generating a steady jet. Modeling can help account for this deficiency (Nichols

et al. 2008), however for experiments it is convenient to have an alternative experiment as the control case, rather than theoretical models.

The flow chopping mechanism was used successfully in the stationary experiments by Choutapalli (2007) and the self-propelled vehicle of Ruiz (2010). The shortcomings of this particular mechanism is that the two examples mentioned yielded a jet with significant perturbations rather than a fully pulsed jet, as that obtained by the piston actuation mechanism. The benefit from this type of mechanism is through careful design one can control the pulse length and velocity program. A particular benefit of this design for comparing against a steady jet is that it is straightforward to make the comparison. Either one locks the flow chopper such that the nozzle experiences nonperturbed flow or one replaces the flow chopping element with a nearly open design so as to not perturb the flow. These designs were both used successfully in Choutapalli (2007) and Ruiz (2010) to yield an experimental control case for comparison with the pulsed data sets.

One of the other shortcomings of the flow chopping mechanism is its energy use, this was addressed by Ruiz (2010). Since Ruiz was investigating the energy use of the entire vehicle, it was important to consider the energy consumed in generating the pulsed flow, that is, the energy used in rotating the flow chopping element. It was found that the energy required to rotate the flow chopper was substantial and that the energetic cost of running the flow chopper could outweigh the benefit gained from the vortex rings produced. Because of the energetic expense of existing mechanisms, the current work has the aim of creating greater improvements in efficiency through a new mechanism. In particular, a passive mechanism for generating the flow pulsatility was desired as it was believed that this would help reduce the energetic losses from generating the pulsatility.

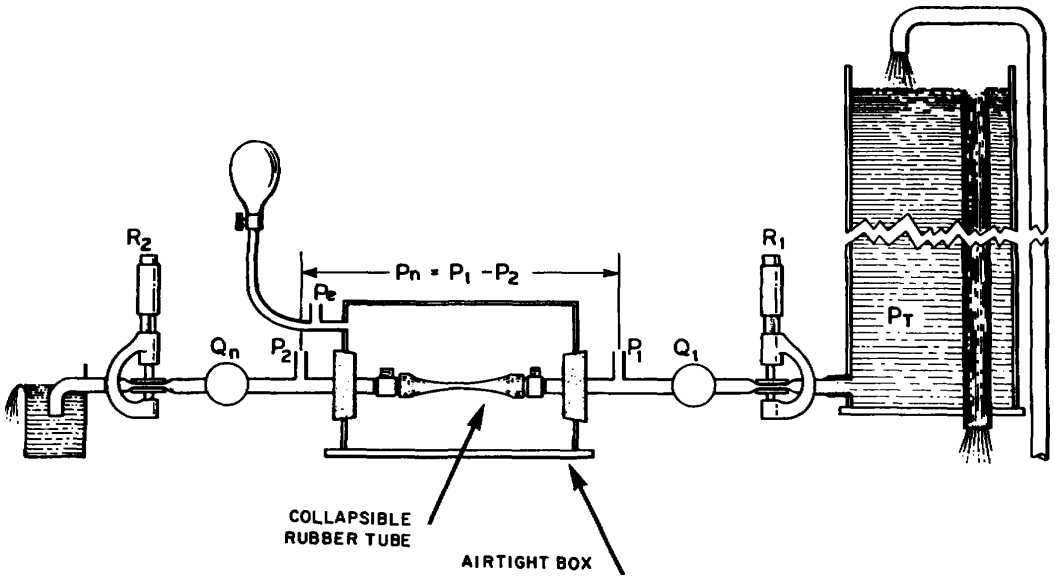

Figure 1.1: Schematic of experimental setup from Conrad (1969) ©1969 IEEE. In the center is the Starling resistor with the collapsible tube encased in an airtight box. Present in this image are micrometers used to control upstream and downstream resistance, indicated by R_1 and R_2, respectively. Two flowmeters measure the upstream and downstream flow velocity, indicated by Q_1 and Q_n, respectively. Finally, the pressures of interest are marked as the upstream pressure, P_1, the downstream pressure P_2, and the pressure external to the tube, P_e.

1.5 Starling Resistor

As a means of generating flow pulsatility, the current work has developed a device based on the Starling resistor. The Starling resistor was first described in a paper by Knowlton & Starling (1912) and was intended to be provide resistance to an isolated dog's heart in the same manner as the peripheral load would normally provide *in vivo*. In essence it is a collapsible tube under external pressure, as seen in figure 1.1. The schematic of Conrad (1969), shown in figure 1.1, shows a very common bench-top setup for studying a Starling resistor, visible in the center of the figure. The device is driven by a constant-pressure-head tank with the flow modulated by the upstream and downstream resistances as well as the pressure external to the tube, P_e. The tube can be made of any elastic material such as latex or silicone.

For most flow and external pressure conditions, the Starling resistor provides variable resistance through modulating the cross-sectional area of the tube. One of the first to explore and report an additional phenomenon in the Starling resistor was Holt (1941). Holt reported that the device produced self-excited oscillations at certain values of the flow rate and external pressure. Although the self-excited oscillations were first described in the jugular vein of a horse in 1824 by Barry (cf. Brecher 1956, pgs. 8 and 66), this was their first description from a lab experiment. This work was followed up by Conrad (1969) who conducted a systematic investigation of the oscillation criteria and also modeled the oscillations as a Van der Pol's oscillator. The self-excited oscillations makes the Starling resistor of particular interest as a means of generating vortex rings for propulsion. Because of the focus on the formation time in regards to vortex ring development, the current work has had a focus on the frequency of oscillation, as the pulse length is a key attribute for calculating the vortex ring formation time. Furthermore, the current work will aim to create large amplitude self-excited oscillations as these will create more defined vortex rings.

In the past several decades, there have been many experimental (Bertram 2003 and references therein, Bertram & Tscherry 2006, and Bertram *et al.* 2008) and numerical (Heil & Jensen 2003 and references therein, Heil & Boyle 2010, Heil & Hazel 2011, Heil & Waters 2006, 2008, Liu *et al.* 2011, 2009, Stewart *et al.* 2010, 2009, and Whittaker *et al.* 2010*a*, *b*) studies to better understand the self-excited oscillations of the Starling resistor. Despite the plethora of studies, there has been little conclusion as to the mechanism of the self-excited oscillations. Experiments have considerable difficulty elucidating the internal flow field as traditional dye visualization or PIV methods have challenges due to poor optical access to the inside of the rapidly deforming collapsible tube. Numerics, on the other hand, also have challenges as the complexity of time-dependent, 3D, moderate Reynolds number

($\mathcal{O}(10^2$–$10^4)$) fluid flow is already an on-going research problem, even without the need to also model a rapidly deforming, hyperelastic collapsible tube.

Because of these restrictions, many experiments have been restricted to evaluating the bulk properties of the flow and tube geometry rather than the detailed flow field (Bertram 1986; Bertram & Castles 1999; Bertram & Godbole 1995; Bertram *et al.* 1990, 1991, 1994; Bertram & Tscherry 2006). More recent studies at experimentally measuring the flow field have been conducted, but due to limited optical access, the results are limited to the region just downstream of the collapsible tube exit (Bertram *et al.* 2001; Bertram & Nugent 2005; Bertram *et al.* 2008). There have been some studies that have measured the flow field within the tube by clever techniques using laser doppler velocimetry (LDV) (Ohba *et al.* 1989; Ohba, Sakurai & Oka 1997), however they were limited in their spatial resolution as LDV is only a point-wise measurement and thus they only obtained a small number of points along the tube axis.

The earliest work in modeling was using lumped-parameter models (Bertram & Pedley 1982; Conrad 1969), which then led to 1D (Cancelli & Pedley 1985; Hayashi *et al.* 1998), 2D (Jensen & Heil 2003; Liu *et al.* 2011, 2009; Luo *et al.* 2008; Luo & Pedley 1995, 1998, 2000; Stewart *et al.* 2010), and most recently 3D modeling efforts (Heil & Boyle 2010; Heil & Waters 2008; Marzo *et al.* 2005; Whittaker *et al.* 2010*a*, *b*). However, existing numerical studies have been limited in scope due to the computational complexity of solving the fluid-structure interaction problem at sufficiently high Reynolds number and in three dimensions.

It is still generally believed that the mechanism of operation has not been adequately described. At first, one might suspect that traveling waves along the tubes dictate the frequency of oscillation. This would yield a mechanism that is similar to the resonance wave phenomenon of the impedance pump (Avrahami & Gharib 2008; Hickerson, Rinderknecht

& Gharib 2005). However, tests examining the effect of tube length found little significant change in the oscillation frequency due to changing the tube length (Bertram *et al.* 1990). Thus end-to-end wave propagation in the tube is not the primary driver of the self-excited oscillations.

One mechanism that has been identified in the numerical literature creates oscillations known as the "sloshing" mode (Jensen & Heil 2003). This mode was first identified for a 2-D collapsible channel (Jensen & Heil 2003) and later shown to exist also for 3-D collapsible tubes (Heil & Waters 2006, 2008). This mode operates when the tube is in high tension, the Reynolds number is $\mathcal{O}(10^2)$, and the axial length of the tube is significantly larger than the tube length. The mechanism for this flow oscillation is described as the fluid within the tube consisting of an unsteady inviscid core in which the traversely oscillating collapsible wall generates axial "sloshing" motions (oscillations). A necessary condition of this mechanism, however, is that the axial sloshing amplitude must be greater at the influx to the tube than at the efflux in order for there to be a net kinetic energy input into the system to keep the system running. Furthermore, it is necessary that the tube oscillate in a "mode 1" shape—which yields a single maxima or minima in tube displacement near the midline of the tube's axial direction. This mode has been studied extensively numerically (Heil & Boyle 2010; Heil & Waters 2006, 2008; Jensen & Heil 2003; Liu *et al.* 2011; Luo *et al.* 2008; Stewart *et al.* 2010; Whittaker *et al.* 2010*a*, *b*) however has never been recreated in an experiment. Furthermore, the amplitude of the oscillations generated tend to be quite small.

For larger amplitude oscillations, many of the mechanisms suggested in the literature point (Cancelli & Pedley 1985; Luo *et al.* 2008; Luo & Pedley 1995; Stewart *et al.* 2010) to Bernoulli's effect acting on the tube during the collapse phase of the oscillation cycle as follows: the tube is narrowed due to the external pressure, and the axial pressure gradient

along the tube accentuates this narrowing or collapse at the downstream end of the tube; through mass conservation, the decreasing cross-sectional area increases the fluid velocity, lowering the local fluid static pressure; this in turn starts a closed-feedback loop that rapidly accelerates reduction of both the tube internal cross-sectional area and the local static pressure. This completes the collapse phase of the oscillation cycle. However, the mechanism of the tube's recovery or relaxation, allowing for another oscillation cycle, is still elusive. There have been theories and suggestions as to the mechanism behind the relaxation phase, but none have been properly validated. These relaxation mechanisms will be described in the following paragraphs.

A mode of oscillation that has been explored numerically was first described by Luo & Pedley (1995) although it will be referred to as "slamming" per Stewart *et al.* (2010). In this oscillation mode, the tube tension is low and the oscillation magnitude becomes so large as to break down the earlier numerical scheme of Luo & Pedley (1995) but is sustained in the later work of Stewart *et al.* (2010). Additionally, it should be noted that in Luo & Pedley (1995), the upstream condition had an imposed steady Poiseuille flow with a fixed downstream pressure, thus allowing for velocity oscillations to occur in the downstream segment. Stewart *et al.* (2010) followed up on this work recreating the large-amplitude "slamming" oscillations using only proscribed pressure boundary conditions. Stewart *et al.* (2010) also suggests a mechanism for these large amplitude oscillations, where one sees significant deformation of the tube or membrane surface. The proposed mechanism of Stewart *et al.* is that the deformation of the collapsible segment (particularly in the downstream-most end of it) causes a significant increase in the curvature of the surface and is accompanied by a drop in the pressure locally. This generates an adverse pressure gradient in the rigid tubing downstream of the collapsible section. The adverse pressure gradient then drives

fluid back into the collapsed section, which pushes the constriction upstream, reducing the wall curvature and the magnitude of the adverse pressure gradient with it. The cycle then repeats the pressure feedback loop to sustain the oscillation.

Yet another proposed mechanism for the oscillations can be found in the work of Cancelli & Pedley (1985). In this 1-D modeling work, they model the self-excited oscillations via the consideration of separation downstream of the tube constriction. In particular, they found that the key mechanism of the oscillations was dependent on the location of separation. This recovery mechanism relies on the presence of a separation bubble downstream of the throat increasing the local pressure and thus allowing for the collapsible tube to expand during the recovery portion of the cycle. Once the tube has expanded enough that the separation bubble is eliminated (or significantly reduced), ostensibly due to the reduced curvature of the tube allowing the flow to remain attached along more of the tube, the cycle can repeat itself by entering into the collapse phase (driven by Bernoulli's effect), creating self-excited oscillations. Thus Cancelli & Pedley (1985) put forth that separation is essential for self-excited oscillations. However later work by Hayashi *et al.* (1998) were able to obtain oscillations in a similar model by modeling the viscous friction rather than the separation. Thus while separation may be evident in collapsible-tubes during self-excited oscillations (Kounanis & Mathioulakis 1999), it is not guaranteed to be a sufficient or necessary condition for self-excited oscillations to occur.

Another mechanism for the self-excited oscillations is suggested by Luo *et al.* (2008) and is similar to the mechanism of Stewart *et al.* (2010) but in reverse. In essence: a positive feedback loop between the velocity, pressure, and tube area works to collapse the tube, then due to the significant viscous resistance at the tube throat (a region of very high velocity with a very small cross-sectional area) the pressure drop axially along the tube

increases and causes the pressure upstream of the constriction to rise, this rising pressure makes the upstream section bulge out and ultimately forces open the constriction. Once the constriction has been opened, the cycle then repeats to sustain the oscillations.

Experimentally determining the primary mechanism is challenging as one can envision a scenario where at the end of the collapse phase the pressure drop along the tube increases (per Luo *et al.* (2008)) simultaneously with the flow separating in the downstream end of the tube (per Cancelli & Pedley (1985)) and flow reversal (per Stewart *et al.* (2010)). Thus elements of all three mechanisms may be seen experimentally. The determination of which factor is the main cause can be difficult.

As a means to help elucidate the mechanism at work, experimental parameters studies have been done, although they are few. As mentioned previously, Bertram *et al.* (1990) examined the effect of changing the tube length, L_0. They found that as the tube lengths were changed within the range of L_0/D_0 = 4 to 34, that there was little change in the oscillation frequency, which ranged from 2.0 to 4.3 Hz for the minimum low frequencies of each tube, respectively. Bertram *et al.* (1990) did suggest that the tube length appears to play a role of which oscillation modes were excited, with the longest tube displaying the largest number of unique modes, however the actual frequency value was unchanged between tubes oscillating using the same mode. Additionally from this study, the many oscillation modes that were reported leads to the suggestion that different physical mechanisms could dominate in some modes and not others. Thus a search for *the* mechanism of oscillation should instead be considered as a search for proof of *a* mechanism. Another experimental parameter study conducted was by Sakurai *et al.* (1996), who considered the effect of longitudinal tension on the self-excited oscillations. For a range of tube strains, which ranged from 0 to 1, Sakurai *et al.* (1996) found a decrease in oscillation frequency with increasing tension (strain) for

the same flow rate through the tubes. This was explained due to the larger tension causing the tube deformation to extend along more of the tube axially, whereas in the zero-tension case the tube deformation is localized to the downstream-most end of the collapsible tube. Because the deformation is more spread out for the higher tension tubes, a larger mass of fluid is involved in the oscillation providing a larger resistance to oscillation and ultimately a lower oscillation frequency.

The existing literature provides no design rules by which to predict the oscillation frequency of a collapsible-tube based device. Even if we consider the possibility of using scaling laws for identifying which parameters affect the oscillation frequency, it would be challenging to identify which scaling is correct. A scaling for the frequency of oscillation from Jensen & Heil (2003) suggests that the frequency goes as $f \sim \sqrt{T' D_0/\rho L_0^4}$ where T' is the tension, D_0 is the tube diameter, ρ is the fluid density, and L_0 is the length of the tube. Heil & Waters (2008) find that $f \sim \rho U_j^2$. Additionally, a simple balance of fluid inertia against the wall stiffness, mentioned in Heil & Waters (2008), provides that $f \sim \sqrt{Eh^3/\rho D_0^5}$, where E is the Young's modulus, and h the tube-wall thickness. The model of Cancelli & Pedley (1985) shows that $f \sim \sqrt{Eh^3/\rho D_0^5}$, in agreement with the balance shown in Heil & Waters (2008).

The effect the diameter of the tube has on the frequency is uncertain as the scaling law from Jensen & Heil (2003) suggest that the frequency and diameter are positively related whereas Heil & Boyle (2010), Heil & Waters (2008), and Cancelli & Pedley (1985) suggest that they are negatively related. Similarly, the effect of changing the flow rate, U_j, appears to be in conflict as Heil & Waters (2008) suggest $f \sim U_j^2$ whereas Heil & Boyle (2010) state $f \sim U_j^{-1}$.

1.6 Objective

The goal of this research is to develop a means for generating pulsed flow passively with the aim of creating a vortex-ring-enhanced wake. With this goal in mind, we are primarily concerned with designing a collapsible-tube-based device that generates large-amplitude oscillations with minimal flow losses.

The current work will build off these two fundamental areas of study: vortex rings for propulsion and self-excited oscillations in collapsible tubes. Due to the potential for reducing the energetic cost of producing pulsed jets, the current work embarks on the use of a collapsible-tube based device for generating vortex rings passively. Furthermore, the potential to explore the formation time space in regards to vehicle efficiency is desired as Ruiz *et al.* (2011) considered only a narrow range of formation time for their vehicle.

Additionally, this research has also extended the basic knowledge of self-excited oscillations in collapsible tubes. In particular, if one was to attempt to design a collapsible tube device and wanted it to oscillate at a given frequency, there are no means of accomplishing that except through iterative design. Since the frequency of oscillation is an important parameter in regards to the vortex ring formation, it is a parameter that we have focused on as part of this work. The goal is to develop a passive device suitable for propelling vehicles on the order of $\mathcal{O}(10^0$–$10^3)$ m in size, whereas existing literature on collapsible tubes only has studied tubes on the order of $\mathcal{O}(10^{-3}$–$10^{-2})$ m in diameter. Thus if one is to scale up a passive device to propel much larger vehicles, it is essential to know how this will affect the oscillation frequency and subsequently the vortex ring formation. Another goal of this work is to explore the effect that tube dimensions have on the frequency of self-excited oscillations. As mentioned previously, the current literature provides conflicting results. In

an attempt to help resolve some of these conflicts, an experimental parameter study of a collapsible tube nozzle was undertaken as part of the current work.

The rest of this thesis is laid out into two general parts. The development of a passive vortex generator (PVG) for integration into an existing autonomous underwater vehicle (AUV) is discussed in chapter 2. The PVG-integrated AUV was used for testing and optimizing the vehicle efficiency. Chapter 3 aims to extend the existing experimental results for collapsible tubes by conducting a parameter study of a collapsible-tube-based propulsion nozzle. In particular, the effect of changing tube diameter and length were studied. Lastly, a summary and discussion of the impact of these findings along with suggestions for future work are included in chapter 4.

Chapter 2

Integrated Passive Vortex Generator Tests

2.1 Introduction

On the basis of the parameter study results, discussed in chapter 3, it was found that the frequency of self-excited oscillations from collapsible-tubes under external pressure was only weakly affected by changing physical dimensions. This knowledge opened up the ability to design a passive vortex generator (PVG) to integrate into a full-scale autonomous underwater vehicle (AUV). The work integrating the PVG into the AUV and the impact the PVG had on the vehicle propulsion will be discussed in this chapter. The chapter will begin by an overview of the experimental setup, followed by the methods by which the experiments were conducted, and finally the results will be presented with a discussion.

2.2 Experimental Setup

2.2.1 PVG Design and AUV integration

The complete vehicle can be divided into two parts: the main vehicle and the add-on PVG. As such, the sections covering the vehicle will use this same division to discuss aspects of

the PVG-integrated AUV.

2.2.1.1 Main Vehicle

For conducting the tests of integrating a PVG to a self-propelled vehicle, a small autonomous underwater vehicle (AUV) was acquired from Professor Stilwell at Virginia Tech and shown in figure 2.1. The vehicle, known as the Virginia Tech 475 AUV, has a hull diameter of 12.06 cm, a length of 1 m, and is capable of traveling at a nominal speed of 1.5 m s^{-1} (Gadre *et al.* 2008; Petrich 2009; Petrich, Neu & Stilwell 2007; Petrich & Stilwell 2010). The aim of the integration was to retrofit an existing AUV with a PVG. As such, limited modification to the main vehicle was desired. In order to attach the PVG, the control surfaces and strakes from the aft end of the vehicle were removed and the propeller shaft was extended. The AUV was installed upside down, with its sail pointed toward the ground, in order to easily mount the vehicle to a sting using tapped holes that were on the (previously) ventral side of the AUV. A 10-wire umbilical cable was used to supply the AUV with power and control commands to the motor. Four of these wires were used for the USB connection to the servo controller, four other wires were used for delivering power to the motor controller (positive and negative line each used two wires), and the remaining two umbilical wires were wired up to another aspect of the AUV that was not used in this application. At the distal end of the umbilical, a USB cable was wired for connecting a computer to the servo controller and two male banana plugs were wired for supplying power to the AUV. The power for the AUV system (and also used for other electrical sensors) was generated by a power supply (Agilent 6674A) that had the capability to output 0–60 V at 0–35 A. This power supply was located to the side of the test tank and the wires for delivering power traveled along a 20 m long energy snake. Because of the long length of the power wires, the

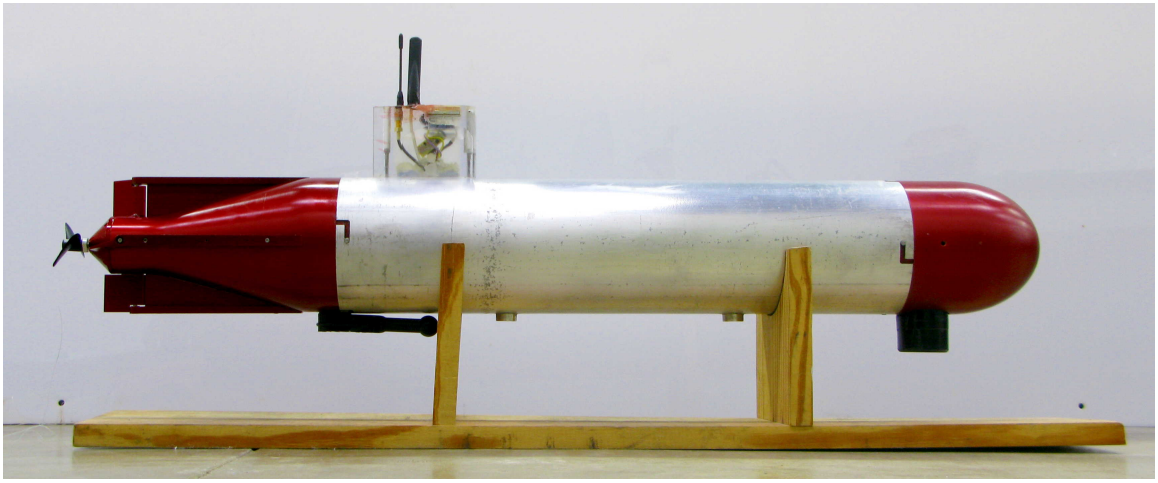

Figure 2.1: Photograph of the VT 475 AUV, the main vehicle used in the PVG-integrated AUV experiments.

power supply used a remote sensing feature to ensure that the voltage delivered to the AUV was the desired value of 13.0 V. This remote sensing feature enabled the power supply to overdrive the voltage at the supply in order to compensate for the significant voltage drop experienced through the long wires.

Inside the AUV, the components used in these experiments were based on standard remote-control hobby parts. A servo controller (Pololu Micro Maestro) was connected via a USB connection to the controlling computer. The servo controller commanded a motor controller (Hyperion Titan 20A Hi-Pro) attached to the AUV propeller motor (Hyperion ZS2209-30). This motor was geared down in a 40:19 ratio to the propeller shaft. Control of the motor was obtained by sending serial commands from a computer to the servo controller. The motor speed could be controlled manually and as part of an automated computer script. The input to the motor, called the "throttle setting" and hereafter denoted T, was related to the pulse width for a servo control (e.g., a servo running a control surface) which is translated by the motor controller into a three-phase, pulse-width-modulated signal for driving the motor. The throttle setting, T, ranged from 1000 (off) to 2000 (full throttle),

with 1100 being the onset of motor rotation. It should be noted that these throttle values have no direct physical significance (e.g., RPM, torque, etc). Due to the concern of over-driving the thin wires in the umbilical, T was never set to its full setting of 2000 and hence the data presented is limited to a lower throttle setting.

The selection and axial location of the propeller was carefully chosen based on the design of the integrated PVG. A variety of propellers were tested with varying pitch, diameter, and blade number. In the end, maximal thrust was produced by a three-bladed, 47 mm diameter propeller with a pitch of 1.4 constructed of fiberglass-reinforced plastic. It was mounted as far aft as possible without striking the sides of the PVG contraction (cf. figure 2.2).

2.2.1.2 Integrated PVG Design

The primary goal of adapting a PVG to an AUV was to enable an AUV to produce the vortex rings necessary for improving propulsion by using the flow generated by the propeller to drive the PVG. A secondary goal was to minimize the amount of losses from the device—both from changes to the overall vehicle drag as well as from resistance to the internal flow. Three designs were tested with different configurations (two with the propeller upstream of the collapsible tube and one downstream). The final design was chosen as it yielded the best propulsion characteristics.

The ratios of the inlet area to nozzle exit area and the contraction ratio and angle were adapted from the submarine developed by Ruiz (2010). Thus it must be noted that the PVG designed and developed for integration to this AUV is in no way an optimal design in terms of reducing the losses to the overall system. This was not pursued as the primary focus of this work was on the PVG and the resulting vortex dynamics. Furthermore the PVG

design was constrained to the AUV provided. It is possible that should one be designing an integrated system from scratch, or modifying a pump-jet system, that one could attain a more optimal arrangement.

The overall design of the PVG-integrated AUV is shown in figure 2.2a with detailed drawings available in appendix A. The integrated PVG has a nozzle and tube diameter of 4 cm and a collapsible tube length of 16 cm, which gives the device an L_0/D_0 value of 4. The tube-wall thickness had a value of $h = 0.5$ mm. The outer diameter of the PVG matches the diameter of the main vehicle to maximize the internal air chamber volume while minimizing form drag. Additionally, the integrated PVG adds approximately 50 cm of length to the vehicle, making the total vehicle length nearly 1.5 m. The final design aimed to minimize the number of seals required to properly seal the air chamber from leaks and thus the PVG is constructed out of only two pieces: an internal frame and a cover. This design yields only two sealing joints while also providing maximal access to the collapsible tube for mounting. Another goal of the design was to maximize the internal chamber volume, and thus the amount of solid material used for construction was minimized. In order to obtain all of these goals, the two-piece integrated PVG was manufactured using a rapid prototyping technique called stereolithography. This method yielded a very smooth surface finish, appropriate for minimizing friction drag.

Prior personal experience with building PVG devices showed that the volume of the PVG air chamber has a significant influence on the kinematics and dynamics of the system. The volume ratio between the air chamber and the collapsible tube of the nozzles is defined as

$$\lambda \equiv \frac{V_c}{V_t}, \tag{2.1}$$

where V_c is the volume of the chamber and V_t is the volume of the distended tube. When calculating V_c, it is necessary to account for the volume of any instrumentation, cabling, hardware; V_c is only the volume of the air within the chamber. The effect λ has on the chamber pressure, P_e, can be represented as

$$\Delta P_e = \frac{\beta}{\lambda}, \tag{2.2}$$

where ΔP_e is the magnitude of the chamber pressure oscillation in one period (in percent) and β is a nondimensional factor relating to the amount of tube collapse during one oscillation period (cf. appendix B for derivation of ΔP_e). This equation shows that for very small λ, that the variation in the chamber pressure can become quite significant over one oscillation period. As such, small λ can affect the tube kinematics. The maximization of the internal chamber volume of the integrated PVG also maximized the volume ratio λ.

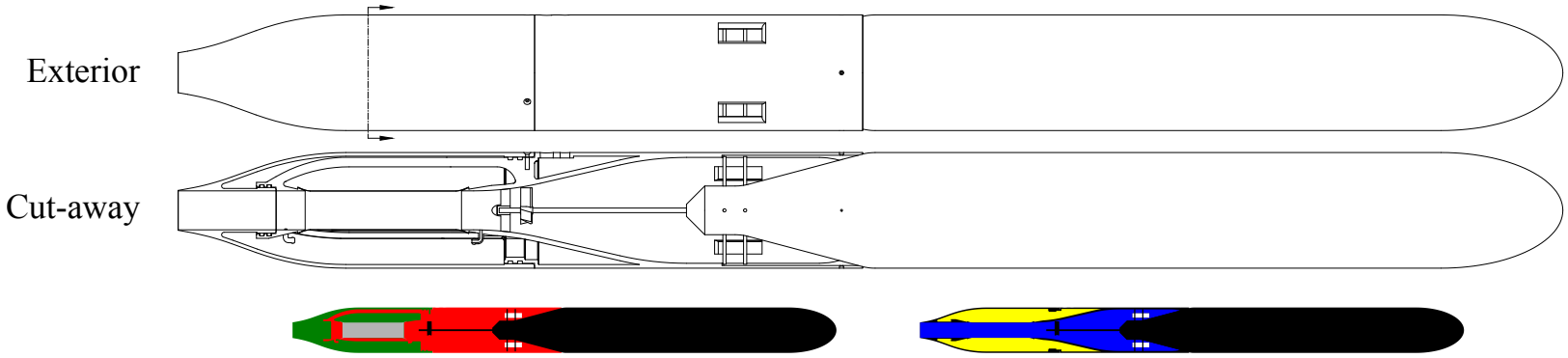

(a) Side view of the PVG-integrated AUV. Top figure shows the complete system exterior with the lower figure showing the system with a cut plane parallel to the page through the middle of the system. The left inset drawing highlights the different components making up the assembly. In black is the AUV, red is the PVG internal frame, green is the PVG cover, and grey denotes the collapsible tube. The right inset shows the different media within the device. In blue is water, yellow is air, and black is solid material. The section line in the top figure corresponds to the section view in figure 2.2b.

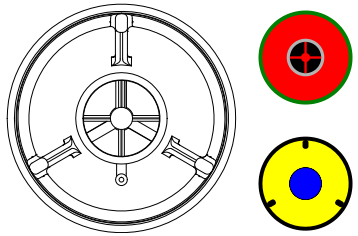

(b) Section view of the integrated PVG system. As in 2.2a, the colors in the inset highlight the different components making up the assembly. For the top inset, black is the AUV, red is the PVG internal frame, green is the PVG cover, and grey denotes the collapsible tube. For the bottom inset, blue is water, yellow is air, and black is solid material.

Figure 2.2: Schematic drawings of PVG-integrated AUV.

The PVG was instrumented with pressure transducers for measuring the chamber, driving, and transmural pressures. Pressure taps were located in the rigid tube 2 cm (one-half of the tube diameter) upstream and downstream of the collapsible tube. These pressure transducers were attached to an instrumentation amplifier circuit and read by a data acquisition system (DAQ, K in figure 2.6). The pressure transducers and amplifier were calibrated using a water manometer. The DAQ system (National Instruments USB-6221) was connected to a computer (hereafter the DAQ computer) that accessed the DAQ system via the MATLAB (Mathworks) software program. The DAQ system was set up to record the pressure transducer signals at 5 kHz for the duration of a self-propelled run. This high sampling rate was sufficiently high to capture all the higher order modes of the signal and ensure that software-based post-filtering would remove the noise within the signal sufficiently. The DAQ system also recorded the voltage and current entering into the AUV vehicle. The current was measured from the voltage drop across a 0.05 Ω shunt resistor that was placed "upstream" of the power supply's remote voltage sensor connection, so as to ensure that the power entering the umbilical of the AUV was at the proper voltage.

Ballast weight was added to the air chamber of the PVG to make the PVG approximately neutrally buoyant. The combination of the ballast weight and the pressure transducers yielded a PVG air chamber volume of 2600 $\pm$ 50 cm^3. This gave the PVG a volume ratio of $\lambda = 13 \pm 0.2$.

For filling and draining the air in the chamber, two solenoid valves were used. One solenoid valve connected the PVG air chamber to a high-pressure line regulated at 75 kPa through a 0.25 mm diameter flow-control orifice. This solenoid was used for filling the chamber. The other solenoid valve exhausted the PVG air chamber to the ambient. Both of these solenoid valves were controlled using a MOSFET-based circuit that drove the high-

current, 13 V solenoid using a low-current, 5 V digital signal from the DAQ board.

As the fill and exhaust solenoids are simply on-off and not proportional, it was unrealistic to try to precisely control the pressure in the chamber either with a controller or manually (the latter was done in the parameter experiments of chapter 3). Thus the amount of time the fill solenoid was open, hereafter referred to as the chamber fill time, τ, was the independent variable used in the tests. One can think of τ as being roughly analogous to controlling the amount of air in the chamber as the pressure upstream of the flow-control orifice was nearly sufficient to choke the flow through the orifice and yielded an approximately constant mass flow rate. This is particularly advantageous for the PVG as collapsible tubes under external pressure are especially compliant once they have azimuthally buckled, as seen in figure 2.3a, and have increased sensitivity to pressure during these partially collapsed phases (Kececioglu, Mcclurken, Kamm & Shapiro 1981). The area fraction, α, plotted in figure 2.3 is defined as

$$\alpha \equiv \frac{A(P_t, \tau)}{A_0}, \tag{2.3}$$

where $A(P_t, \tau)$ is the cross-sectional area of the tube and A_0 is the nominal cross-sectional area of the tube without external forces applied (i.e., $P_t = 0$). We expect that if the tube cross-sectional area is changing significantly while the pressure is relatively constant, then the volume of the chamber must be changing and thus the amount of air within the chamber is changing significantly.

To verify the magnitude of the tube collapse as a function of the chamber fill time, photos looking along the axial direction of the tube were taken with different chamber fill times, τ. A set of photos were taken with the PVG dry and another set with the PVG

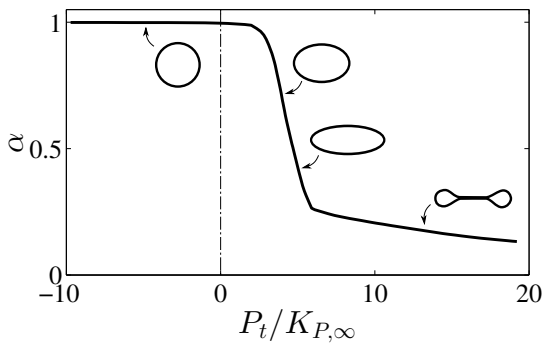

(a) Plot of the cross-sectional area fraction of a collapsible tube versus the transmural pressure, non-dimensionalized by the infinite bending stiffness parameter, $K_{P,\infty}$, modified from Kececioglu *et al.* (1981). Images depict the tube cross-section shape at indicated conditions.

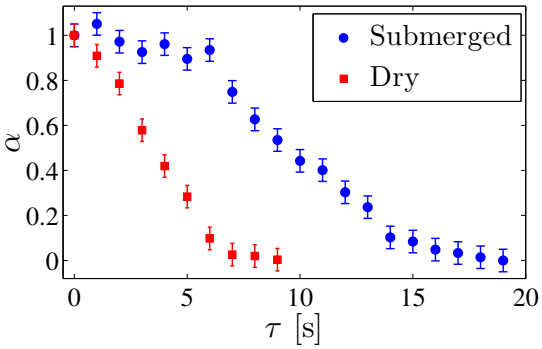

(b) Plot of the cross-sectional area fraction of the collapsible tube from the PVG versus the chamber fill time τ in seconds. Areas calculated from images shown in figures 2.4 and 2.5.

Figure 2.3: Plots of the area fraction of the collapsible tube.

submerged and installed on the AUV as shown in figures 2.4 and 2.5, respectively. Using these photos, the area of the tube cross-sectional area was calculated and then normalized by the area of the tube at $\tau = 0$ seconds. These results are plotted in figure 2.3b for both the dry and submerged PVG.

It is noted that there appears to be a discrepancy between the tube cross-sectional area of the dry conditions and the submerged conditions. For a chamber fill time of $\tau = 0$ s, this means that the chamber pressure is equal to the ambient pressure in the lab. However, the pressure within the collapsible tube differs between the dry and submerged cases. For the dry case, the pressure is identical to the ambient pressure in the lab and thus $\tau = 0$ s for the dry case corresponds to a transmural pressure, P_t, of identically 0. The discrepancy between the dry and submerged cases can likely be resolved if one considers that the submerged tube has a pressure within the tube equal to the hydrostatic pressure from the tank. Thus for $\tau = 0$, $P_t < 0$ for the submerged case. The onset of significant area reduction in the submerged tube (at $\tau \approx 6$ s) is likely the point where $P_t = 0$ for the submerged case.

It is apparent that, as predicted, the chamber fill time reduces the sensitivity of α compared to using the transmural pressure. Because of this decreased sensitivity, the chamber fill time is a better independent variable for ensuring reproducible results.

It should also be noted from figures 2.4 and 2.5 that the tube undergoes buckling and collapse with an mode 3 azimuthal collapse. This is apparent from the tri-lobed shape of the tube's cross-section. This is distinct from many of the earlier works in collapsible tubes, both numeric and experimental that observed in their experiments or constrained their simulations to have a mode 2 azimuthal collapse (Bertram & Nugent 2005; Bertram *et al.* 2008; Bertram & Tscherry 2006; Heil & Boyle 2010; Heil & Waters 2008; **?**). The critical pressure for collapse of a thin cylindrical tube under uniform external pressure loading can be shown to be

$$P_{t,crit} = \frac{4Eh}{D_0}\left\{\frac{4(n^2-1)h^2}{3(1-\sigma^2)D_0^2} + \frac{\pi^4 D_0^4}{16L_0^4 n^4(n^2-1)}\right\} \tag{2.4}$$

using the current nomenclature where $P_{t,crit}$ is the critical transmural pressure for collapse and n is the azimuthal mode of the collapse (Love 1944, Article 341). From this equation, we can see that the critical pressure for a given collapse mode is purely a function of the geometry and material properties of the tube. The assumption of uniform external pressure is not maintained for the PVG experiments, as there is an axial pressure gradient along the inside of the tube due which leads to a spatially-varying transmural pressure, P_t. However, conceptually we can evaluate the criteria under which the tube will collapse with a mode 3 azimuthal mode before a mode 2 azimuthal mode as

$$P_{t,crit,3} < P_{t,crit,2} \tag{2.5}$$

$$\left\{\frac{4(3^2-1)h^2}{3(1-\sigma^2)D_0^2} + \frac{\pi^4 D_0^4}{16L_0^4 3^4(3^2-1)}\right\} < \left\{\frac{4(2^2-1)h^2}{3(1-\sigma^2)D_0^2} + \frac{\pi^4 D_0^4}{16L_0^4 2^4(2^2-1)}\right\} \tag{2.6}$$

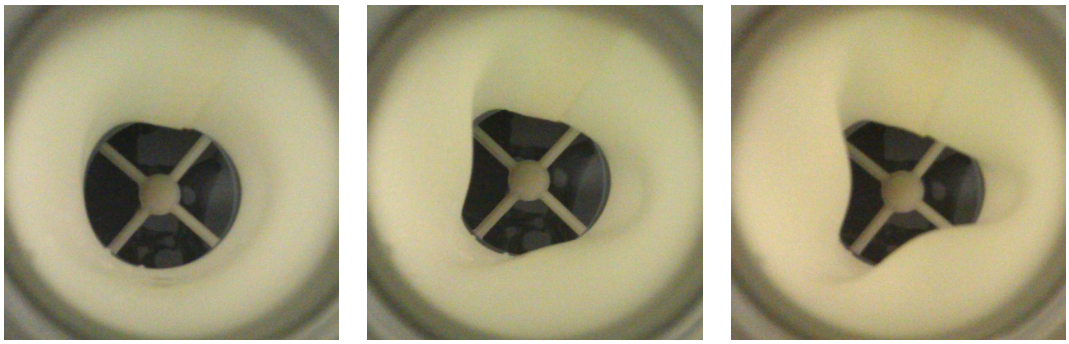

(a) τ = 0 s (b) τ = 1 s (c) τ = 2 s

(d) τ = 3 s (e) τ = 4 s (f) τ = 5 s

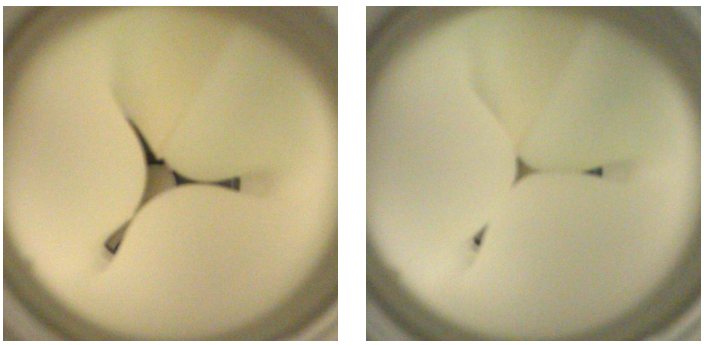

(g) τ = 6 s (h) τ = 7 s

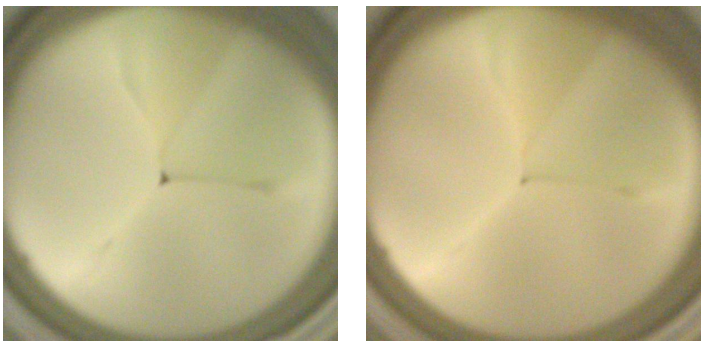

(i) τ = 8 s (j) τ = 9 s

Figure 2.4: Axial view of tube collapse at different chamber fill times, τ, for the PVG exposed to the ambient atmosphere and not submerged underwater.

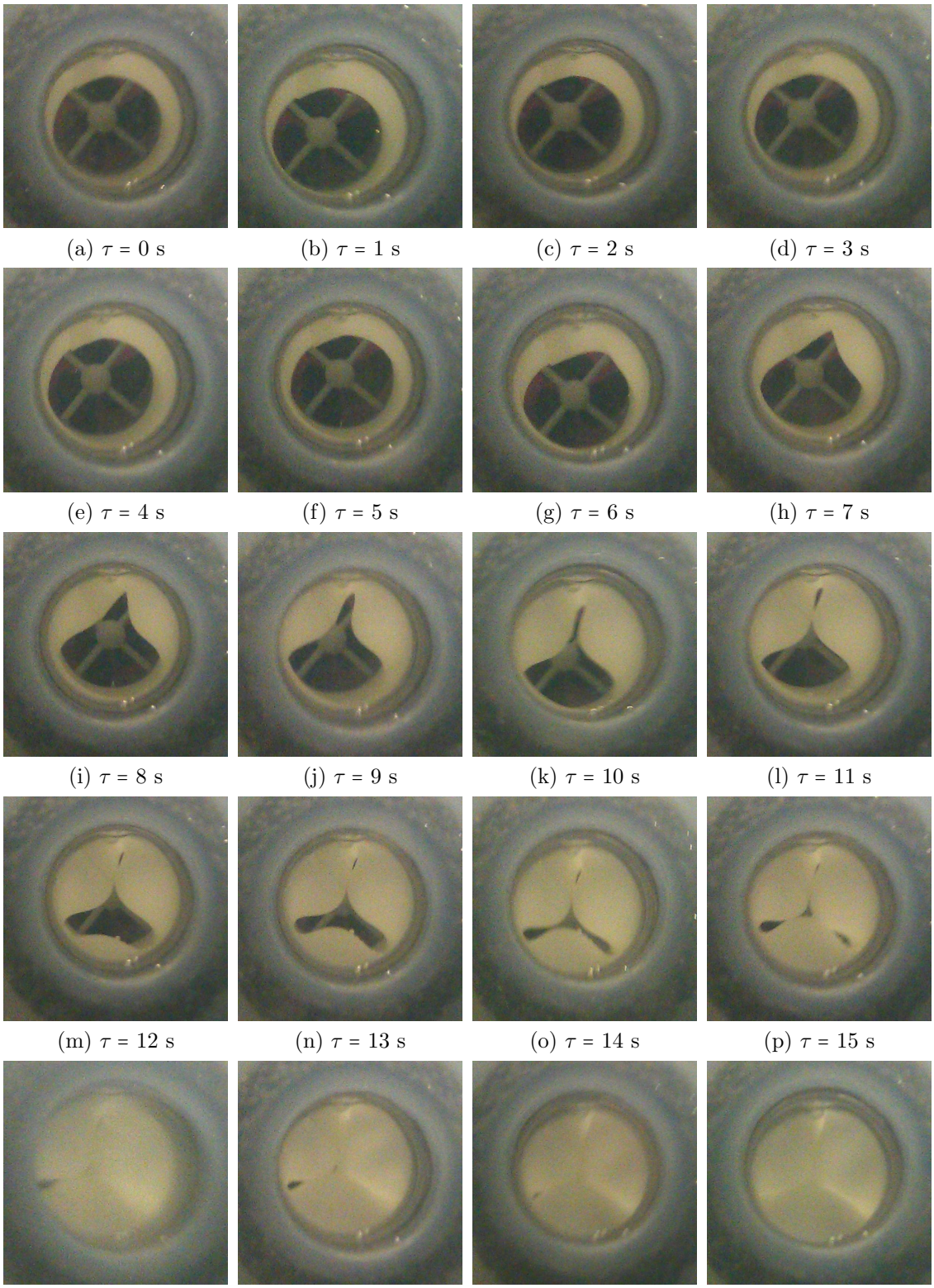

(a) τ = 0 s (b) τ = 1 s (c) τ = 2 s (d) τ = 3 s

(e) τ = 4 s (f) τ = 5 s (g) τ = 6 s (h) τ = 7 s

(i) τ = 8 s (j) τ = 9 s (k) τ = 10 s (l) τ = 11 s

(m) τ = 12 s (n) τ = 13 s (o) τ = 14 s (p) τ = 15 s

(q) τ = 16 s (r) τ = 17 s (s) τ = 18 s (t) τ = 19 s

Figure 2.5: Axial view of tube collapse at different chamber fill times, τ, for the installed and submerged PVG with the propeller stationary. Photos are aligned such that gravity points down.

if we assume that $\sigma = 0.5$ for our rubber material

$$\left(\frac{128h^2}{9D_0^2} + \frac{\pi^4 D_0^4}{10368L_0^4}\right) < \left(\frac{16h^2}{3D_0^2} + \frac{\pi^4 D_0^4}{768L_0^4}\right) \tag{2.7}$$

$$\frac{80}{9}\left(\frac{h}{D_0}\right)^2 < \pi^4\left(\frac{1}{768} - \frac{1}{10368}\right)\left(\frac{D_0}{L_0}\right)^4 \tag{2.8}$$

and say, for the tube we used in the integrated PVG, we have h = 0.5 mm and D_0 = 4 cm. This means we can predict the required tube length, L_0, where we expect to see a mode 3 collapse as $L_0 < 12$ cm. Our actual tube had a length of 16 cm, which does not satisfy the inequality and thus equation (2.6) would predict that our tube should have a mode 2 collapse state. This disagreement, while small, is likely because the tube used in our experiments was not fully axisymmetric as the seam from constructed tube yielded a region of thicker wall stiffness that may have predisposed the tube toward a particular azimuthal buckling mode. Furthermore, the derivation of equation (2.6) involves dropping higher order terms and these may have been necessary to bring the results into quantitative agreement. However, even from this exercise one can see that a mode 3 azimuthal mode is possible for a sufficiently short tube and that appears to be the explanation for our results.

2.2.2 Test Facility and Cart System

All of the experiments using the PVG-integrated AUV were conducted in a 40 m long water tunnel, shown in figures 2.6 and 2.7. For the vast majority of the tests, the tunnel's recirculating pumps were turned off and thus created a tank of quiescent fluid. The AUV was mounted to a motorized cart system that moved on rails extending along the length of the tank test section. The cart's motor (G in figure 2.6) was mounted to the cart and moved the cart through the use of a toothed belt that extended along the length of the flume. The

cart system was retrofitted to incorporate a controller system such that self-propelled tests could be conducted (I in figure 2.6). To allow for completely self-propelled motion, the AUV mounted to the slider of an air bearing (Nelson Air Corp, RAB6) that restricted the AUV's motion along the longitudinal direction of the test section to 10 cm of travel (F in figure 2.6). The carriage of the air bearing was mounted to the cart. Attached to the slider of the air-bearing was an optical target. A short-range laser sensor (optoNCDT 1302, E in figure 2.6), rigidly mounted to the cart, measured the distance to the optical target and thus provided the cart system with the position of the AUV relative to the cart. The cart controller read the current relative position of the AUV and moved the cart such that the relative position of the AUV is kept at a reference value. In this way, the cart system provided the AUV self-propelled motion with minimal interference.

It should be noted that the cart system as a whole has difficulty moving at low speeds (approximately less than 5 cm s^{-1}). This is attributed to both the poor-low-RPM performance of the cart motor and belt stretching by the toothed belt by which the cart motor pulls the cart. Since the toothed belt runs the length of the water tunnel (40 m) there can be significant belt stretch which is more of an issue for lower cart speeds as at higher cart speeds the belt has sufficiently acquired enough tension to have prestretched the belt.

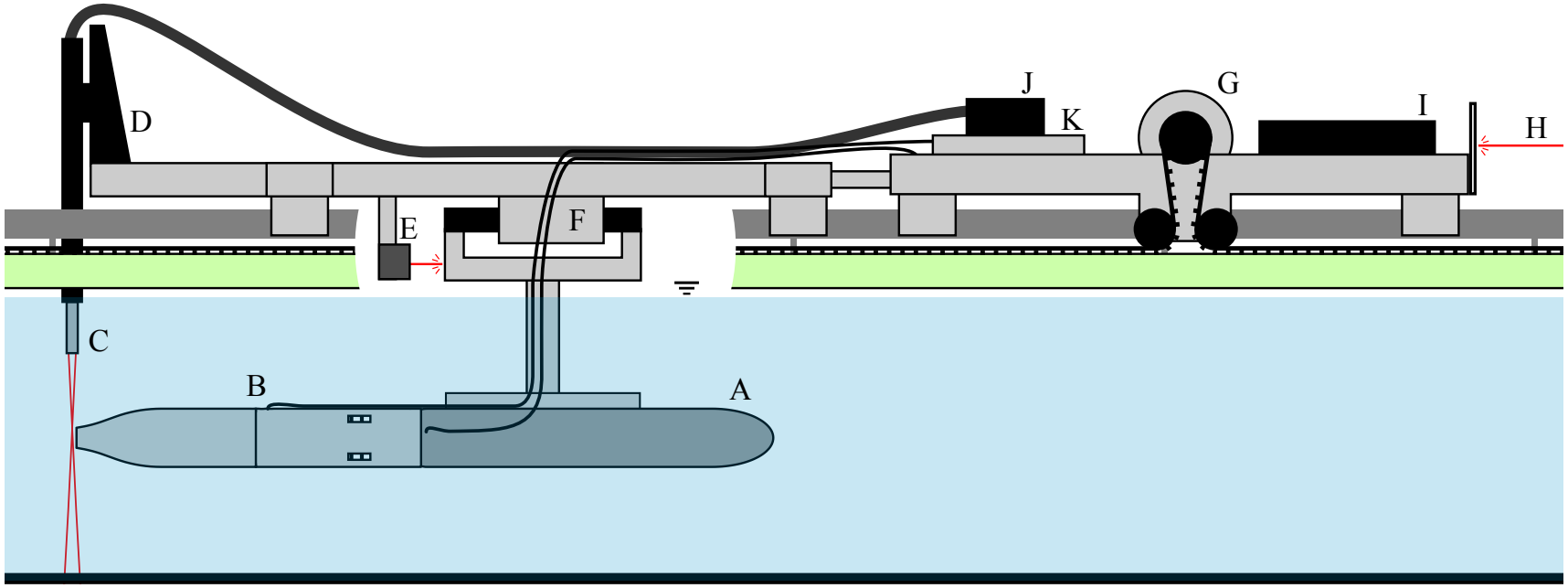

Figure 2.6: Schematic drawings of facility for the experiments using the PVG-integrated AUV. Letters indicate the item as follows: A, main vehicle (AUV); B, PVG; C, LDV probe for jet measurements; D, traverse for moving LDV probe; E, short-range laser distance sensor; F, air bearing carriage (slide in black); G, cart motor showing toothed belt and pulleys used to move cart; H, laser beam from long-range laser distance sensor; I, cart controller box which interfaces to cart computer; J, LDV processing engine receives back scattered light from LDV probe (C) and interfaces to DAQ computer; and K, DAQ system which interfaces to DAQ computer.

In order to ensure that the system stays within predefined bounds of the tank, a long-range laser distance sensor (optoNCDT 1182, H in figure 2.6) measures the location of the cart along the flume. The long-range distance sensor readings are used by the controller to disable the cart should the cart move past its predefined bounds. The combined values of the short- and long-range distance sensors accurately give the exact position of the vehicle in the tank. This position is then Kalman-filtered and used to obtain the position and velocity, U_∞, of the vehicle during self-propelled runs. The system is controlled by an independent computer (hereafter the cart computer) that enabled communication to the cart's on-board microprocessor controller and recording of cart's position and velocity. The cart computer was also responsible for controlling the servo controller in the AUV.

The air bearing is considered frictionless so the only resistance to the AUV motion would be fluid drag from the AUV's movement in the water and a minimal amount of influence from cables that are attached to the AUV (umbilical, tubing to air chamber, etc.). To prevent the cables from affecting the AUV's motion, a simple procedure was used to tare the setup. The cart system is activated such that the cart moves based on the AUV's position to a reference point but the AUV throttle is kept off. The cables are then adjusted until the cart is nearly motionless. This ensures that the cables do not significantly affect the results of the self-propelled runs. While the force from these cables is eliminated as much as possible via this procedure, in practice the cables tend to produce a small force. The force from the cables is generally completely overwhelmed by the magnitude of the vehicle's thrust and drag, yielding reliable results for high vehicle speeds. However, the cable force can become of significant magnitude in the presence of equally small vehicle thrust. Furthermore, the cart controller has challenges at low velocities due to backlash and lag from the toothed belt, as mentioned previously. Thus the results for U_∞ less than

(a) Overall view of the water tunnel facility.

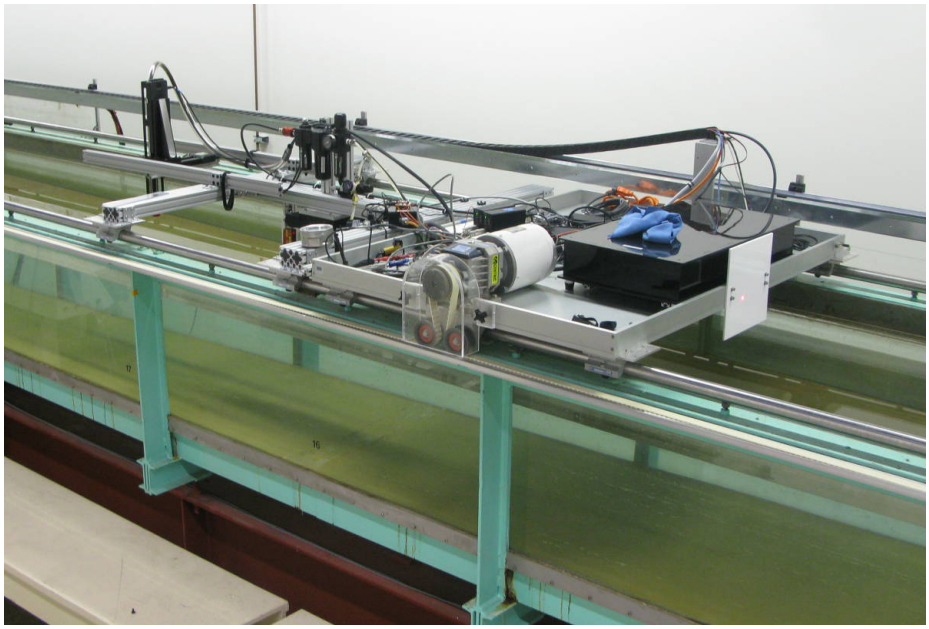

(b) Close-up view of the cart system for enabling self-propelled motion. Please refer to figure 2.6 for explanations of key components.

Figure 2.7: Photographs of the facility for the experiments using the PVG-integrated AUV.

10 cm s^{-1} are difficult to obtain.

Another feature of the cart system is that it was possible to command the cart system to follow a specified trajectory, rather than using the feedback of the vehicle's position to control the cart. This, in conjunction with a force transducer, allowed for drag measurements of the PVG-integrated AUV.

2.2.3 Drag Measurements

In order to measure the impact the addition of the PVG has on the entire AUV system, the drag force, F_D, on the overall vehicle was measured using a force transducer for both the AUV alone and the PVG-integrated AUV system. For these tests, the cart was run using a prescribed-position program that moved the cart at a specified velocity, U_∞, while the model was dragged through the water and mounted to the air-bearing and force transducer. The force transducer (Transducer Techniques LSP-10) measured the force in the axial-direction only. Each test was repeated once.

2.2.4 Laser Doppler Velocimeter Setup

For measurements of the jet velocity, a laser Doppler velocimeter (LDV) was used (C in figure 2.6). The LDV system (Measurement Science Enterprise, Inc. miniLDV) used frequency shifting to obtain the fluid velocity in the measurement volume. The LDV probe used a backscatter photo detector that was integrated into the probe body, allowing for permanent alignment of the system. The probe was mounted to a two-axis traverse system (D in figure 2.6) that gave the system 100 mm of travel in the two directions lateral to the axial direction of the AUV. The traverse and its attached LDV probe was mounted directly to the AUV cart using modular aluminum framing. As the AUV system was able

to travel many centimeters along the air bearing, there was the potential for variability in the distance of the probe volume from the aft-most tip of the PVG. However, recordings of the short-range laser distance sensor (measuring the relative position of the cart to the AUV) showed that the measurement volume was 0.23±0.05 nozzle diameters (9.3±2.0 mm) downstream of the PVG nozzle exit across all runs. The LDV system was controlled by a vendor-provided software program which controlled the traverse and data acquisition.

As figure 2.5 shows, the tube cross section can become very nonuniform. To evaluate the influence of the tube's nonuniform cross section on the flow exiting the nozzle, two high-spatial-resolution profiles were taken of the jet exit. Each profile consisted of a 11×14 grid of sampling locations spaced 5 mm apart. At each sampling location, 250 samples would be obtained before moving to the next location. These 250 samples were time-averaged to obtain the local flow velocity and showed good convergence to their time-averaged value. As each self-propelled run only generated a few tens of seconds of test time during which the submarine was steadily moving ($\partial U_\infty/\partial t \approx 0$), only a few locations would be sampled during each self-propelled run. It was decided that it would be excessively time-consuming to conduct the high-spatial-resolution tests under self-propelled conditions, and thus the submarine was kept fixed in the tank while the recirculation pumps were turned. The two run conditions chosen for analysis used τ = 0 and 10 seconds and both had T = 1300. Generally, these run conditions would result in a self-propelled AUV speed of 42 and 12 cm s^{-1}, respectively (cf. figure 2.14). Since the test was aimed at evaluating the nonuniformity of the jet exit, rather than obtaining accurate jet exit velocities for the self-propelled cases, the flow in the tank was set to approximately 20 cm s^{-1}. This discrepancy between the flume water velocity and AUV velocity was considered acceptable, again, due to the motivation behind these tests.

The results of the high-resolution LDV jet profiles are shown in figure 2.8. The spatial average of the time-averaged local velocities yielded U_j values of 1.2 and 0.74 m s^{-1} for τ = 0 and 10 s, respectively. It should be noted these values differ from the results shown later (in figure 2.15) due to differing freestream speeds between the current static tests and the later self-propelled tests. The figures show that there was nonuniformity in the resulting jet, particularly for the τ = 10 s case, and the standard deviation of local mean velocities across the exit was 5.4% and 13% of the mean of all local mean velocities for τ = 0 and 10 s, respectively. Because of the variation across the jet exit, measurements of the average jet exit velocity used the LDV probe volume centered on the jet exit and are assigned an additional error of 13% to account for the jet exit nonuniformity. This allowed for single runs to yield a complete set of results rather than having to span data collection across several runs for a given experimental condition (T, τ). It should be noted, however, that the difference between the time-averaged center line velocity and the spatially-and-time-averaged velocity across the interior of the jet yielded differences of only 4%; thus the 13% added error is considered conservative.

From the center-line velocity data obtained from the self-propelled runs, phase-averaged plots were made of the center-line velocity as a function of time. The velocity data as a function of time has significant noise, due to the turbulent nature of the jet flow and hence phase averaging is an appropriate technique to apply. These plots used the frequency obtained from the transmural pressure transducer as this frequency had less error than that obtained using the LDV velocity data. Because of the non-uniform sampling of the LDV data (sampling occurs when a particle arrives through the sampling volume, not based on a clock), the velocity data was first super-sampled using a linear interpolation technique with a sampling interval based on the smallest interval between neighboring samples from

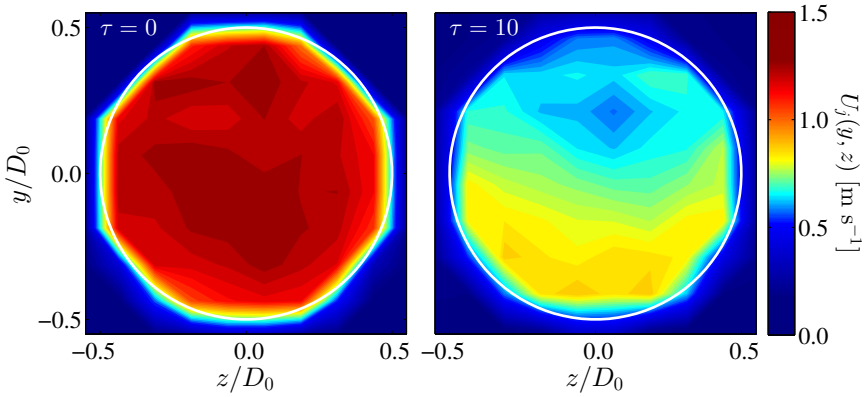

(a) Contour plot showing the spatial variation in the mean jet exit velocity. The left image is for τ = 0 s and the right for τ = 10 s. Color indicates the magnitude of the local mean velocity in the x direction (aligned with the axial direction of the submarine). The color bar indicates velocity in m s^{-1}and is matched between each plot. The lateral directions, y and z are scaled by the diameter of the jet nozzle and the outline of the nozzle exit is shown as the white ring in each of the plots.

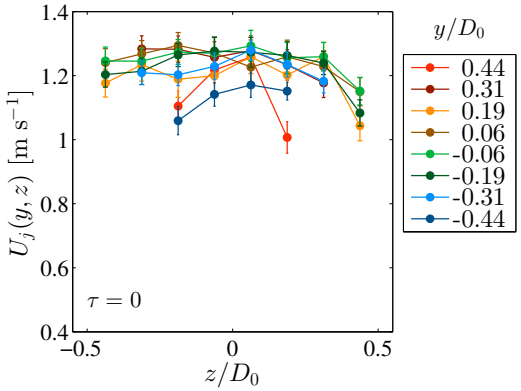

(b) Plot of the time-averaged jet velocity for τ = 0 s at each spatial location with errorbars indicating the range of the 95% confidence interval. The colors indicate different y positions while the abscissa indicates different z positions, both of which have been normalized by the jet diameter, D_0.

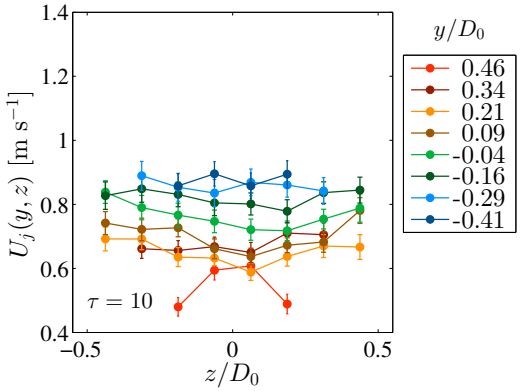

(c) Plot of the time-averaged jet velocity for τ = 10 s at each spatial location with errorbars indicating the range of the 95% confidence interval. The colors indicate different y positions while the abscissa indicates different z positions, both of which have been normalized by the jet diameter, D_0.

Figure 2.8: Plots of the jet exit profile for T = 1300 and τ = 0 and 10 s.

the original data. This super-sampled data thus preserves the original data and provides a uniformly sampled dataset to facilitate phase averaging.

Each phase included in the averaging is obtained by taking subsets of the oscillation period and their contributions to the mean. Additionally, the standard deviation of that phase of the cycle is also obtained. This provides the mean and standard deviation calculated at the precise phase of each oscillation cycle from 50 oscillations.

2.2.5 Dye Visualization

Gharib *et al.* (1998) showed that the formation time of a vortex ring has implications for its wake structure, especially as the criterion for vortex ring pinch-off when the formation time exceeds the formation number. However, since the formation number is only approximately defined and can vary (Dabiri & Gharib 2004*a*; Krueger *et al.* 2006; Mohseni *et al.* 2001; Rosenfeld *et al.* 1998), it is appropriate to not rely solely on the formation number criterion as the formation number has not been calculated for vortex rings generated from PVG devices. Thus it is necessary to visually evaluate the resulting flow field to determine the presence of vortex ring pinch-off. In order to visually interrogate the flow field, dye visualizations of the wake of the PVG-integrated AUV were done. These dye visualizations were made using a gravity-fed solution of slightly diluted food coloring. The high speed camera used in these experiments (Photron APS-RX) recorded the dye visualizations at 125 Hz and a resolution of 1024×1024 pixels. The camera recordings were activated using a software trigger that detected the nose of the submarine in the image frame and began recording. To assist in minimizing clouding of the tank by the dye, the exhaust solenoid was replumbed to instead control the dye being supplied to the vehicle. This solenoid was activated by the DAQ computer once the AUV was near the high-speed camera and remained

on for a specified duration of time. The PVG chamber was then manually exhausted at the end of each run using a needle valve.

The resulting videos show the AUV vehicle passing by the camera followed by the PVG and its dyed wake. Example frames can be seen in figure 2.9(a). As individual frames can be hard to interpret and a periodic process is being investigated, the dyed wakes were phase averaged. In order to accomplish this, the frequency of oscillation was determined from the transmural pressure data, P_t, and was used to select the frames for averaging. Because the PVG-integrated AUV is in a different position in every frame, each frame of interest was cross-correlated with a smaller cropped frame of just the aft-most portion of the PVG nozzle. This allowed for accurate tracking of the vehicle in each frame. Frames that were integer periods apart were stacked and aligned by the cross-correlated nozzle exit positions, as demonstrated in figure 2.9(b). The stacked frames were then summed in their pixel intensity values and divided by the number of frames stacked. Because each frame added to the overall phase-averaged image covered a different area of the vehicle (e.g., one frame may show mostly PVG and little of the wake whereas another frame may show mostly wake and little of the PVG), different regions of the phase-averaged frames have different numbers of phases averaged (e.g., all frames show the wake near the vehicle whereas less frames show the wake far from the vehicle). This is visible in the resulting phase-averaged dye frames as vertical bars as seen in figure 2.9(c).

2.2.6 Procedure for Self-Propelled Runs

For each self-propelled run of the AUV, two independent parameters controlled its behavior: the throttle setting, T, and the chamber fill time, τ. The general procedure for a run was as follows:

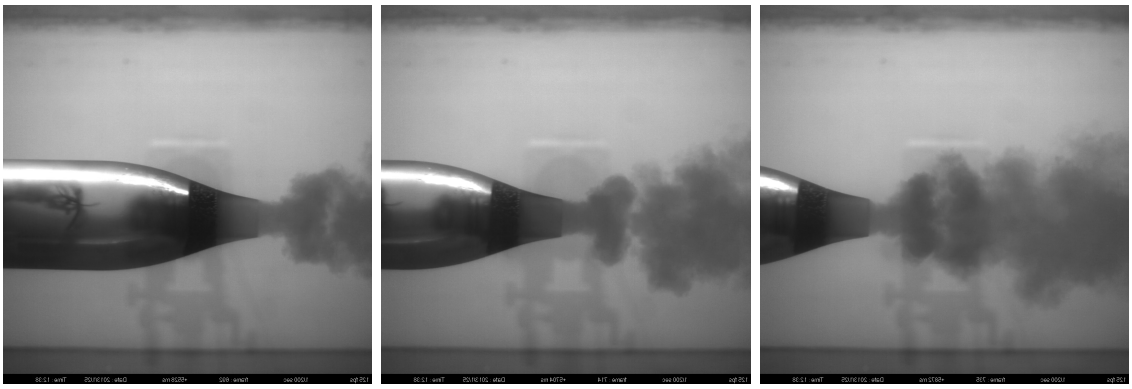

(a) Example raw frames from dye-visualization run with $T = 1700, \tau = 10$. Each frame is from approximately the same phase of the oscillation cycle and are approximately 0.16 seconds apart.

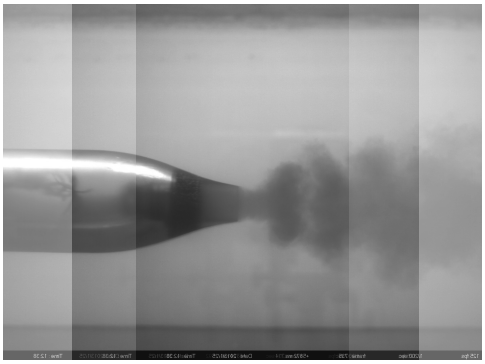

(b) Simulated stacking of dye visualization frames from Part (a), above.

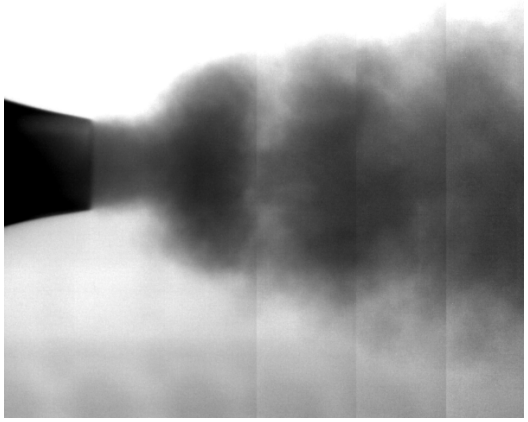

(c) Final phase-averaged result including frames from part (a) after stacking (demonstrated in part (b)) and image correction (brightness and contrast). Vertical bars are present in the wake due to video frame border (cf. part (b)).

Figure 2.9: Example results from dye visualizations of PVG wake.

1. Move cart to its starting position.

2. Fill the air chamber of the PVG for the duration specified by τ using the fill solenoid, controlled by the DAQ computer.

3. Commence data recording on both the DAQ and cart computers as the AUV propeller motor turns on and quickly spins up to specified throttle setting.

4. The AUV moves in a self-propelled manner via the cart system.

5. When the cart reaches a specified location along the tank, the cart computer turns off the AUV motor to allow the system to coast and slow down before the run halts to a finish or before the vehicle encounters the end of the tank.

6. Cart system halts once the run time elapses (generally set between 50 and 100 seconds).

7. The DAQ computer opens the exhaust solenoid to allow the air chamber pressure to recover to ambient pressure.

8. The cart system slowly returns the system to its starting position in the tank.

9. The system waits 15 seconds for the air chamber pressure of the PVG, P_e, to completely recover to ambient before ending the run.

The settling time of the tank between subsequent runs was evaluated to ensure that each run was independent. Tests were conducted at a variety of vehicle speeds and found no significant difference in results from sets of runs performed with no delay versus sets of runs performed with a delay on the order of several minutes between runs. Thus all future runs were conducted without any additional delay. For taking measurements of the jet exit

velocity, the AUV is first started on a self-propelled run. Once the cart has reached a steady velocity, the LDV recording is manually started. Before the steady velocity portion of the run ends, the LDV recording is then manually stopped.

An algorithm was developed to find the range of time at which the vehicle is steadily moving ($\partial U_\infty/\partial t \approx 0$) and, once this time segment is found, to obtain time averages of the various quantities during this time. The steady segment was found by analyzing the position and velocity data. Based on the procedure for a run, the vehicle motor turns off either at a specified position or when the duration of the run elapses (cf. step 5 above). This point marks the end of the steady segment, t_{stop} in figure 2.10. The beginning of the steady segment, t_{start} in figure 2.10, is found by finding the point early in the run where the velocity is 98% of the velocity averaged over $[t_{stop} - 1, t_{stop}]$. This yields the beginning and end points in our data where the vehicle is steadily moving itself in the tank, however is only applicable for the data from the cart computer. The cart computer recorded the vehicle speed and position, whereas the DAQ computer recorded the pressure signals and the AUV motor's current and voltage. It was initially attempted to use simultaneous recording triggers, however due to inconsistent start-up delays in recording on both of the computers, the recorded data signals were used for synchronization during processing.

Fortunately, there are landmarks in the recorded data that were able to be used to synchronize the data. To find t_{start} and t_{stop} in the data from the DAQ computer we compare two data series. The AUV motor current, I, has a square wave pattern of one period during a run, as depicted in figure 2.10. The motor turns on at the beginning of a run, which quickly drives the current high, and stays at that same speed until the vehicle reaches the specified coasting position within the tank or, less commonly, the run time elapses. For either case, as illustrated in figure 2.10, the knee in the velocity data (or the

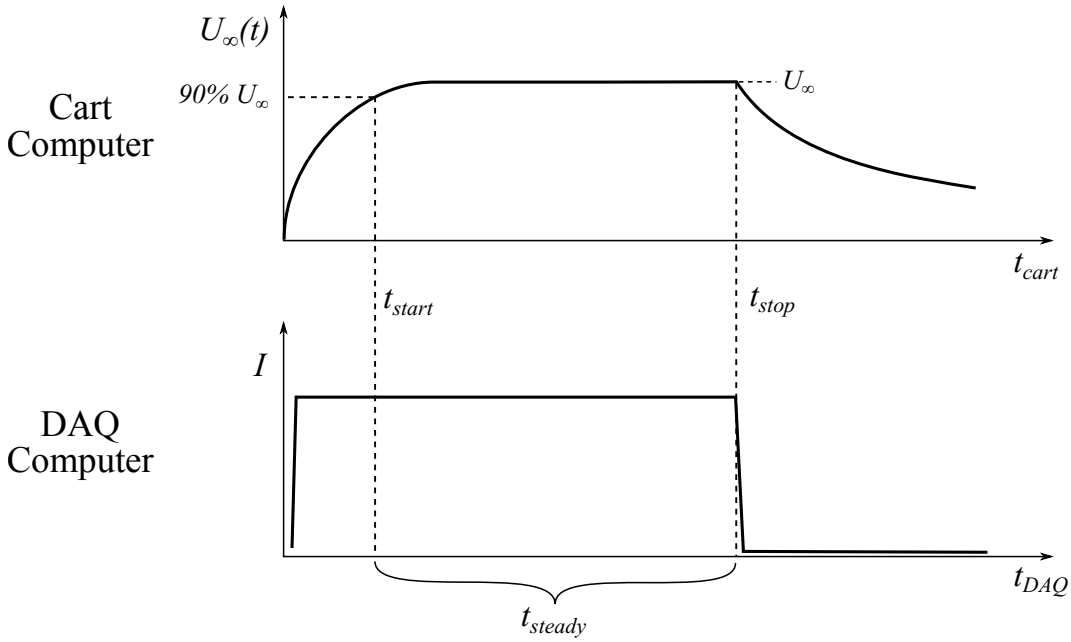

Figure 2.10: Schematic illustrating how the data is synchronized between the two computers. The top plot shows the velocity data and is taken from the cart computer with its time, t_{cart}. The bottom plot shows the AUV motor current data, I, and is taken with the DAQ computer with its time, t_{DAQ}. The dotted lines show how the steady time segment is found and how time is synchronization between the two computers.

end of the run) results from the motor turning off, which is reflected in the plot of the motor current. Thus to synchronize the data from the two computers, identifying the point where the motor current decreases significantly and aligning it with the specified coasting position from the cart computer data is all that is required. This aligns t_{stop}, as shown in figure 2.10. The error in this alignment is dependent on the thresholds used in the synchronization algorithm and is approximately 0.5 s. This error is primarily on the side of finding t_{start} and t_{stop} from the vehicle velocity data as the motor current signal yields a very reliable form. Since we already know the duration of the steady run, $t_{steady} = t_{stop} - t_{start}$, the bounds for time averaging the steady portion of the self-propelled runs for all of the data collected from both computers are set.

2.2.7 Formation Time

As discussed previously (cf. section 1.2), the formation time of the ejected fluid characterizes the vortex rings that are produced. To calculate the formation time for a pulsed jet, adjustments have to be made to the standard definition of formation time, $\hat{t}_{GRS}$, given as

$$\hat{t}_{GRS} = \frac{\overline{U_p} t_p}{D_0}, \tag{2.9}$$

where $\overline{U_p}$ is the average piston velocity, t_p is the discharge time, and D_0 is the nozzle diameter as defined in Gharib *et al.* (1998). This definition is based on the use of a piston-cylinder arrangement for producing vortex rings in a quiescent tank. However, because the present system creates a train of vortex rings from a moving system, two adjustments have to be made.

Krueger *et al.* (2003) considered the creation of vortex rings created in co-flow, where the ambient fluid is flowing parallel and in the same direction as the jetting fluid, and revised the formation time, $\hat{t}_{GRS}$, to be

$$\hat{t}_{KDG} = \frac{t_p \left(\overline{U_p} + \overline{V_c} \right)}{D_0}, \tag{2.10}$$

where $\overline{V_c}$ is the average co-flow velocity. This revised form of the formation number is appropriate for application to propulsion in particular as at steady state, the vehicle will be moving and thus the vortex rings will be formed in the presence of co-flow. A derivation of this form of the formation time is provided in appendix C.

The second adjustment is to redefine the formation time for a pulsed system rather than a one-pulse setup. Since the ejection time $t_p \sim 1/f$, where f is the oscillation frequency, we

can redefine the formation time for self-propelled pulsed jets (which are in co-flow) as

$$\hat{t} = \frac{U_j + U_\infty}{f D_0}, \tag{2.11}$$

where $\overline{U_p}$ and $\overline{V_c}$ have been replaced by U_j and U_∞, respectively. In reality, the period of pulsation, $1/f$, is greater than the ejection time, t_p, and would tend to overpredict the formation time; however, this overprediction is not present in the current experiments and the definition given is correct (cf. appendix D). The oscillation frequency is calculated from the peak in the fast-Fourier transform of the mean-subtracted transmural pressure, P_t, during the steady-state portion of the self-propelled run. Furthermore, a threshold was applied to the amplitude of the Fourier-transformed P_t in order to ensure that there was a significant periodic signal present in the pressure signal. Only runs with frequency amplitudes exceeding this threshold are considered oscillating cases. It should also be noted that the wake structure behind the vehicle could affect the co-flow velocity that the vortex ring experiences during roll-up (e.g., the wake of the vehicle could cause a velocity deficit at the nozzle edge). This phenomena was not explored as a part of this study, however is something to consider.

Figure 2.11 shows both the (false-color) planar laser-induced fluorescence image of vortex ring ejection for three formation times and an illustrated silhouette depicting the expected image of the same event using food coloring as dye and room lighting (as was done with the AUV dye visualization). For figures 2.11(a) and (b), one can see that for formation times less than the formation number ($\hat{t}/F < 1$), one expects to see the primary vortex ring along with a minimal amount of dye in its wake. Additionally, as the formation number is increased, the size of the vortex ring created increases as well. However for fluid ejections

that are greater than the formation number ($\hat{t}/F > 1$), as seen in figure 2.11(c), "bumps" along the trailing jet form. These bumps correspond to secondary vortex rings that are created after the primary vortex ring has pinched off. The example in figure 2.11(c) is from a sufficiently high formation time ($\hat{t}/F = 2$) that many secondary rings have been created in the trailing jet.

Additionally, Krueger *et al.* (2006) showed that the formation number, F, at which a vortex ring pinches off from its trailing jet, is dependent on the co-flow conditions. They expressed the co-flow conditions in terms of a velocity ratio, R_v, where

$$R_v = \frac{U_\infty}{U_j}, \tag{2.12}$$

using the current nomenclature. In particular, they conducted a series of experiments measuring the formation number at various velocity ratios ranging from $R_v = 0.0 - 0.9$ (figure 2.12). The significant feature of this plot shows that there is a sharp transition in the formation number around $R_v = 0.6$. However, above and below this transition point, the data shows a nearly linear trend. Below the transition point, a least-squares fit was obtained (using the data points marked in red) and yielded the equation $F = 4.0 - 1.8R_v$ $(0 \leq R_v \leq 0.6)$.

The explanation for the drop-off of the formation time with increasing velocity ratio was found to result from the high level of the co-flow effectively stripping the vortex ring from the shear layer, thus discontinuing any addition of the shear layer into the vortex ring. This was shown to be the case by consideration of the self-induced velocity of the vortex ring added to the co-flow velocity and compared against the shear layer velocity (Krueger *et al.* 2006). At the point of vortex ring pinch-off, the vortex ring's combined velocity (both

(a) $\hat{t}/F = 0.5$

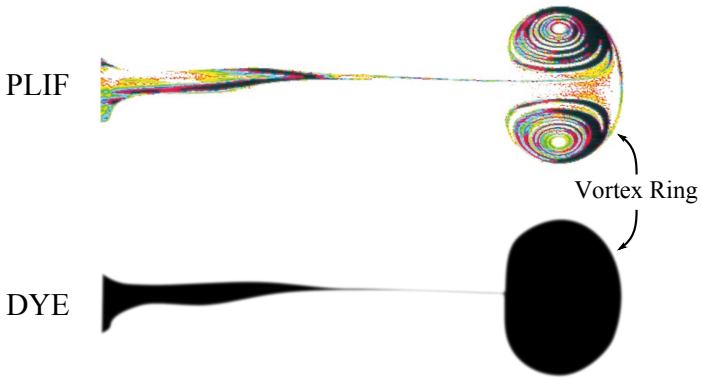

(b) $\hat{t}/F = 0.95$

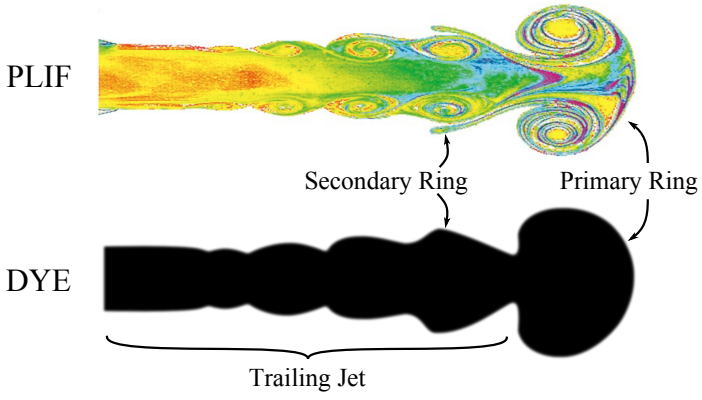

(c) $\hat{t}/F = 2$

Figure 2.11: Top image is of a false-color planar laser-induced fluorescence (PLIF) of vortex ring ejection from Gharib *et al.* (1998) © Cambridge University Press, reproduced with permission. The bottom image is a simulated dye visualization image of the same event created using a silhouette of the PLIF image.

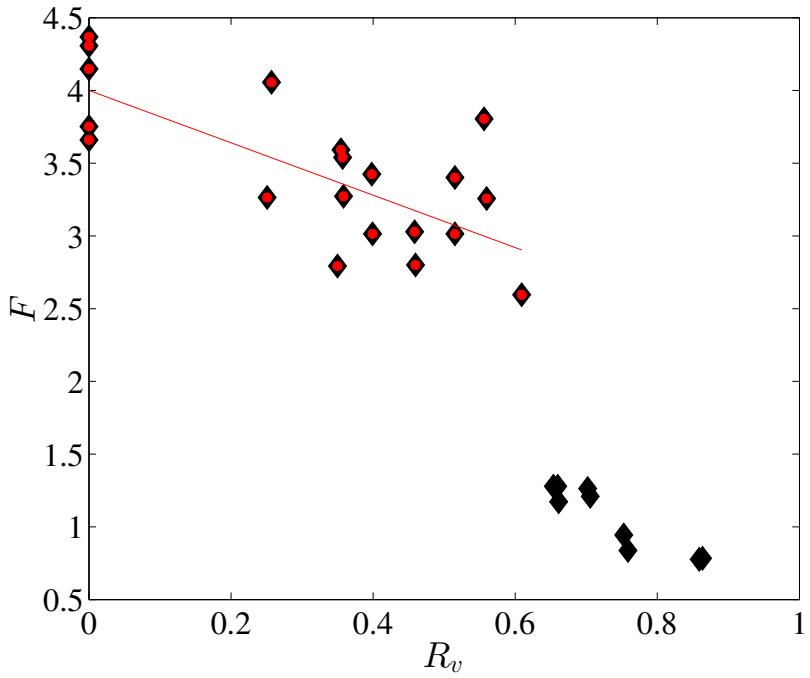

Figure 2.12: Plot of the formation number, F, versus the velocity ratio, R_v, from Krueger *et al.* (2006). For velocity ratios less than 0.6, as indicated by the red dots, a linear fit of the data was obtained and is shown as the red line.

self-induced and from the ambient co-flow) would be greater than the velocity of the shear layer and thus the vortex ring would pinch-off.

2.2.8 Error Analysis

The error for the measurements was calculated a few different ways. For measurements that yield a Gaußian distribution, the error bounds are given by the use of Student's t-distribution to obtain a 95% confidence interval for the measurement (Beckwith *et al.* 2007, pgs 55-6). A Gaußian distribution applies to the measurements of: U_∞, F_D, I, and V during the period of the run when the vehicle is moving steadily ($\partial U_\infty/\partial t \approx 0$). For the jet velocity, U_j, the distribution of these measurements is in fact Gaußian, even for the oscillating regimes, owing the significant level of turbulence in the jet. As such, the error bars for the mean jet velocity are the 95% confidence interval using the Student t-distribution in

addition to 13% of the mean value, where the latter addition is due to the non-uniformity of the jet as observed in section 2.2.4. For any quantity that is calculated based on measured values, the error is propagated by summing the product of the error in the measured value and the sensitivity of the calculated quantity to that measured value in a root-mean squared fashion (Beckwith *et al.* 2007).

2.3 Results and Discussion

2.3.1 Drag

The results for a range of velocities for the two system configurations are shown in figure 2.13(a). One can normalize the drag force by the dynamic pressure and the cross-sectional area of the AUV to yield a drag coefficient,

$$C_D = \frac{F_D}{\frac{1}{2}\rho U_\infty^2 A_V}, \tag{2.13}$$

where C_D is the drag coefficient, ρ is the density of water, and A_V is the cross sectional area of the AUV (taken to be the area of a circle with diameter 12 cm), plotted in figure 2.13(b).

The drag tests were in a range of Re_V = 200,000–900,000 based on the total vehicle length. Due to its high Reynolds number, it was expected that the drag coefficient would remain constant throughout all velocities. However, one can see that the drag coefficient only becomes constant at higher velocities, i.e., over 40 cm s^{-1}. This is believed to be due to the significant amount of mechanical vibrations that the cart experiences as it moves and are transmitted to the force transducer; i.e., vibrations from the support side of the transducer, not on the vehicle side of transducer. As the vehicle increases in speed, the

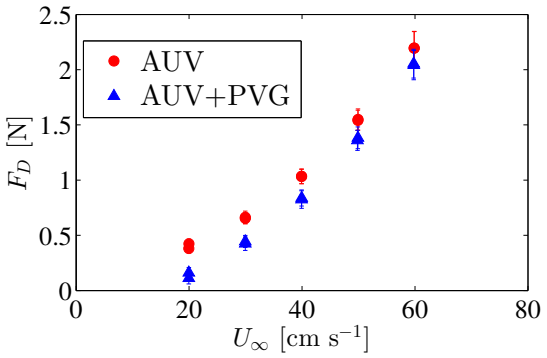

(a) Plot of the measured drag force of the AUV alone and the PVG-integrated AUV system versus the free-stream velocity of the system, U_∞.

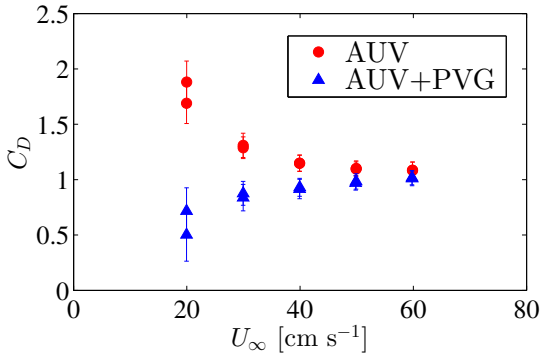

(b) Plot of the drag coefficient for the AUV alone and the PVG-integrated AUV system. The drag coefficient is given by equation 2.13 using the data from 2.13a. Error bars indicate range of 95% confidence interval.

Figure 2.13: Results of the drag measurements for the AUV and PVG-integrated AUV system configurations for two runs at each configuration and vehicle speed.

strength of the fluid drag force begins to dominate the mechanical vibrations and yields the expected plateau in the drag coefficient, as seen in figure 2.13(b). Assuming that the value of the drag coefficient at 60 cm s^{-1} is correct (as the fluid drag will have more adequately suppressed mechanical noise in the measurements), then the addition of the PVG to the AUV does not significantly affect the overall drag of the vehicle as seen by the overlapping error bars. Additionally, the divergence of the drag coefficient, C_D, for at low velocities is of note as the PVG-integrated AUV shows a lower drag coefficient than the AUV alone. This could be due to the more massive PVG-integrated AUV dampening the mechanical vibrations better than the less massive AUV alone.

2.3.2 Vehicle Speed

The mean vehicle speed measured from the combined long- and short-range distance sensor while the AUV was in steady operation is plotted in figure 2.14 for a range of T and τ. This yields a range of Re_V = 8900–1,000,000. For T = 1600–1750, there is an absence of results for low chamber fill times as these runs were attempted but they were not fully self-propelled,

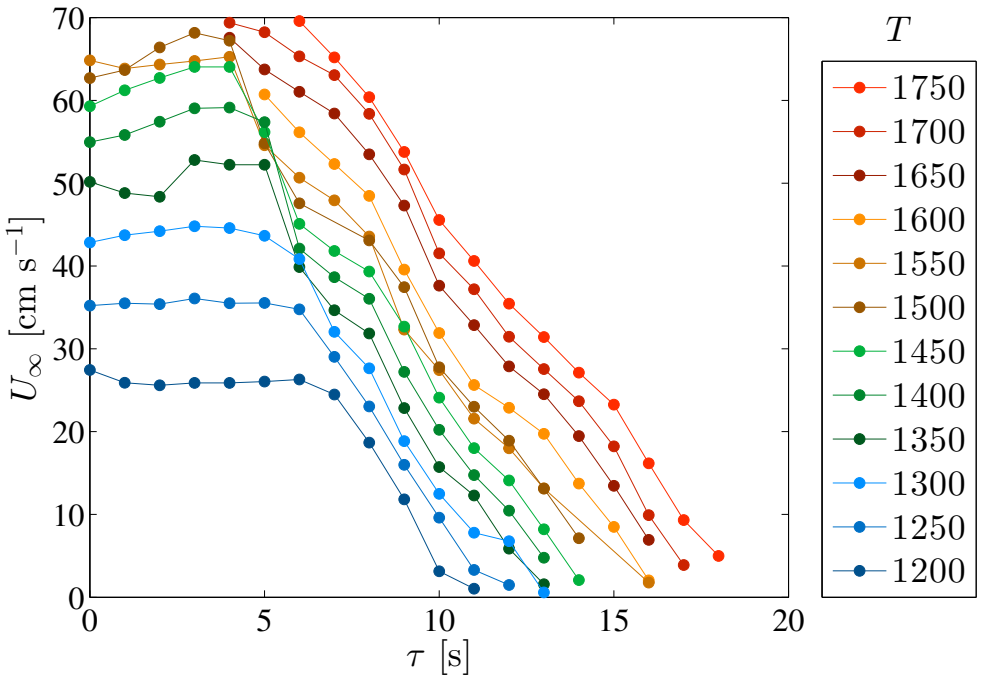

Figure 2.14: Plot of the vehicle velocity, U_∞, versus the chamber fill time for the variety of throttle settings tested. Error bars showing the bounds of a 95% confidence interval are also plotted but are hidden by the marker size.

as the cart reached maximum speed which saturates the controller output. As such, these conditions are omitted from the data set. However, the higher T settings of 1300–1750 along with sufficiently high τ slows down the AUV system enough for the cart system to provide a self-propelled run, as seen in figure 2.14. For each throttle setting tested, the chamber fill time was increased until forward propulsion was essentially extinguished.

In general, it is clear that increasing T increases the vehicle speed. Furthermore, it is seen that there is a critical τ, τ_{crit}, after which the vehicle speed begins to decrease. The value of τ_{crit} decreases with increasing throttle setting and ranges from approximately 4 to 6 s at the high to low range of T, respectively. The value of τ_{crit} also corresponds well to the onset of significant tube cross-sectional area reduction as seen in figure 2.3b. Thus the plateau in the AUV velocity at low τ is due to the tube being in an uncollapsed state and acting as a straight tube.

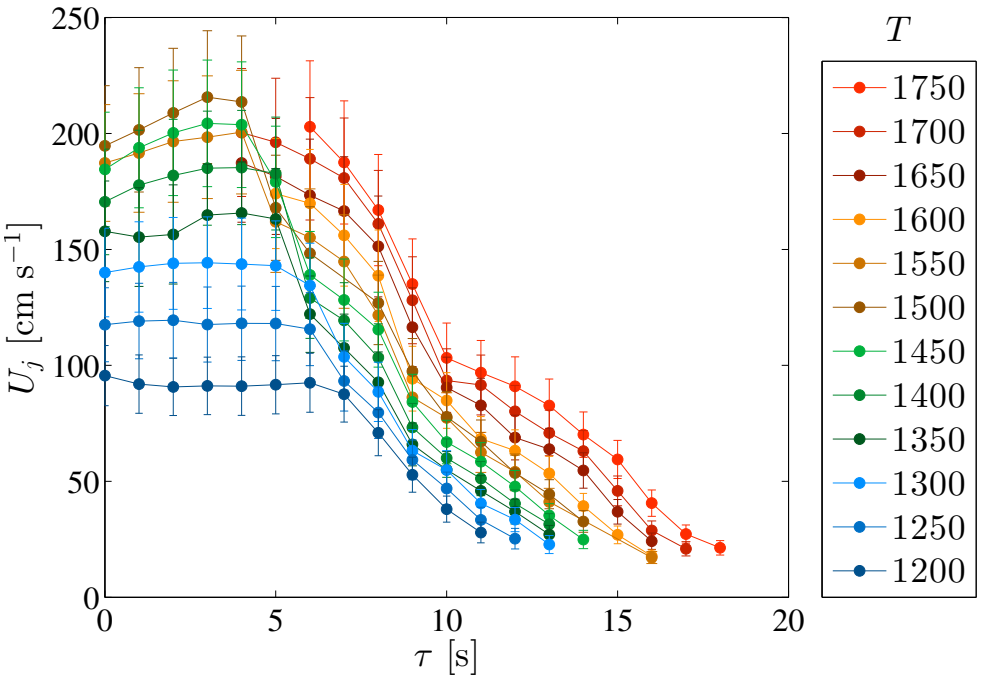

Figure 2.15: Plot of the jet velocity, U_j, versus the chamber fill time for the variety of throttle settings tested. Error bars showing the bounds of a 95% confidence interval are also plotted but are mostly hidden by the marker size.

2.3.3 Jet Velocity

The jet velocity, U_j, was measured by the LDV probe and is given in figure 2.15. These results yield a jet Reynolds number, defined as

$$Re_j = \frac{U_j D_0}{\nu}, \tag{2.14}$$

in the range of Re_j = 7000–86,000, indicating that the jet was fully turbulent. The results seam to mimic the general trends of the vehicle speed, shown in figure 2.14, where larger T yields higher velocities and that after τ_{crit}, the velocities drop quickly. This is primarily related to the increased resistance to flow due to tube collapse as τ is increased.

Figure 2.16 shows plots of the phase-averaged jet velocity as a function of time. These plots are from 50 oscillation periods that have been phase-averaged and matched based on

the trough of the oscillation period. The black line indicates the phase-averaged value of the velocity and the light gray band indicates one standard deviation from the phase-averaged value. Additionally, a dot-dashed gray line indicates the value of the overall mean of the jet velocity from all points in the original LDV data. From this dataset one can see that the jet velocity during an oscillation cycle can be generally described by a sinusoid, however there are also higher order modes present as well.

2.3.4 Oscillation Frequency

The oscillation frequencies are plotted in figure 2.17. The value of f can be seen to generally increase as T is increased. However, for a given T, there does not appear to be a strong relationship between f and τ—although a slight depression in f appears around τ = 10–12 s.

2.3.5 Efficiency

Using the results for U_j and U_∞, both measured during steady state, the Froude efficiency, η, can be calculated and yields figure 2.18 (cf. equation (1.4)). In general, as one increases T, η increases as well. Furthermore, at τ less than τ_{crit}, η is nearly constant. This τ_{crit} from the η data set is again approximately 6 seconds, which corresponds to the onset of tube collapse as seen in figure 2.3b.

At τ greater than τ_{crit}, where the tube has begun to collapse, the Froude efficiency, η, and its trend varies significantly depending on the throttle setting. For throttle values below 1300, the Froude efficiency decreases sharply with increasing chamber fill time. These decreases appear to be driven primarily by a low U_∞ manifesting as a low η. The low U_∞ is likely due to the difficulty running the cart system at low velocities (cf. section 2.2.2). For throttle settings above 1300, the trends of the Froude efficiency appear to exhibit a

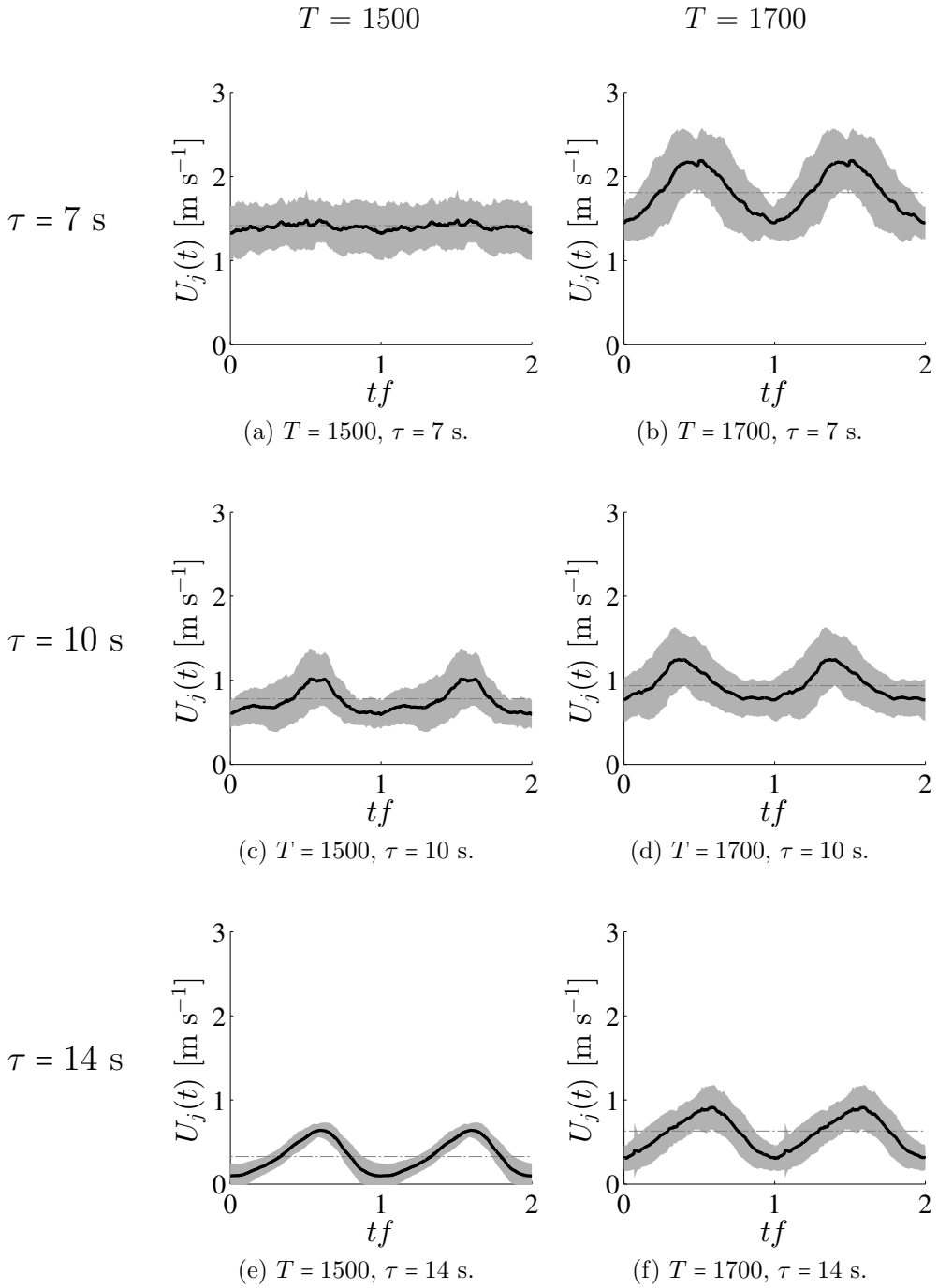

(a) T = 1500, τ = 7 s. (b) T = 1700, τ = 7 s.

(c) T = 1500, τ = 10 s. (d) T = 1700, τ = 10 s.

(e) T = 1500, τ = 14 s. (f) T = 1700, τ = 14 s.

Figure 2.16: Phase-averaged results of the jet velocity measured at the center of the jet. Each plot shows two phase-averaged oscillation cycles with time normalized by the oscillation period (thus the data is repeated). Each plot is generated from 50 oscillation periods averaged together with the phase-averaged velocity given by the thick black line with the standard deviation of the constitutive data denoted as the light gray banding. Also drawn as the gray dot-dashed line is the overall time-average from the entire set of data for those self-propelled conditions.

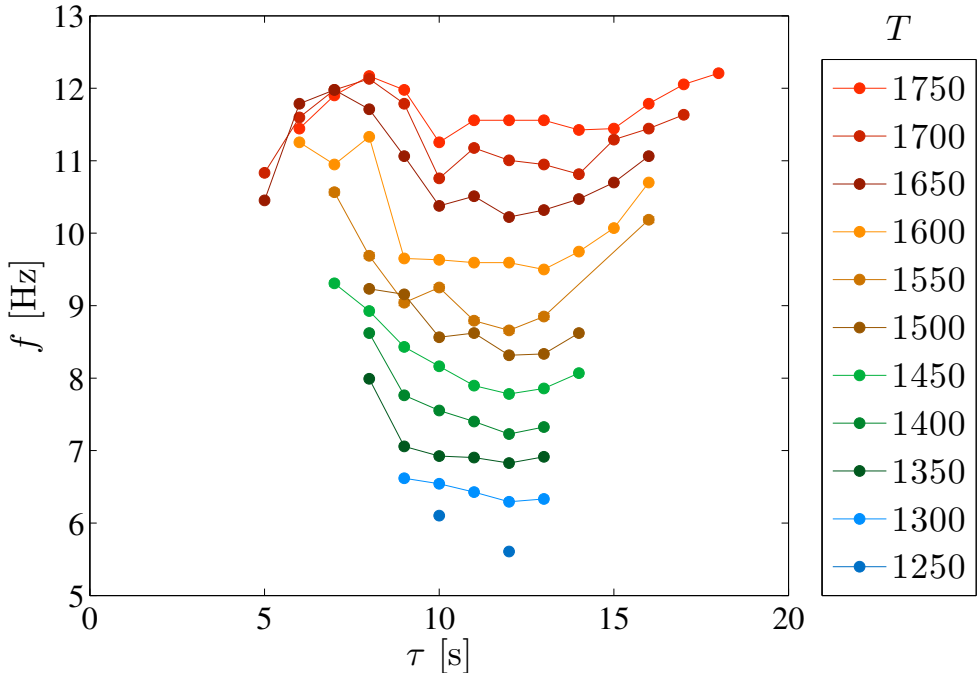

Figure 2.17: Plot of the oscillation frequency versus the chamber fill time for the variety of throttle settings tested. Error bars are plotted, however are mostly obstructed by the markers.

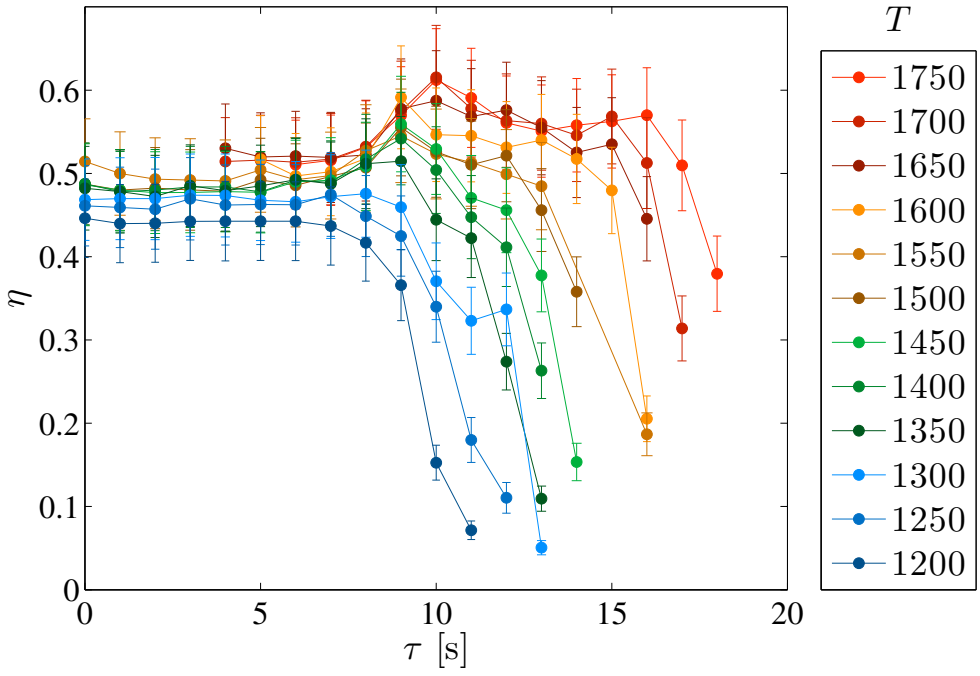

Figure 2.18: Plot of the calculated Froude efficiency, η, versus the chamber fill time for the variety of throttle settings tested. Error bars showing the bounds of a 95% confidence interval of η are also plotted but are mostly hidden by the marker size.

well-defined, local peak and then either decrease quickly or plateau briefly before dropping off. In all of these results, the sharp decreases are driven by the very low U_∞ (cf. figure 2.14).

It should be noted that the definition of the Froude efficiency in equation (1.4) assumes that the flow is completely steady ($\partial/\partial t = 0$ for all terms). However, it is clear in this case that this assumption is invalidated. A discussion of this effect and the potential of η to over- or underestimate the hydrodynamic efficiency is presented in appendix E.

Equation (2.11) was used to calculate the formation time which was used to replot the efficiency values in figure 2.19. By plotting the data in this way, the peaks that were previously spread out in figure 2.18 have become more aligned around $\hat{t} = 3.0$–3.5. Furthermore, the plot has flipped along the vertical direction as low values of η are correlated with low values of $\hat{t}$. This means for low formation times ($\hat{t} < 2$) that η decreases precipitously. The trend in η for $\hat{t} > 4$ appears to level off and plateau.

The measured R_v from the AUV system is plotted in figure 2.20. While the measured R_v from the AUV system is variable, the maximum R_v is less than 0.5. Thus the linear fit obtained from the Krueger *et al.* (2006) can be used to obtain the co-flow specific formation number, $F(R_v)$, assuming that the formation numbers measured by Krueger *et al.* (2006) apply to the PVG-generated vortex rings. For the present data, the Froude efficiency, η, versus the normalized formation time, $\hat{t}/F$, is plotted in figure 2.21.

As a comparison of the pulsed jet efficiency against the steady jet efficiency, the Froude efficiency, η, for the oscillating cases can be normalized by the Froude efficiency for the nonoscillating case, here taken to be the Froude efficiency when $\tau = 0$ s, denoted as η_0. This is plotted in figure 2.22 and appears sparser than figure 2.21 as $T > 1550$ do not have an η_0 for comparison (cf. figure 2.14). Figure 2.22 shows the potential for a 15% increase in

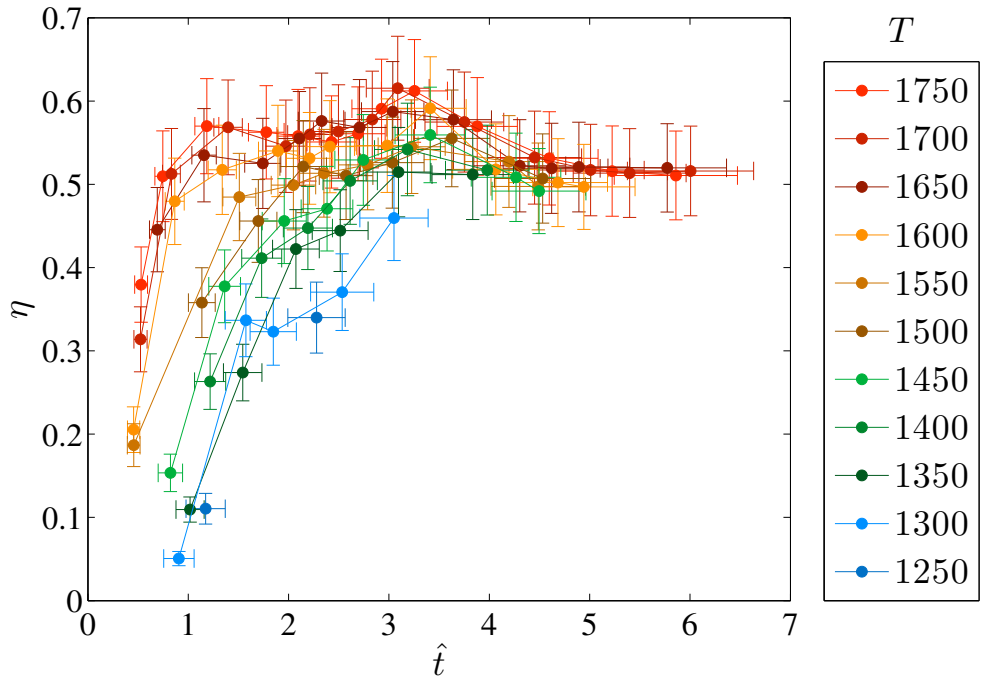

Figure 2.19: Plot of the calculated Froude efficiency, η, versus the formation time, $\hat{t}$, for the variety of throttle settings tested. Error bars show the bounds of a 95% confidence interval for both η and $\hat{t}$.

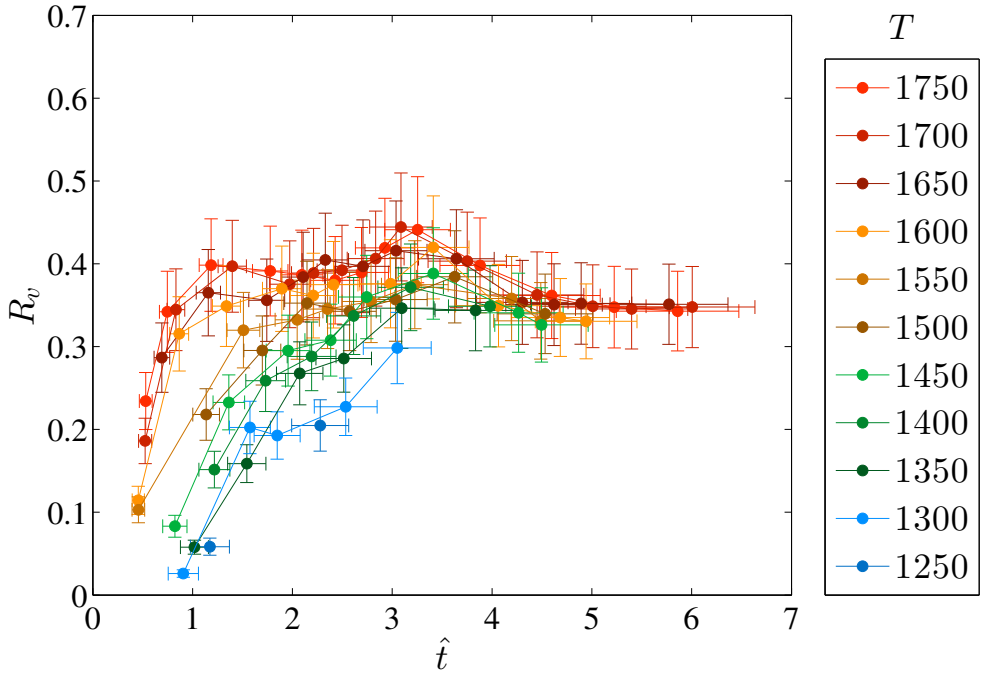

Figure 2.20: Plot of the velocity ratio, R_v, versus the co-flow formation time, $\hat{t}$, for the variety of throttle settings tested. Error bars show the bounds of a 95% confidence interval for both R_v and $\hat{t}$ are also plotted.

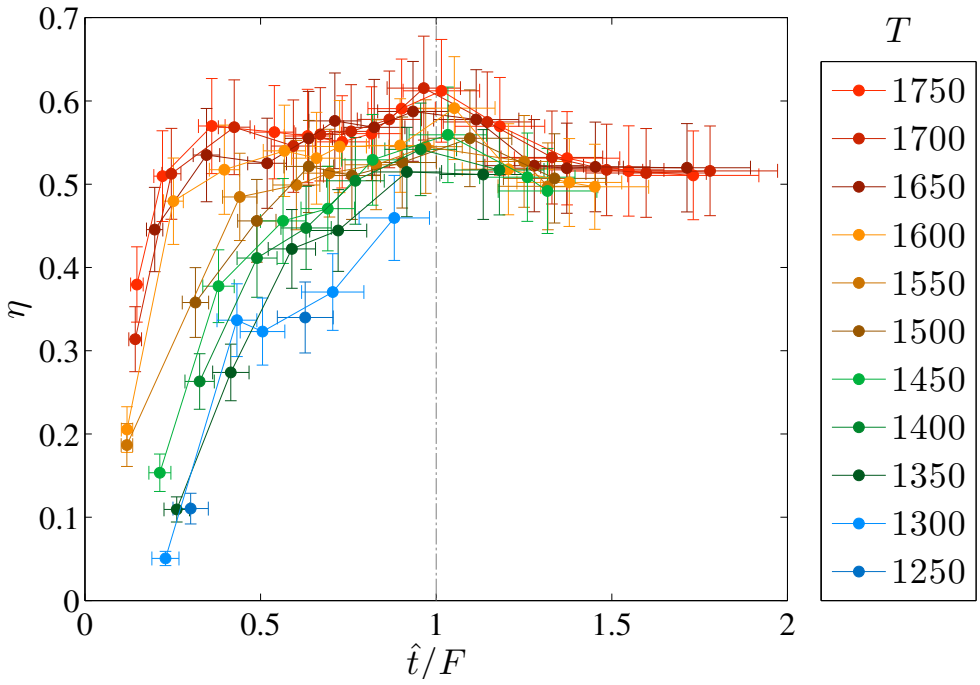

Figure 2.21: Plot of the Froude efficiency versus the normalized formation time for the variety of throttle settings tested. Error bars showing the bounds of a 95% confidence interval for both η and $\hat{t}/F$.

the Froude efficiency when the formation time for vortex ring formation is aligned with the formation number.

An alternative means of comparing the pulsed jet to the steady jet can be done by normalizing the Froude efficiency by the average Froude efficiency for $\tau = 6$, $\overline{\eta}_6$, as seen in figure 2.23. The reason for averaging at $\tau = 6$ is that every throttle setting has a data point for $\tau = 6$ and that this is within the plateau region for low τ (cf. figure 2.18). This yields a similar result to that of figure 2.22, however it allows for every throttle setting to be represented. The data from this plot indicates that an increase in efficiency over a steady jet of 22% can be obtained for higher throttle settings and when the formation time is aligned with the formation number.

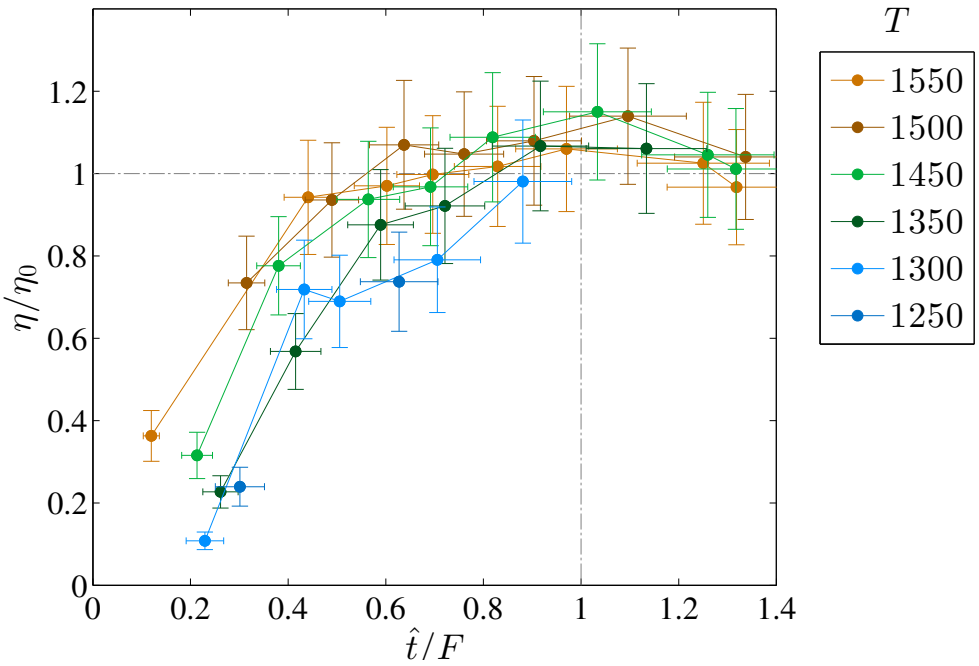

Figure 2.22: Plot of the Froude efficiency normalized by the Froude efficiency for τ = 0 s, η/η_0, versus the normalized formation time, $\hat{t}/F$, for various values of T. Error bars showing the bounds of a 95% confidence interval for both η/η_0 and $\hat{t}/F$ are also plotted.

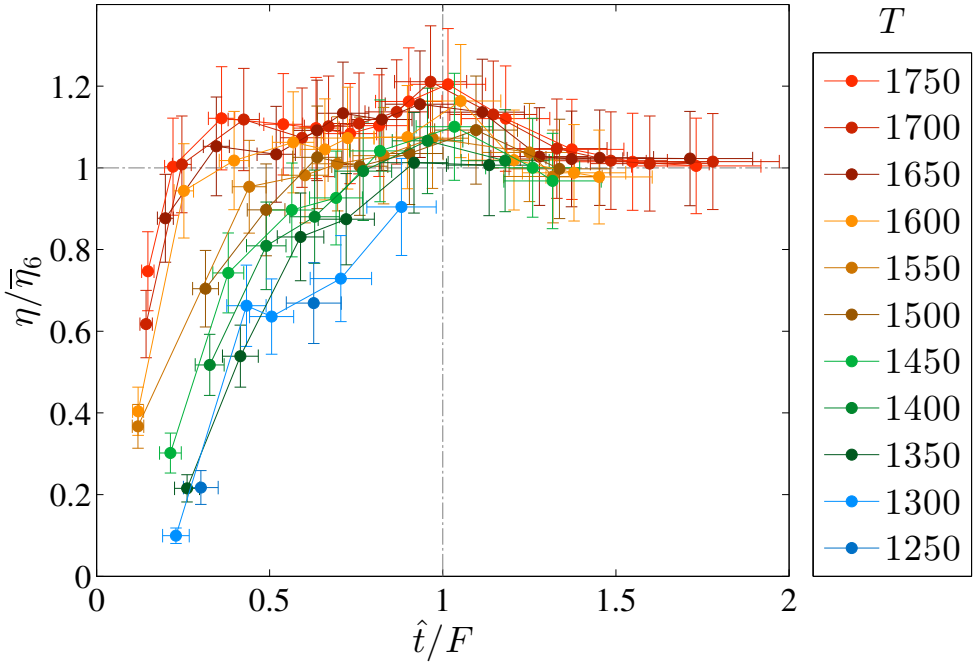

Figure 2.23: Plot of the Froude efficiency normalized by the Froude efficiency for τ = 0 s, η/η_0, versus the normalized formation time, $\hat{t}/F$, for various values of T. Error bars showing the bounds of a 95% confidence interval for both η/η_0 and $\hat{t}/F$ are also plotted.

2.3.6 Vortex Ring Formation

Figure 2.21 highlights something that was earlier obscure: the peak in the Froude efficiency, η, corresponds with the vortex ring formation number where $\hat{t}/F = 1$. To demonstrate that this is indeed the case, it is illustrative visualize the vortex ring formation at formation times below, at, and above the formation number where $\hat{t}/F < 1$, $\hat{t}/F \approx 1$, and $\hat{t}/F > 1$, respectively.

With figure 2.11 in mind, let us consider the phase-averaged frames from the dye visualization at the end of the pulsation cycle. These are arranged in figure 2.24 according to their normalized formation time. For the complete set of phase-averaged dye frames, see appendix F. There are some key differences between the single vortex ring images from figure 2.11 and the phase-averaged frames of figure 2.24. The first is that the results from the phase-averaged frames are from a series of vortex ring ejections, which create a train of vortex rings. This yields much darker images overall. Secondly, the images from figure 2.11 were taken after the vortex ring had advected many diameters away from the vortex generating nozzle. This yields a relatively thin amount of trailing dye for figures 2.11(a) and (b). This is in contrast to the images from the phase-averaged frames presented in figure 2.24 where the last vortex ring ejected is only a nozzle diameter away from the nozzle (or less). Because of this, the trailing dye is more significant than that shown in the example images of figure 2.11.

Phase-averaged dye visualizations for runs far below the formation number, $\hat{t}/F < 1$, are shown in figures 2.24(a) and (b) with normalized formation times of $\hat{t}/F = 0.31$ and 0.24, respectively. Consultation with figure 2.11(a) suggests that one should see a small primary vortex ring and negligible amounts of trailing dye. The train of dyed vortex rings in these images makes the vortex rings harder to discern, however comparison with the other

$T = 1500$ $T = 1700$

$\hat{t}/F < 1$

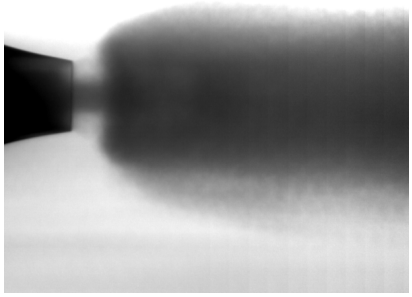

(a) $\hat{t}/F$ = 0.31. $T = 1500$ and τ = 14 seconds (also as figure F.11a).

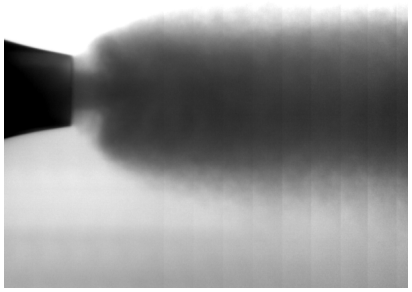

(b) $\hat{t}/F$ = 0.24. $T = 1700$ and τ = 16 seconds (also as figure F.16a).

$\hat{t}/F \approx 1$

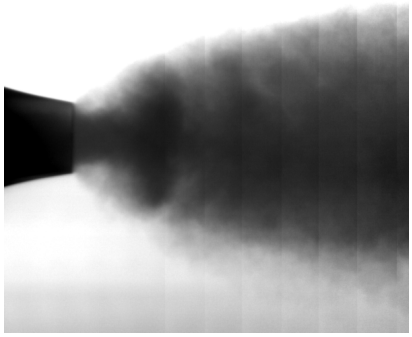

(c) $\hat{t}/F$ = 0.89. $T = 1500$ and τ = 10 seconds (also as figure F.10a).

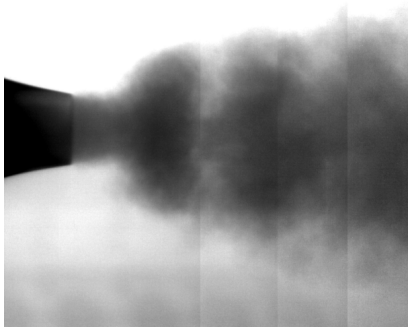

(d) $\hat{t}/F$ = 0.96. $T = 1700$ and τ = 10 seconds (also as figure F.15a).

$\hat{t}/F > 1$

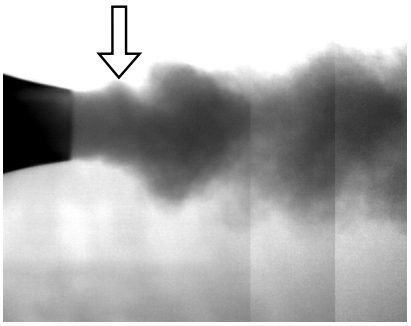

(e) $\hat{t}/F$ = 1.48. $T = 1700$ and τ = 7 seconds. Arrow indicates location of bump in trailing jet (also as figure F.14a).

Figure 2.24: Phase-averaged dye visualizations frames at the end of the pulsation cycle. For viewing the rest of the oscillation cycle, see appendix F.

images of figure 2.24 shows that the conditions in (a) and (b) yield the smallest vortex rings (compared to their higher-τ counterparts for the same T) with the least amount of trailing dye, both of which are consistent with a low-formation-time vortex ring.

Phase-averaged dye visualizations for runs near the formation number, where $\hat{t}/F \approx 1$, are shown in figures 2.24(c) and (d). After consultation with figure 2.11(b), one expects the primary vortex ring to be individually isolated and the existence of a small trailing jet may be seen. Furthermore, one should see a larger ring than with the lower formation time conditions. This is qualitatively in agreement with the phase-averaged dye visualizations. The dye visualization frames of figures 2.24(c) and (d) depicts vortex rings that appear to be larger in size than in figures 2.24(a) and (b) and there is in fact a significant amount of trailing dye. The amount of trailing dye in figures 2.24(c) and (d) is much greater than figure 2.11(b) suggests it should be, however as mentioned previously, this is likely a consequence of the image being taken when the vortex ring is close to the nozzle rather than advected further downstream (as in figure 2.11).

Finally, let us consider the case for formation times greater than the formation number where $\hat{t}/F > 1$. This is shown in figure 2.24(e) with a normalized formation time of $\hat{t}/F = 1.48$. As in figure 2.11(c), we expect to see bumps along the trailing jet from the primary ring that would indicate the formation of secondary vortices. While the primary vortex ring in figure 2.24(e) is not as coherent as in the other frames in figure 2.24, a bump trailing behind the primary ring is visible as indicated by the arrow. This bump is not a single random occurrence, but in fact is present in each pulse as this image is obtained from 4 frames phase-averaged together. This indicates that the primary vortex ring has indeed pinched off from the trailing jet. In contrast to figure 2.11(c), figure 2.24(e) shows only one secondary vortex ring is created, but that is consistent with the much lower normalized

formation time of figure 2.24(e) ($\hat{t}/F$ = 1.48 versus 2.25).

Other cases where vortex ring pinch-off is expected are shown in figure 2.25. Figure 2.25(a) shows the vortex ring formation for a normalized formation time $\hat{t}/F$ = 1.33. This is beyond the formation number and, as indicated by the arrow, a small bump can be observed along the trailing jet; this indicates vortex ring pinch-off. Other runs that yielded very high formation number are depicted in figures 2.25(b)–(d). The runs depicted in these figures have measurable oscillations (as measured by the transmural pressure signal), however it is clear that the amplitude of these oscillations in the velocity are small from the phase-averaged dye visualizations. Thus even though one may measure pressure oscillations, that is not sufficient to prove that there is a substantial shear-layer roll-up that creates significant vortex rings.

Additionally, it should be noted from figure 2.24 that the cases where $\hat{t}/F \approx 1$ show a increased rate of jet spreading which indicates higher entrainment (Ho & Gutmark 1987; Liepmann & Gharib 1992; Reynolds *et al.* 2003). Ruiz (2010) also found that a pulsed jet exhibited increased entrainment over a steady jet for a self-propelled vehicle.

2.3.7 Power Consumption

Following Ruiz (2010), it is useful to consider not only the hydrodynamic efficiency of the AUV but that of the entire system, including the power losses through the electrical wires, conversion to mechanical power through the motor, any frictional losses through the drive shaft, the propeller efficiency, and also any losses from the internal geometry of the PVG. In order to consider the system as a whole, we evaluate the total efficiency via a power coefficient

$$C_p' \equiv \frac{IV}{\frac{1}{2}\rho S U_\infty^3}, \tag{2.15}$$

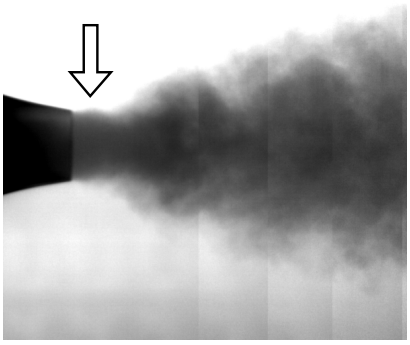

(a) $\hat{t}/F$ = 1.33. T = 1500 and τ = 8 seconds (also as ϕ = 0 of figure F.8).

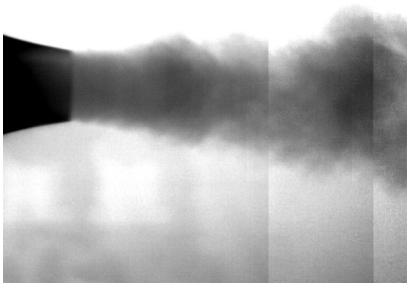

(b) $\hat{t}/F$ = 1.77. T = 1700 and τ = 5 seconds (also as ϕ = 0 of figure F.12).

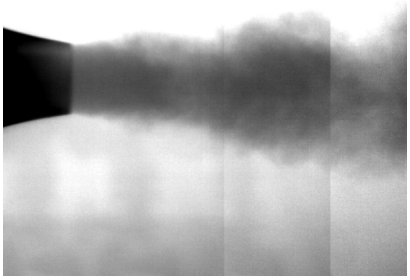

(c) $\hat{t}/F$ = 1.59. T = 1700 and τ = 6 seconds (also as ϕ = 0 of figure F.13).

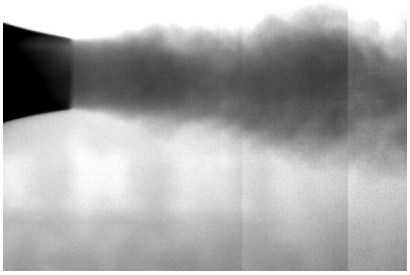

(d) $\hat{t}/F$ = 1.48. T = 1700 and τ = 8 seconds (also as ϕ = 0 of figure F.14).

Figure 2.25: Phase-averaged dye visualizations frames at the end of the pulsation cycle for conditions yielding high normalized formation times, $\hat{t}/F$. For viewing the rest of the oscillation cycle, see appendix F.

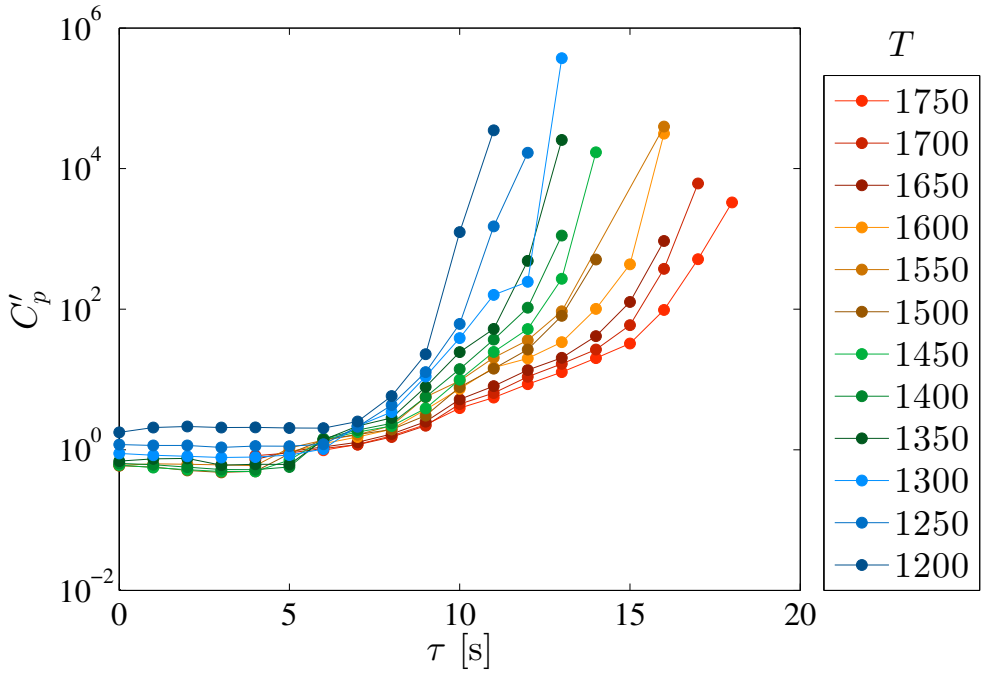

Figure 2.26: Plot of the power coefficient versus τ for various values of T. Error bars are not included, but the maximum error of the data points plotted was 9%.

where S is the external wetted area of the vehicle (Ruiz 2010). This definition physically yields the amount of electrical power required to sustain the energy of the vehicle, where lower values indicate more efficient means of propulsion. The values of C_p' for the conditions tested are plotted in figure 2.26.

In general one sees that for increasing throttle settings, the power coefficient decreases. This indicates that higher throttle settings are more efficient, which is consistent with the results of figure 2.18. Furthermore, figure 2.26 indicates that the lowest power coefficients are obtained for low values of τ; in fact, the lowest C_p' values for a given T are for $\tau < \tau_{crit}$. This indicates that while the hydrodynamic efficiency of the vehicle may have increased 22% through the addition of the PVG, that the overall system has suffered due to the significant flow losses through the PVG.

2.3.8 Discussion

The observed peak in efficiency shown in figures 2.22 and 2.23 correlates well with the work of Krueger (2001), who showed that the average thrust per pulse is maximized at pinch-off and even after normalizing the average thrust by the dynamic pressure the conclusion holds. Later work by his group involved the use of a pulsed-jet vehicle, named "robosquid," which uses a motor-driven piston to propel itself, as mentioned in section 1.3. The current results of the PVG-integrated AUV are distinct from "robosquid" in several respects. In particular, work reported by Moslemi & Krueger (2010, 2011) measured the relative efficiency of "robosquid." These results have been reproduced in figure 2.27. It should be noted that the formation number for these studies are actually based on the $\hat{t}_{GRS}$ definition, but for these tests $R_v = 0.05 - 0.10$ and thus the $\hat{t}/F$ plotted is expected to be only 5-10% off of the true value. It is expected that their relative efficiency, η_P/η, is comparable to the normalized Froude efficiency, η/η_0, used in the current study.

The results of Moslemi & Krueger (2010, 2011) show nearly a monotonic decrease in the normalized efficiency, η_P/η as the formation time $\hat{t}/F$ is increased. This is contrast to the current study where a peak in efficiency occurs at $\hat{t}/F = 1$. It should be noted that the peaks in η/η_0 for the PVG-integrated AUV were obtained at $Re_V \approx 480,000$; a higher Re_V than that of Moslemi & Krueger (2011) by over an order of magnitude. However at the relatively high Re_V of both vehicles one would generally have expected that the flow would become Re_V-independent.

Later work in the same group examined variations in the inlet geometry through aftward and foreward inlets and variations in the nozzle geometry though a blunted exit and orifices of two different diameters at $Re_V = 210$–850 (Nichols & Krueger 2012). These results are shown in figure 2.28 where the normalized propulsive efficiency, η_P/η, is defined the same

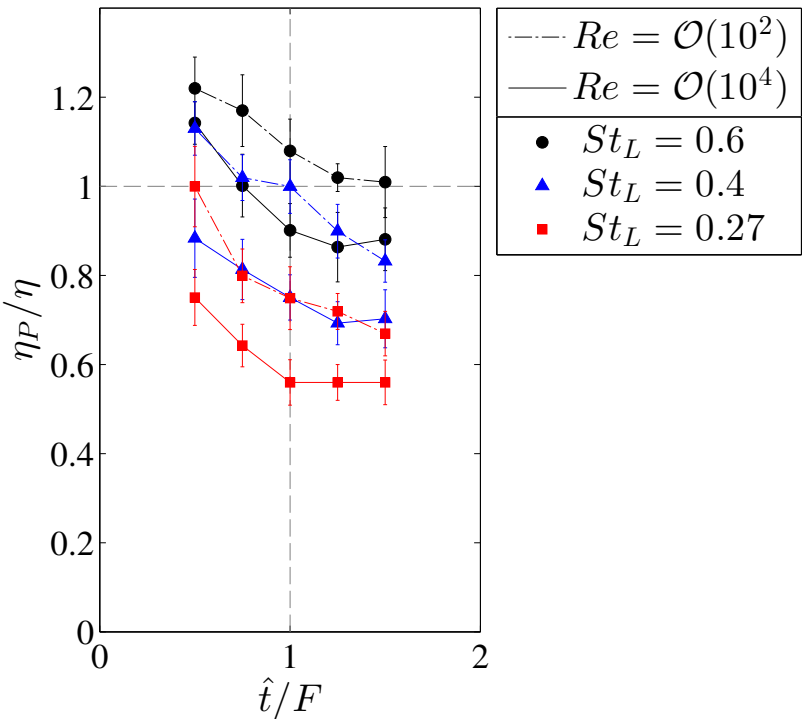

Figure 2.27: Plot of the ratio of the pulsed jet to steady jet propulsive efficiency, η_P/η, versus the normalized formation time, $\hat{t}/F$, from Moslemi & Krueger (2010, 2011) where $F = 4$ is assumed. As Moslemi & Krueger's vehicle was driven by a piston, they were able to control both the formation time of the pulses as well as the speed of pulsation, non-dimensionalized here such that $St_L = ft_p$ where t_p is the pulsation time duration, which are indicated by the different markers. The line style indicates the range of Reynolds number from the tests, where Moslemi & Krueger (2011) yielded $Re_V = 290$–470 ($\mathcal{O}(10^2)$) and Moslemi & Krueger (2010) (via (2011)) yielded $Re_V = 10,200$–$21,100$ ($\mathcal{O}(10^4)$).

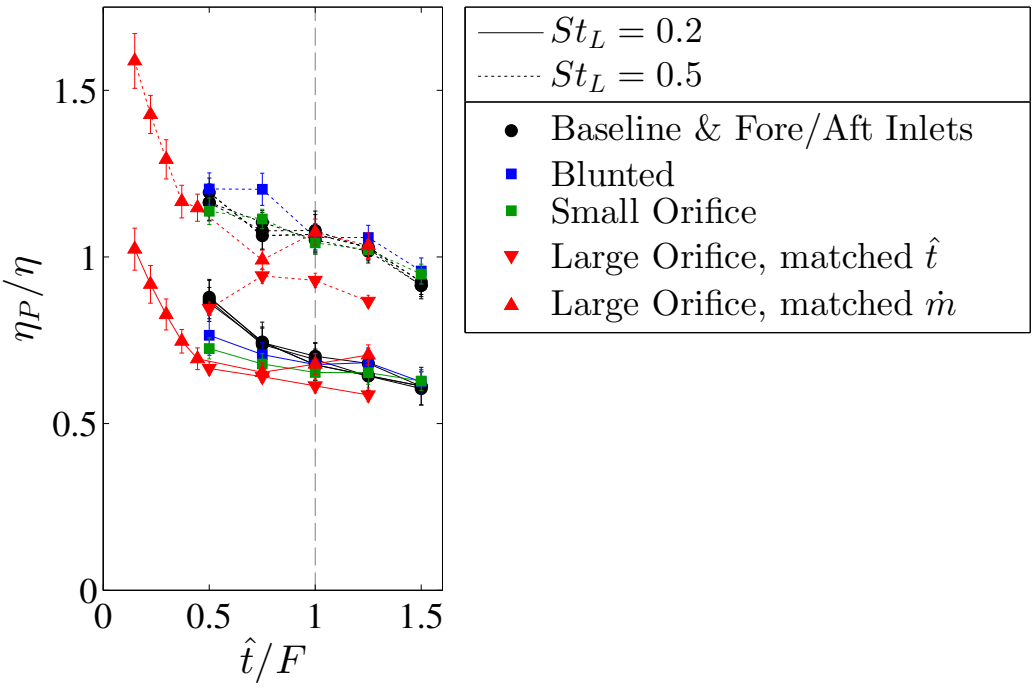

Figure 2.28: Plot of the ratio of the pulsed jet to steady jet efficiency, η_P/η, versus the normalized formation time, $\hat{t}/F$, from Nichols & Krueger (2012) where $F = 4$ is assumed. As Nichols & Krueger's vehicle was driven by a piston, they were able to control both the formation time of the pulses as well as the speed of pulsation, nondimensionalized here such that $St_L = ft_p$ where t_p is the pulsation time duration, which are indicated by the different line styles. The marker and color indicate the variations of the vehicle from the baseline configuration.

as in Moslemi & Krueger (2010, 2011). Broadly, they found similar results to Moslemi & Krueger (2010, 2011) where decreases in $\hat{t}/F$ yield increases in η_P/η. In particular, they found that the inlet variations had little to no effect on the normalized propulsive efficiency, η_P/η. However, the different nozzles did yield a measurable effect.

In general, the different nozzles show the same characteristic performance trends seen before, where decreases in the formation time, $\hat{t}/F$, yield increases in the efficiency, η_P/η, as seen in figure 2.28. However, of note is the case of the large orifice nozzle. When the η_P/η is calculated, one can see a slight peak around the formation number for a nondimensional frequency of $St_L = 0.5$. However, this peak is not nearly as significant as the peak described in the current study as it is clearly overshadowed by the high efficiencies at lower formation

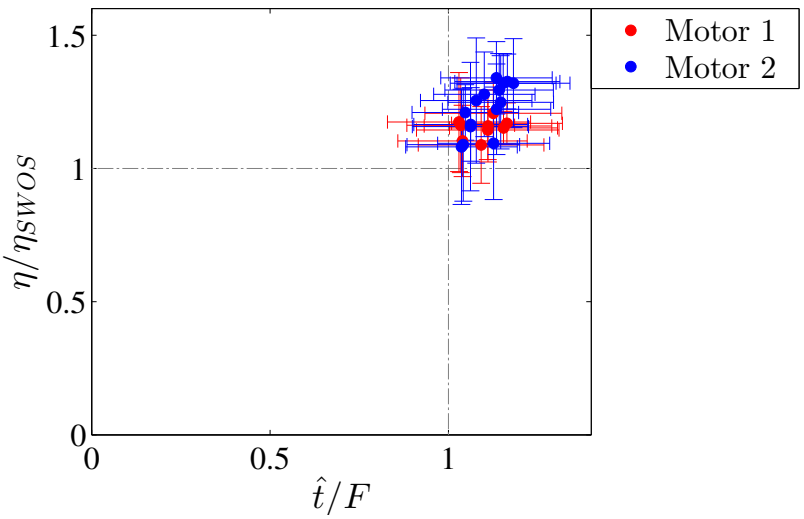

Figure 2.29: Plot of the ratio of the pulsed jet to steady jet efficiency, η/η_{SWOS}, versus the normalized formation time, $\hat{t}/F$, from Ruiz (2010) where F is calculated based on the linear fit to the R_v value from Krueger *et al.* (2006). In the work of Ruiz, the submarine used two different motors and the data is segregated based upon the motor used for the tests. As such, the different colors indicate the different motors used.

time.

The other body of work on self-propelled vehicles that use vortex rings for propulsion was done by Ruiz *et al.* (2011). Ruiz *et al.* used a custom-designed submarine that modulated the inlets using a rotating shell that was geared to the motor shaft. For the control experiments, the vehicle was operated with the rotating shell removed, a case coined "SWOS" for "steady [jet] without shell." Thus the normalized efficiency is plotted as η/η_{SWOS} and are plotted against the normalized formation time (using the linear fit to the velocity ratio from Krueger *et al.* (2006) to correct for co-flow due to being self-propelled) in figure 2.29. The definition for the formation time plotted in figure 2.29 uses the current definition given in equation (2.11), rather than the definition used in the sourced work.

The results plotted in figure 2.29 indicate that the vehicle operated in a fairly narrow regime in both efficiency and formation time space. It is interesting that while the rotation rate of the shell ranged from 8.5–12.5 Hz, the jet and vehicle speed adjusted to maintain a

relatively small range of formation time. Because of the small parameter range explored, it is not possible to explore any trends in the data. However, it is worth noting that the data is slightly beyond the formation number, indicating that the vortex ring size was likely maximized. This could explain why the mean normalized efficiency values of these points lie above unity.

Figure 2.30 compiles the results of Moslemi & Krueger (2011); Nichols & Krueger (2012) and Ruiz (2010) along with the current work in a single plot. This allows for easier comparison amongst the results of the different researchers and platforms used. In particular, the results of Ruiz align well with the peak observed in the current data set as mentioned previously. However, it is also clear from these compiled results that while all of these vehicles were shown to produce vortex rings, there is no clear overall trend amongst the different vehicles in regards to the normalized efficiency as a function of the formation time. In particular a significant variance occurs in the behavior for low formation time. The "robosquid" vehicle (Moslemi & Krueger 2011; Nichols & Krueger 2012) found that decreasing formation time yielded a monotonic increase in the efficiency whereas the current results find the opposite. It is difficult to determine why this discrepancy exists, as it could be an effect of the different Reynolds number regimes ($Re_V = \mathcal{O}(10^2\text{–}10^4)$ for "robosquid" versus $\mathcal{O}(10^5)$ for the current work) or simply a function of the vehicle geometry and the mechanism for producing vortex rings.

To help address this discrepancy, we can consider some more recent work in this area. A study by Krieg & Mohseni (2013) also considered the effects of nozzle geometry and conducted a series of experiments exploring orifice versus tube geometry. Their findings showed a 70%–75% increase in the impulse and a 105%–135% increase in the kinetic energy of a jet produced by an orifice over a tube. Because of the greater increase in the kinetic

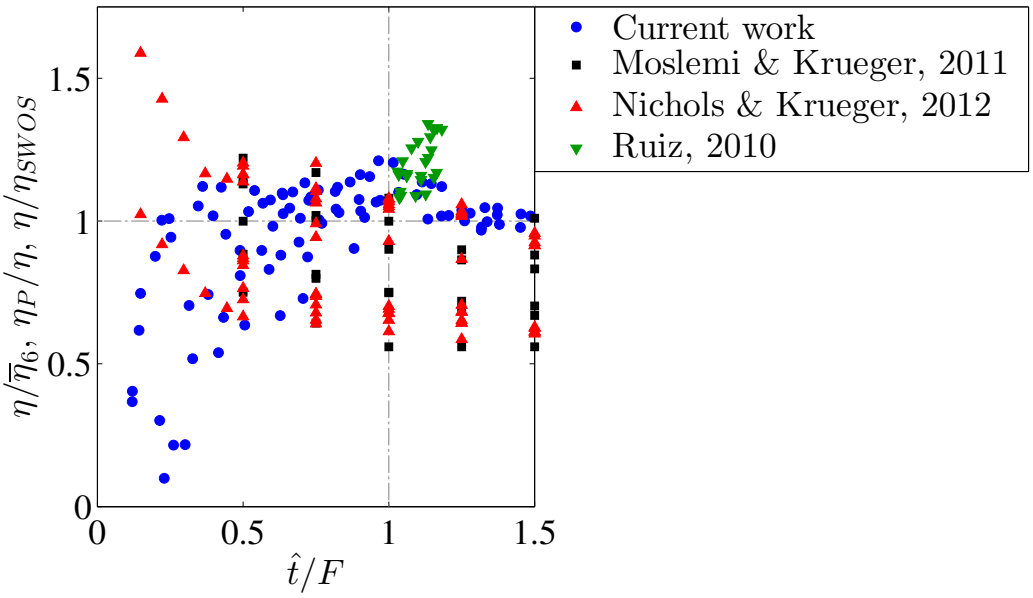

Figure 2.30: Compiled results showing all of the data points from Moslemi & Krueger (2011); Nichols & Krueger (2012), Ruiz (2010), and the current work.

energy than in the impulse, one would expect that Nichols & Krueger (2012) would have found that the orifice designs are less efficient in their study of a self-propelled vehicle. It should be noted that these measurements are only based on the resulting flow field and without consideration of the pressure field, which has been found to be an important contribution in unsteady flows (Krueger & Gharib 2005). However, in figure 20 of Krieg & Mohseni (2013), they show that the overpressure at the exit is sustained for a far longer time in the orifice geometry than in the tube geometry. This could yield a higher efficiency for vortex rings created through orifices rather than tubes, due to an increased contribution to nozzle exit overpressurization.

2.3.9 Model Predictions

Ruiz *et al.* (2011) developed an analytical model for predicting the efficiency of a pulsed-jet vehicle. Under various assumptions such as $\hat{t}/F < 1$ and that the frequency of oscillations f are sufficiently high such that $\partial U_\infty/\partial t \approx 0$, the efficiency of the vehicle, η_R, can be expressed

as

$$\eta_R \approx \frac{2}{3}\left(1+\alpha_{xx}\right)\frac{U_\infty}{U_j}, \tag{2.16}$$

where α_{xx} is the added mass coefficient for the forming vortex ring. Using the dye visualizations shown in figure 2.24 of the vortex rings at the end of the pulsation cycle, the shape of the vortex bubble can be obtained. The vortex bubble is defined as the volume of fluid that moves with the vortex ring (Maxworthy 1972). Generally, the vortex bubble can be obtained through streamline analysis (Dabiri & Gharib 2004*b*; Shariff & Leonard 1992), dye visualization (Shariff & Leonard 1992), or, more recently, Lagrangian coherent structures (LCS) (Shadden, Dabiri & Marsden 2006). It was suggested by early observers such as Maxworthy (1972) that measuring the vortex bubble via dye visualization would produce an underestimation of the true bubble volume. Olcay & Krueger (2008) conducted a study of fluid entrainment by vortex rings and measured the vortex bubble size using all three methods. They found that in all cases, the dye method underestimated the vortex volume and that the error increased in time, as the vortex volume increased through entrainment and diffusion of vorticity but that the dye did not reflect this. Olcay & Krueger (2008) also found that there was close agreement between the streamline and LCS methods but that in general, the streamline method also underpredicts the vortex bubble volume, which is in agreement with the results of Shadden *et al.* (2006).

While it is known that the volume of the vortex bubble will be underpredicted by using the dye method, Olcay & Krueger (2008) show that at at the end of a pulsation cycle (if we assume a 50% duty cycle) that this error is, at worst, 10% of the volume and thus we assume that this results in a 3% error in any one dimension of the vortex ring (e.g., 3% error in the thickness, and 3% error in each lateral direction from the axis).

Under the assumption that the vortex ring can be modeled as an oblate ellipsoid of revolution, the resulting vortex bubbles are approximated using ellipses as shown in figure 2.31. Using the major and minor axes sizes from these fits, a ellipsoid of revolution can be constructed and used to calculate the added mass coefficient for the vortex bubble. The equation for the added mass coefficient of an ellipsoid is given by Green (1835) and is evaluated numerically with the error bounds obtained by perturbing the ellipsoid axes 3%. The calculated added mass coefficients ranged from 0.98–1.17 which reflect the significant oblateness of the vortex bubbles. Using equation (2.16), the pulsed jet efficiency can be calculated and is compared to the standard Froude efficiency as shown in figure 2.32. In general, one can see that the pulsed jet model yields results that are consistent with the Froude efficiency. Thus one could expect to see a similar trend in the pulsed jet efficiency, η_R, with a peak in efficiency around $\hat{t}/F = 1$ as was found in the Froude efficiency results.

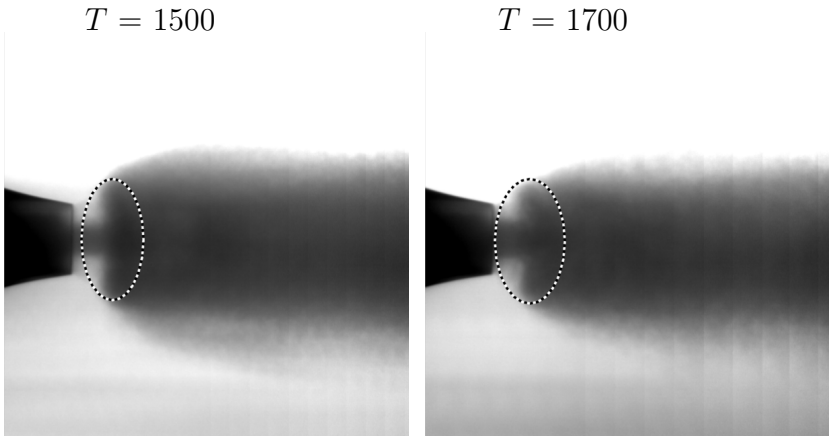

(a) $\hat{t}/F$ = 0.31. $T = 1500$ and τ = 14 seconds. $\alpha_{xx} = 1.09 \pm 0.06$ (also as figure F.11a).

(b) $\hat{t}/F$ = 0.24. $T = 1700$ and τ = 16 seconds. $\alpha_{xx} = 0.98 \pm 0.05$ (also as figure F.16a).

(c) $\hat{t}/F$ = 0.89. $T = 1500$ and τ = 10 seconds. $\alpha_{xx} = 1.08 \pm 0.06$. (also as figure F.10a).

(d) $\hat{t}/F$ = 0.96. $T = 1700$ and τ = 10 seconds. $\alpha_{xx} = 1.17 \pm 0.07$. (also as figure F.15a).

Figure 2.31: Ellipses are fit to the dyed vortex ring visible at the end of the pulsation cycle. These ellipses are representative of the vortex bubble volume.

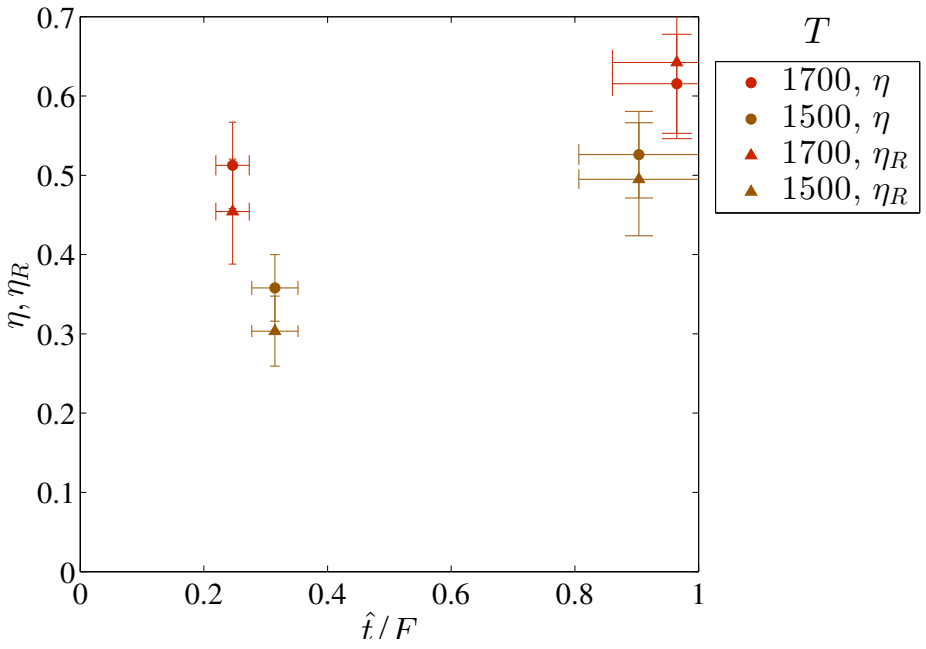

Figure 2.32: Plot of the pulsed jet efficiency, η_R, and the Froude efficiency, η, versus the normalized formation time, $\hat{t}/F$, for two values of T. The conditions plotted have their wake structures and vortex bubbles shown in figure 2.31.

Chapter 3

Parameter Study Experiments

3.1 Introduction

A series of experiments exploring how physical parameters affect the frequency of oscillations of collapsible-tube based devices was conducted. Section 3.2 presents the setup of the experiments. Section 3.3 details the methods used to obtain the results. Lastly, section 3.4 describes the results of these experiments followed by a discussion.

3.2 Experimental Setup

The general design of the passive vortex generator (PVG) used in this study is shown in Figure 3.1, with the values of key dimensions for each device given in table 3.1. The PVG consists of a collapsible tube enclosed within an airtight box. A steady flow of water enters the airtight box through a rigid tube and continues through the collapsible tube, made of silicone, before exiting via another rigid tube into the ambient liquid. By adjusting the flow rate through the tube and the pressure within the airtight box, the collapsible tube spontaneously produces self-excited oscillations. This design is distinct from earlier Starling resistors (and collapsible-tube experiments) as the flow exits through a nozzle into ambient fluid rather than through a tube to recirculate within the experiment (Bertram 2003 and

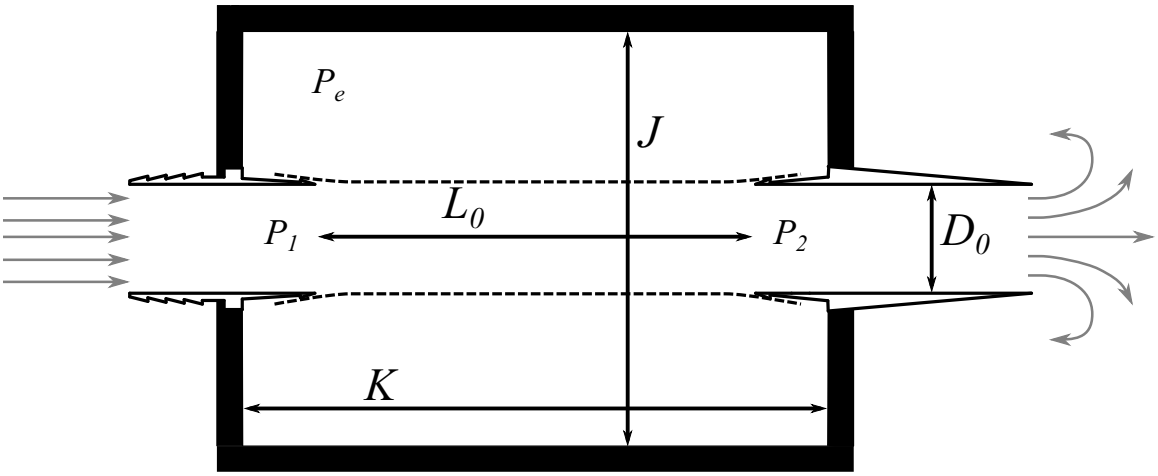

Figure 3.1: Schematic of the PVG design with key dimensions marked. The collapsible tube is indicated by the dashed line and water flows from left to right through the device, as indicated by the grey arrows. Values of the key dimensions are given in table 3.1.

references therein, Bertram & Tscherry 2006, and Bertram *et al.* 2008).

The pressure within the chamber box and external to the tube is denoted P_e, and the pressures upstream and downstream of the collapsible segment are denoted P_1 and P_2, respectively (figure 3.1). A series of PVGs with tube diameters, D_0, of 19, 38, and 57 mm were built and will be referred to henceforth by their relative nozzle size as small (S), medium (M), and large (L) respectively.

Because the mechanism that drives these oscillations is still undetermined, it was not immediately apparent whether the length of the collapsible tube should be coupled to the diameter or left constant. If the length was a constant multiple of the diameter, then the tubes of various diameter would maintain the same scaled shape. Since flow separation is a theorized mechanism for the oscillations, then having a constant shape could maintain the same flow separation characteristics as both the tube length and diameter are scaled. Alternatively, it is useful to isolate the diameter as the sole variable in a set of experiments. Because of these two considerations, a set of experiments were conducted with keeping both the shape of the tube constant and the length of the tube constant. For the constant shape

Table 3.1: Significant dimensions and parameters for each nozzle tested. The boxed table cells indicate the two sets for comparison—one set where L_0/D_0 is constant and another set where L_0 is constant. The PVG dimensions are labelled in figure 3.1.

Case	S-4	M-4	L-4	M-6	S-12
Tube Diameter, D_0 (mm)	19	38	57	38	19
Tube Length, L_0 (mm)	77	152	228	228	228
Chamber Height,[a] J (mm)	68	145	227	145	68
Chamber Length, K (mm)	129	205	281	281	281
$h/D_0 \times 100$	2.6	1.3	0.9	1.3	2.6
L_0/D_0	4	4	4	6	12
K_P (N m^{-2})	4.0	0.50	0.15	0.22	0.44
$K_{P,\infty}$ (N m^{-2})	260	32	9.5	32	260

[a] The depth of the chamber is the same as the height

experiments, a series of nozzles were tested with the length of the collapsible section of the nozzle fixed at $L_0 = 4D_0$. This yielded the series of nozzles denoted as S-4, M-4, and L-4 with the suffix indicating the L_0/D_0 ratio of the nozzle, as seen in table 3.1. The other set of experiments was conducted with the length constant and the nozzles used for these experiments were the L-4, M-6, and S-12 nozzles, as seen in table 3.1. The volume ratio, λ, was kept constant across all nozzle sizes at approximately $\lambda = 24$.

The collapsible tube of each PVG was formed using 0.5 mm thick silicone sheets with a Shore durometer hardness of 35A (Marian Chicago, Inc. HT6135). The collapsible tube was constructed by wrapping a rectangular sheet on itself to create a hollow cylinder. The seam overlap was typically 5 mm in size, and the seams were secured using aquarium silicone sealant (Dap 00688). The tubes were designed to have nominally the same diameter as the nozzle, such that at low chamber pressures the PVG would act as a straight tube. This yielded tubes with a tube thickness to diameter ratio (h/D_0) in the range of 8.7×10^{-3}–2.6×10^{-2}. This was believed to create tubes that had sufficiently thin walls as to have negligible effect on the tube bending. However, a later investigation into the tube properties

explored the bending stiffness of the tubes. A means of nondimensionalizing P_e on the basis of a finite cylindrical shell was done by Yamaki & Otomo (1973) and Batdorf (1947) who nondimensionalized P_e by the following,

$$K_P = \frac{\pi^2 E h^3}{6(1-\sigma^2) D_0 L_0^2}, \tag{3.1}$$

where K_P is the finite bending stiffness parameter, E is the Young's modulus, and σ is Poisson's ratio. The values for the tubes tested are shown in table 3.1. Alternatively, Kececioglu *et al.* (1981) in their work considered extremely long tubes and on the basis of extremely long tubes, a similar parameter for non-dimensionalizing P_e can be developed, called here the infinite bending stiffness parameter $K_{P,\infty}$, and is defined as

$$K_{P,\infty} = \frac{2\pi^2 E h^3}{3(1-\sigma^2) D_0^3} \tag{3.2}$$

such that the length of the tube, L_0, in K_P has been replaced by the diameter of the tube, D_0 (Singer *et al.* 1998, pg. 58). The values of this parameter are also found in table 3.1. In light of the bending stiffness parameters for both finite and infinite tubes, we can consider the order of magnitudes between the different tubes. The finite bending stiffness parameter, K_P, in general is $\mathcal{O}(10^{-1})$ with the exception of tube S-4. For the infinite bending stiffness parameter, $K_{P,\infty}$, we see that there is an order of magnitude between each of the different tube diameters, as one might expect given the D_0^{-3} dependence.

The collapsible tubes were mounted such that the axial tension was minimal. To avoid axial buckling, a small amount of strain (≈1%–3%) was imparted on the collapsible tube during installation. This was desirable, because thin-walled tubes buckle easily under axial compression. The work of Sakurai *et al.* (1996) found that axial tension significantly affected

the oscillation frequency, where over a range of tube strains from 0%–100% the frequency of oscillation was approximately reduced by a factor of 2. However, it is expected that the effect of the small amount of strain applied presently is negligible. The strain was imparted by carefully mounting the tube such that the slack tube's length of the collapsible section was slightly less than the required, thus when the tube was installed a small amount of strain was imparted to the tube. This was verified by markings on the tube and photographs that were taken before and after installation of the tube to the PVG device.

The experiments were conducted in a water tank with a cross-sectional area of 110 cm in width and up to 60 cm in height, with a test-section length of approximately 40 m. The nozzles were mounted rigidly and while the test-section was quite long, only a limited portion was actually utilized in these experiments. A schematic of the experiments is shown in Figure 3.2.

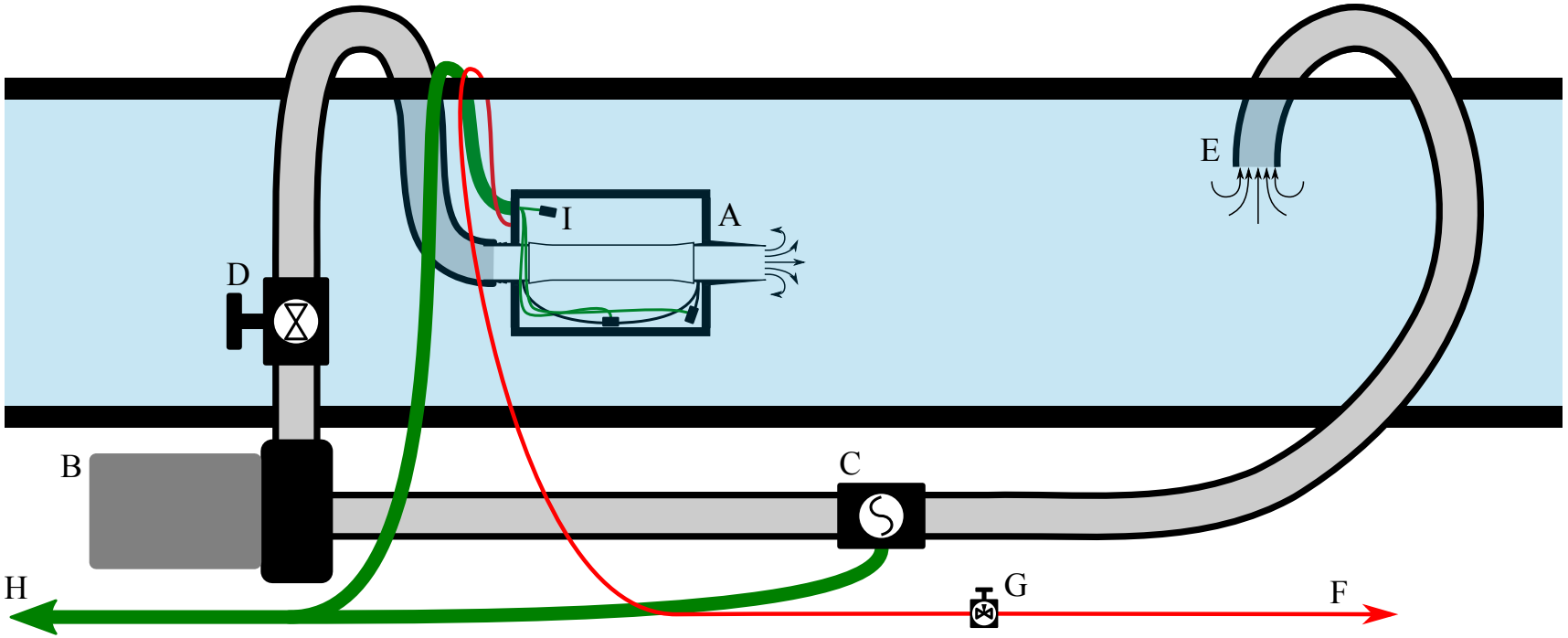

Figure 3.2: Schematic drawing of facility for the PVG parameter study experiments. Letters indicate the item as follows: A, passive vortex generator (PVG); B, pump for delivering fluid to PVG; C, upstream paddle-wheel flowmeter; D, gate valve for modulating flow rate through PVG; E, water inlet to pump, located away from the experiments; F, tubing to connect to high-pressure air source; G, needle valve for controlling air delivery to PVG; H, connection to computer DAQ system from pressure transducers and flowmeter; I, pressure transducers inside PVG chamber.

It was expected that the dynamic pressure within the nozzle has a significant influence on the self-excited oscillations of the PVG by affecting the forces on the collapsible tube. As the dynamic pressure is defined as $\rho U_j^2/2$, flow speeds, U_j, in the 0.2–0.8 m s^{-1} range were selected for comparison among the different nozzles. This yielded dynamic pressures in the range of $\approx$ 20–320 Pa and Reynolds numbers in the range of $\approx$ 3000–45,000 across the range of nozzle diameters. Even for the lowest Reynolds number cases, because the flow was not conditioned before entering the tube, all of the flows were fully turbulent. Due to the wide range of flow speeds and diameters, the volumetric flow rate necessary for these experiments ranged from 0.05 to 2.0 L s^{-1}. To accommodate this requirement, two pumps were used with separate paddle-wheel flowmeters to measure the time-averaged flow rate.

The smaller of the two pumps was an electric motor (Leeson C42D17FK4A) with an attached impeller and electric motor speed controller (Leeson 174307.00) for controlling the flow rate and coupled with a flowmeter (Omega FPR303). The smaller pump had a range of 0.01–0.63 L s^{-1}. The large pump (Dolphin DP62502) was modulated using a downstream gate valve and flow was measured with a flowmeter (Omega FP7001A/FP7015). This system had a range of 0.45–4.1 L s^{-1}. For each pumping system, the flowmeter was placed several tube diameters away from the pump to ensure accurate readings of the flow rate, as illustrated in Figure 3.2.

The transmural pressure, defined as $P_t \equiv P_e - P_2$, is the difference between the chamber pressure and the pressure inside the downstream end of the collapsible tube. It should be noted that this is a definition different from what is normally given in the physiology literature for the transmural pressure in order to obtain only positive values. The driving pressure, defined as $P_d \equiv P_1 - P_2$, is the pressure difference between the upstream and downstream ends of the collapsible tube. The transmural and driving pressures were measured

using differential pressure transducers (Omega PX26-005DV). The pressure transducers were calibrated using a water manometer. The chamber pressure was measured using an absolute pressure transducer (Omega PX72-030AV) and the manufacturer-supplied calibration coefficient was used. Due to variations in the hydrostatic pressure caused by changes in the water depth in the tank and natural variation in the barometric pressure, the values of the chamber pressure may have a mean offset from one measurement set to the next. A manual air pump connected to a needle valve and analog gauges allowed for control over the air pressure in the PVG chamber, as shown in Figure 3.2

Each PVG incorporated a DE-9 serial extension cable that passed through the chamber sidewall. This cable was used to supply power to the pressure sensors within the PVG and to connect the outputs of the transducers to the data acquisition system (cf. Figure 3.2). The cable extended out of the PVG and connected to an amplifier circuit and power supply. The data acquisition (DAQ) system consisted of a computer running Windows XP and a USB-based DAQ device (NI USB-6221). The MATLAB software program (Mathworks) was used for accessing the DAQ device and processing and storing the results. The DAQ system recorded signals from four channels: one for each pressure transducer and the flowmeter signal.

3.3 Methods

Measurements of the transmural, driving, and chamber pressures and flow rate were taken at approximate increments of 500 kPa of the transmural pressure at a range of flow speeds, U_j. First, the average flow rate was set to within 0.005 L s^{-1} of the desired value and the pressure in the chamber was adjusted until a mean transmural pressure of 0 kPa was obtained. This constituted the first data point for each flow rate, and further data points

were collected by increasing the mean transmural pressure in approximate increments of 500 kPa by use of a manual air pump with a needle valve. For each desired condition, adjustments to the flow rate and transmural pressure were required. Once the desired conditions were achieved, measurements of the transmural, driving, and chamber pressures and flow rate were recorded at 10 kHz for 10 seconds. The sampling rate was quite high, however it ensured that we captured any higher order harmonics and later software-based low-pass filtering to remove noise essentially downsampled the data. If the mean transmural pressure for the recording was more than 100 kPa away from the desired value, then the point was discarded and the setup was adjusted before rerecording that data point; this occurred periodically due to issues with maintaining the seal on the chamber or tube. Some data points were considered unobtainable and were skipped. An unobtainable point typically occurred when the system transitioned from steady to pulsed flow and vice versa. If significant transients were obtained during recording, then the system was allowed to return to steady state, adjusted if necessary, then rerecorded. Because of the manual nature of setting the flow settings (both the pressure and flow rate) and the rather coarse control, especially over the flow rate, the desired conditions were only approximately obtained (e.g., some points are only 400 kPa apart, despite the goal of a 500 kPa interval). However, because the true value was recorded, this is not a significant issue.

This procedure produced a collection of data at different pressure conditions for each nozzle, at a given flow speed. The upper limit of P_e was obtained when either the pressure became so high as to suppress any self-excited oscillations (a possibility for the largest nozzle at low flow rates) or the transmural pressure transducer saturated its DAQ channel. Once the limiting P_e was reached, the procedure was repeated, this time by decreasing the transmural pressure in approximate increments of 500 kPa. This allowed us to obtain

information on the hysteresis of the oscillation. The entire procedure was repeated for four different flow rate settings for each of the nozzles tested.

Using MATLAB's built-in fast-Fourier transform (FFT) algorithm, the fundamental frequency of the flowmeter signal was found. This frequency was used in conjunction with the flowmeter manufacturer's supplied calibration coefficient to determine the average flow speed through the device.

The tube oscillation frequency was determined from an FFT of the transmural pressure. Since the goal of the present work was to investigate the oscillatory nature of the PVG, the waveform shapes were also visually evaluated. Within the portion of the data set which exhibited a discernible oscillation, the transmural pressure waveforms varied considerably in amplitude and shape, with most waveforms having only a strong fundamental frequency and others with strong subharmonics like the "2-out-of-3" beats mode described by Bertram (1986). To consider the effect that different oscillation modes may have on the results, isolation of test conditions that yielded similar waveforms (and were thus expected to have similar self-excited oscillation mechanisms) was conducted. This was accomplished via applying thresholds to the transmural pressure frequency spectra. However, comparison of the complete data set versus the thresholded data set showed that although the thresholding did remove a noticeable number of experimental conditions (19% across all nozzles), the overall results did not seem greatly impacted by the omissions. Thus the complete data set is presented despite the possibility of variations in the oscillation mode.

3.4 Results

The results have been divided into two subsections. The first considers the effect of changing tube diameter on the self-excited oscillations through a set of experiments where the tube

shape, L_0/D_0, is kept constant and another set of experiments where the tube length, L_0, is kept constant. The second subsection considers the effect of changing the tube length for constant tube diameter, D_0.

3.4.1 Effect of Tube Diameter

Figures 3.3 and 3.4 compare tubes of the same shape at different tube diameters (S-4, M-4, and L-4). Figure 3.5 and 3.6 compares tubes of the same length at different tube diameters (S-12, M-6, and L-4). Figures 3.3 and 3.5 show plots of the tube oscillation frequency versus the nondimensionalized pressure coefficient based on the mean driving pressure, where

$$C_P = \frac{\overline{P_d}}{\frac{1}{2}\rho U_j^2}, \tag{3.3}$$

and the overline indicates time averaging. Several candidates for the independent variable were considered, but a pressure coefficient using the driving pressure was found to result in the best collapse of the data. See appendix G for examples of plots using other variables. Figures 3.4 and 3.6 show plots of the tube oscillation frequency versus the diameter of the tube. For figures 3.3–3.6, there is a plot for each flow speed, U_j, ranging from 0.2 to 0.8 m s^{-1}.

To further investigate the diameter-independence of the PVG, results that were in close proximity within the frequency/flow-speed/pressure-coefficient parameter space and were present in different nozzles were chosen. These sets of points are shown encircled in figure 3.3. The representative waveforms and frequency spectra for the same encircled conditions are shown in figure 3.7. The waveforms from different nozzles have been phase-matched based on the trough of the P_2 waveform at $t = 0$. However, no other time manipulation

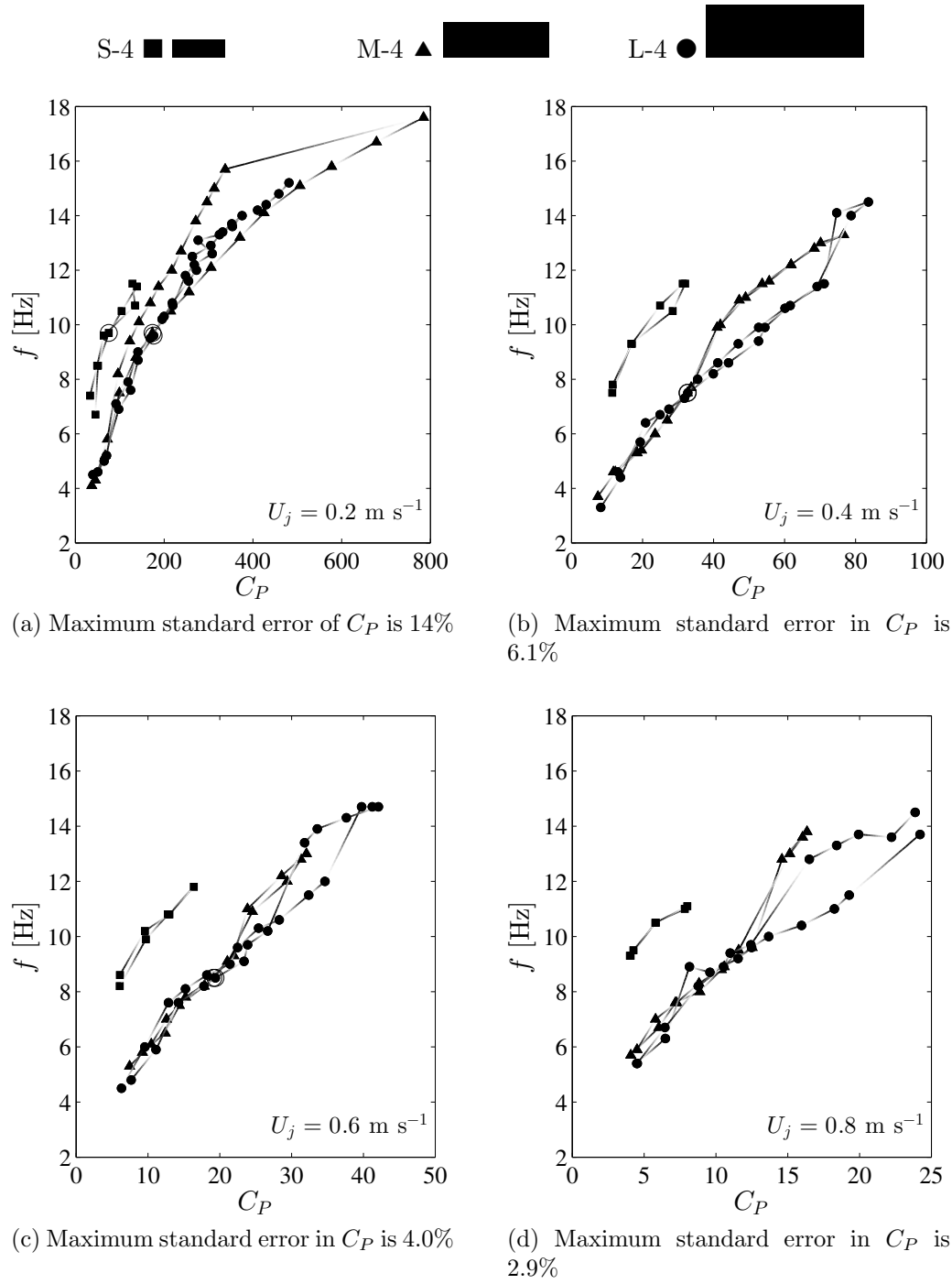

(a) Maximum standard error of C_P is 14%

(b) Maximum standard error in C_P is 6.1%

(c) Maximum standard error in C_P is 4.0%

(d) Maximum standard error in C_P is 2.9%

Figure 3.3: Plots of the oscillation frequency versus the pressure coefficient at four different flow speeds. The marker symbols denote the nozzle being plotted: ■ for S-4, ▲ for M-4, and ● for L-4. The shape, to scale, of the tube is denoted next to its marker above the plots for visual reference. The encircled points are the points of comparison in figure 3.7. Data points are taken only at the marker location and the line connecting the markers indicates direction of movement in parameter space during the experimental run as moving along increasing level of darkness (i.e., direction is from white to black). A connecting line means that the two points were immediately adjacent during the experimental run. Points not connected by lines mean that there are other point(s) in between that are not displayed due to a lack of a dominant frequency. The error in the frequency is 0.1 Hz.

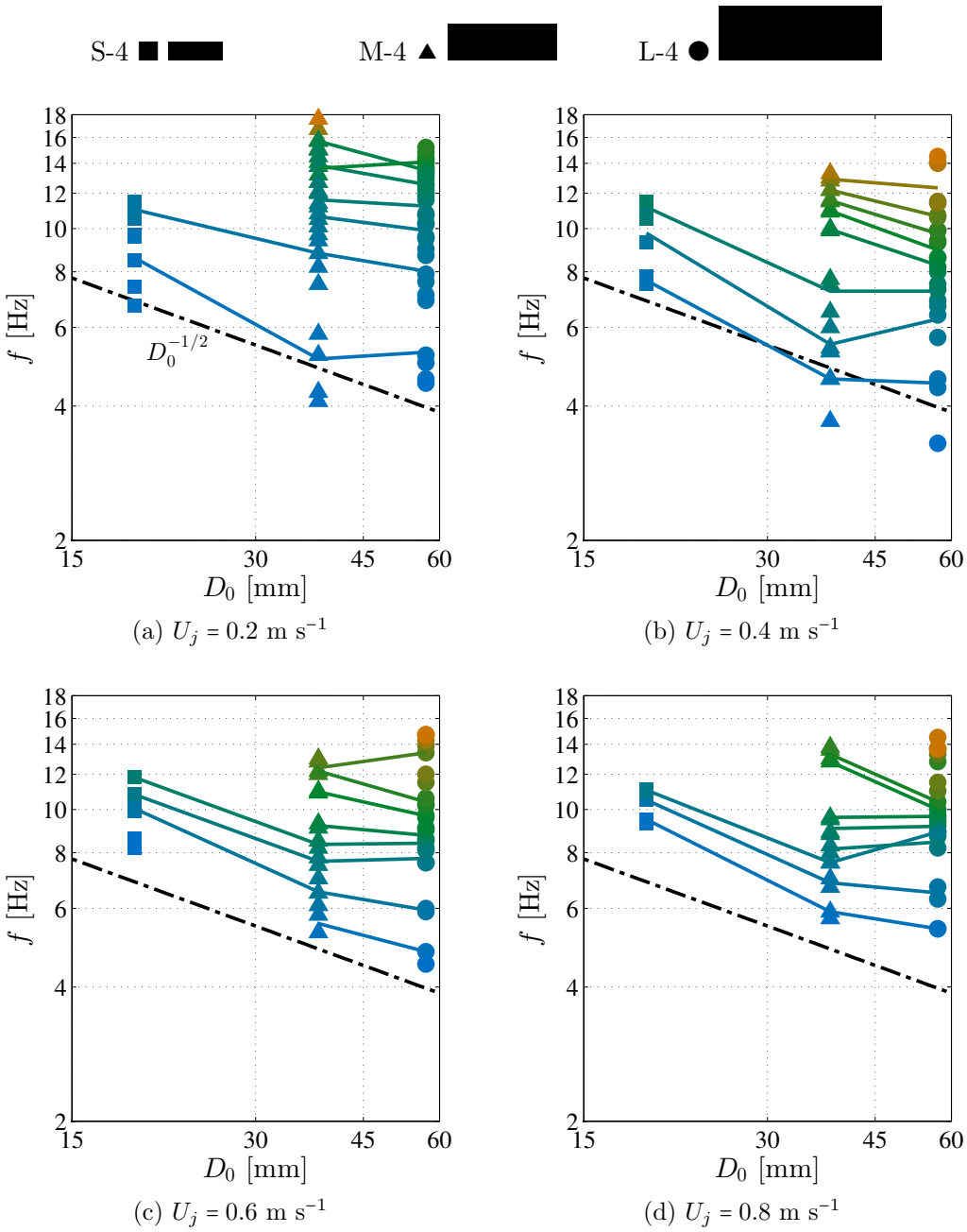

(a) $U_j = 0.2$ m s^{-1} (b) $U_j = 0.4$ m s^{-1}

(c) $U_j = 0.6$ m s^{-1} (d) $U_j = 0.8$ m s^{-1}

Figure 3.4: Plots of the oscillation frequency versus the tube diameter at four different flow speeds. The marker symbols denote the nozzle being plotted: ■ for S-4, ▲ for M-4, and ● for L-4. The shape, to scale, of the tube is denoted next to its marker above the plots for visual reference. The color indicates the value of C_P. Lines connect the average f within a range of C_P and are intended to help demonstrate the effect of D_0 on f for constant C_P and L_0/D_0. The black dashed-dotted line has slope $-1/2$ for reference. The error in the frequency is 0.1 Hz.

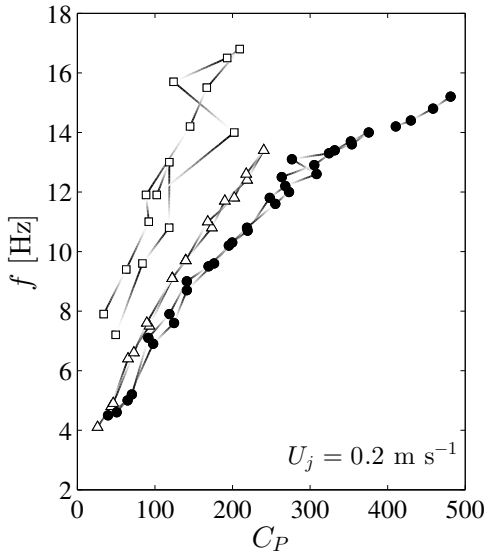

(a) Maximum standard error of C_P is 14%

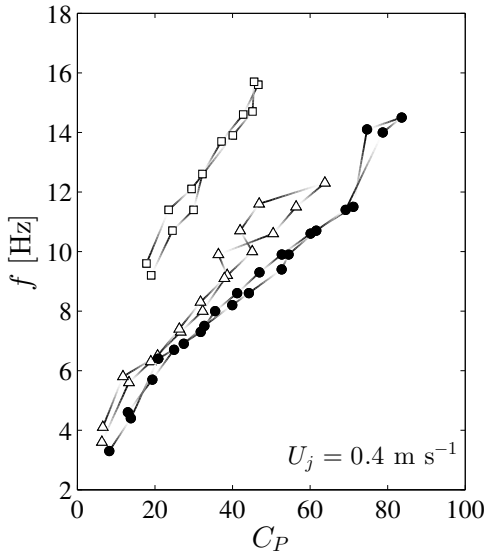

(b) Maximum standard error in C_P is 5.9%

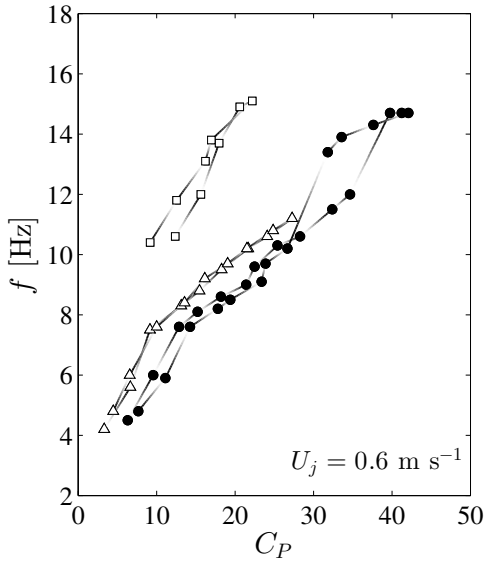

(c) Maximum standard error in C_P is 3.9%

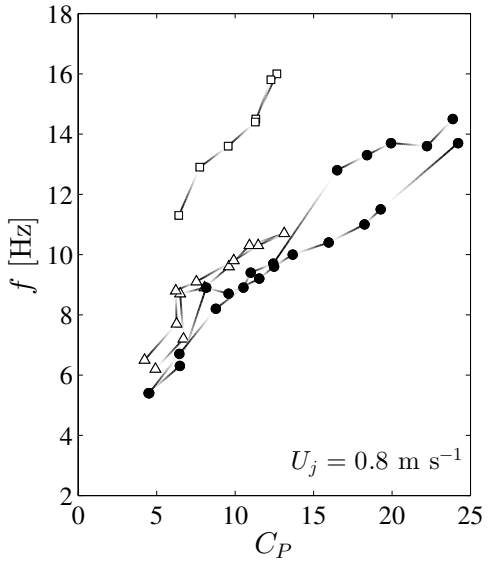

(d) Maximum standard error in C_P is 3.0%

Figure 3.5: Plots of the oscillation frequency versus the pressure coefficient at four different flow speeds. The marker symbols denote the nozzle used: □ for S-12, △ for M-6, and ● for L-4. The shape, to scale, of the tube is denoted next to its marker above the plots for visual reference. The encircled points are the points of comparison in figure 3.7. Data points are taken only at the marker location and the line connecting the markers indicates direction of movement in parameter space during the experimental run as moving along increasing level of darkness (i.e., direction is from white to black). A connecting line means that the two points were immediately adjacent during the experimental run. Points not connected by lines mean that there are other point(s) in between that are not displayed due to a lack of a dominant frequency. The error in the frequency is 0.1 Hz.

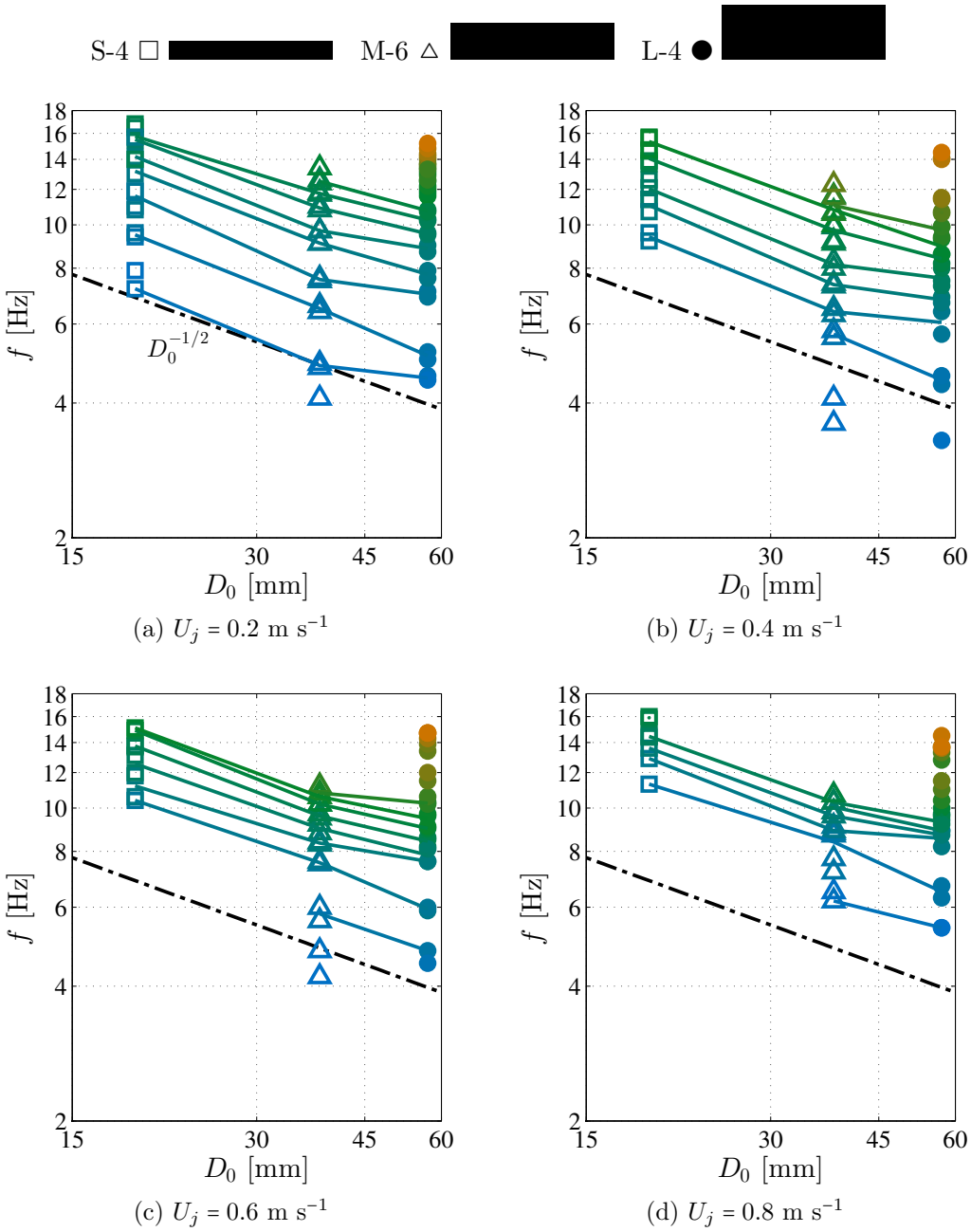

Figure 3.6: Plots of the oscillation frequency versus the tube diameter at four different flow speeds. The marker symbols denote the nozzle being plotted: □ for S-12, △ for M-6, and ● for L-4. The shape, to scale, of the tube is denoted next to its marker above the plots for visual reference. The color indicates the value of C_P. Lines connect the average f within a range of C_P and are intended to help demonstrate the effect of D_0 on f for constant C_P and L_0. The black dashed-dotted line has slope $-1/2$ for reference. The error in the frequency is 0.1 Hz.

has been applied. Hence, the waveforms diverge over time due to their slightly different frequencies. Because the chamber pressure is measured using an absolute pressure gauge, the magnitude of this pressure can vary from day to day due to the barometric pressure. For simplicity, the mean has been subtracted from the traces of P_e. The values of P_1 and P_2 were then calculated using $P_2 = P_e - P_t$ and $P_1 = P_d + P_2$, respectively, using the mean-subtracted P_e.

3.4.2 Effect of Tube Length

Figures 3.8 and 3.10 show plots of the tube oscillation frequency versus the nondimensionalized pressure coefficient based on the mean driving pressure, C_P for tubes of the smallest diameter (S-4 and S-12) and medium diameter (M-4 and M-6), respectively, at different lengths. Figures 3.9 and 3.11 show plots of the tube oscillation frequency versus tube length for the smallest and medium diameter, respectively. Figures 3.8–3.11 each contain plots for each flow velocity, ranging from 0.2 to 0.8 m s^{-1}.

To further investigate the length-independence of the PVG, results that were in close proximity within the frequency/flow-speed/pressure-coefficient parameter space and were present in different devices were chosen. These sets of points are shown encircled in figures 3.8 and 3.10. The representative waveforms and frequency spectra for the encircled conditions are shown in figure 3.12, as done in section 3.4.1.

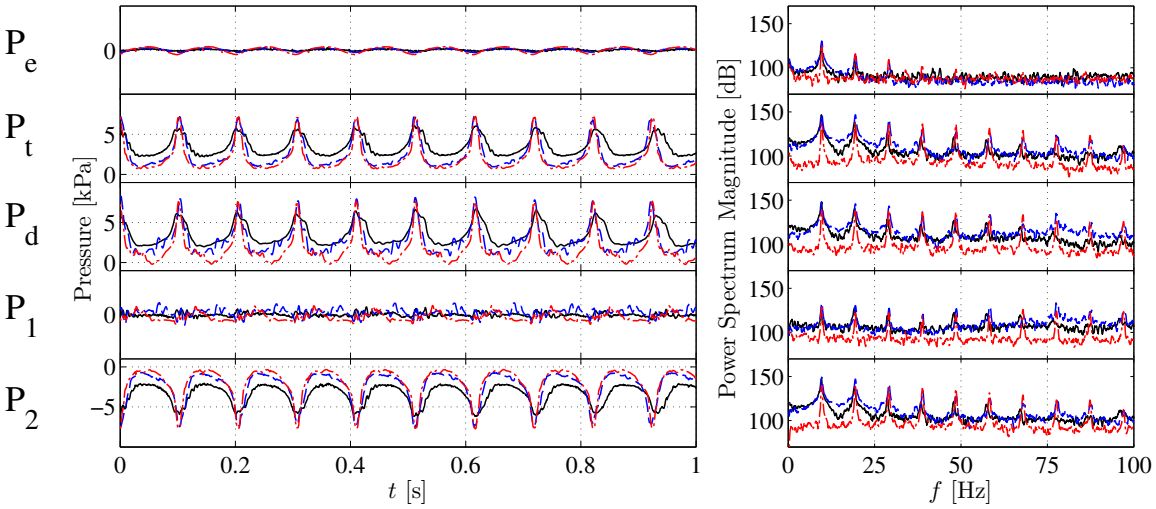

(a) Collection of points from the region in the parameter space of $U_j = 0.2$ m s^{-1}, $f = 9.5$, $C_P = 100$. The chosen points are encircled in figure 3.3(a). The solid black line is for the L-4 nozzle, the dashed blue line for the M-4 nozzle, and the dot-dashed red line for the S-4 nozzle.

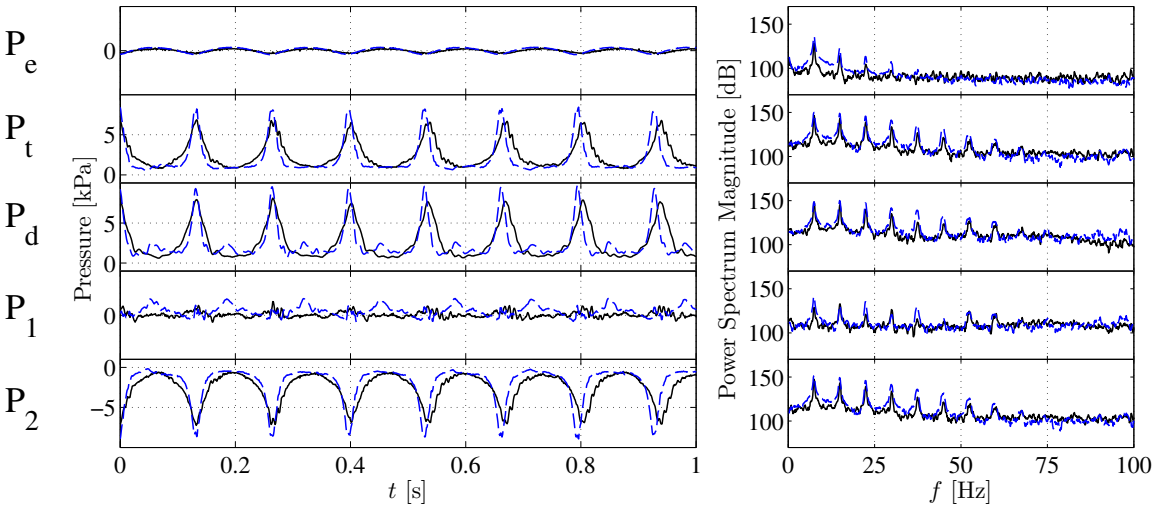

(b) Pair of points from the region in the parameter space of $U_j = 0.4$ m s^{-1}, $f = 7.5$, $C_P = 32$. The chosen points are encircled in figure 3.3(b). The solid black line is for the L-4 nozzle and the dashed blue line for the M-4 nozzle.

Figure 3.7: Full caption available on page 97.

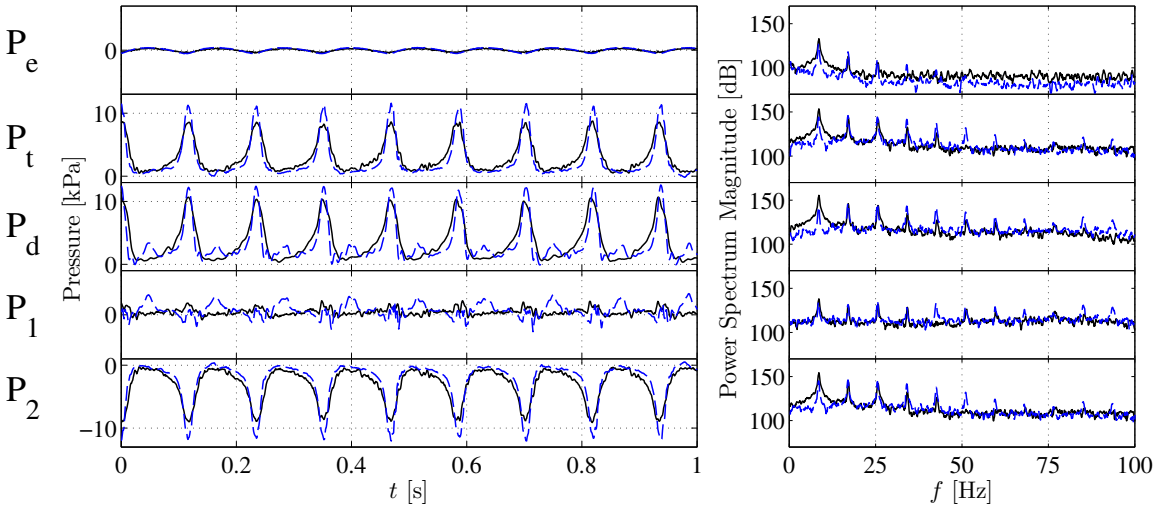

(c) Pair of points from the region in the parameter space of $U_j = 0.6$ m s^{-1}, $f = 8.5$, $C_P = 19$. The chosen points are encircled in figure 3.3(c). The solid black line is for the L-4 nozzle and the dashed blue line for the M-4 nozzle.

Figure 3.7: Waveform plots of the measured chamber pressure (mean subtracted), P_e, transmural pressure, P_t, driving pressure, P_d, and calculated upstream, P_1, and downstream, P_2, nozzle pressures. To the right of the waveform plots are the power spectra for the pressures with the mean component subtracted. Within each subfigure, the ordinate scales have been matched among all of the waveform and frequency plots, respectively.

3.5 Discussion

3.5.1 Diameter Study Discussion

The results plotted in figure 3.3 show a nearly linear dependence between the oscillation frequency and the pressure coefficient. Furthermore, the data for the medium and largest diameter devices, M-4 and L-4, collapse well, particularly for lower values of the pressure coefficient. However, the M-4 nozzle appears to depart from the L-4 nozzle after a critical pressure coefficient, and undergoes a swift increase in oscillation frequency thereafter. The smallest device, S-4, appears to yield a frequency of oscillation that is noticeably higher than that of the M-4 and L-4 nozzles. Additionally, for the L-4 nozzle, it is apparent from figures 3.3(c) and (d) that there is some hysteresis in the device as the higher pressure coefficient values yield different frequencies depending on whether one is on the ascending

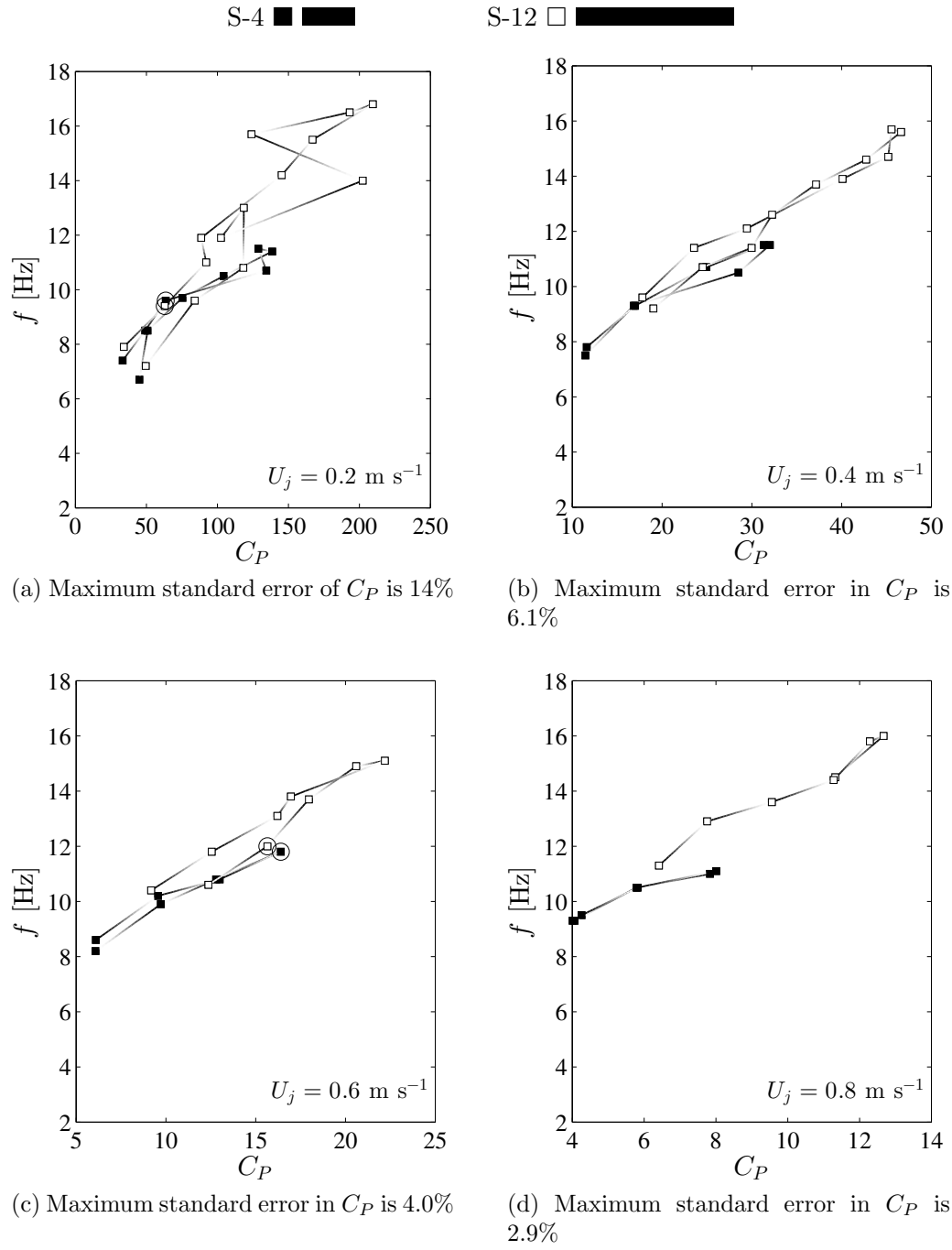

(a) Maximum standard error of C_P is 14%

(b) Maximum standard error in C_P is 6.1%

(c) Maximum standard error in C_P is 4.0%

(d) Maximum standard error in C_P is 2.9%

Figure 3.8: Plots of the oscillation frequency versus the pressure coefficient at four different flow speeds. The marker symbols denote the nozzle being plotted: ■ for S-4 and □ for S-12. The shape, to scale, of the tube is denoted next to its marker above the plots for visual reference. The encircled points are the points of comparison in figure 3.12. Data points are taken only at the marker location and the line connecting the markers indicates direction of movement in parameter space during the experimental run as moving along increasing level of darkness (i.e., direction is from white to black). A connecting line means that the two points were immediately adjacent during the experimental run. Points not connected by lines mean that there are other point(s) in between that are not displayed due to a lack of a dominant frequency. The error in the frequency is 0.1 Hz.

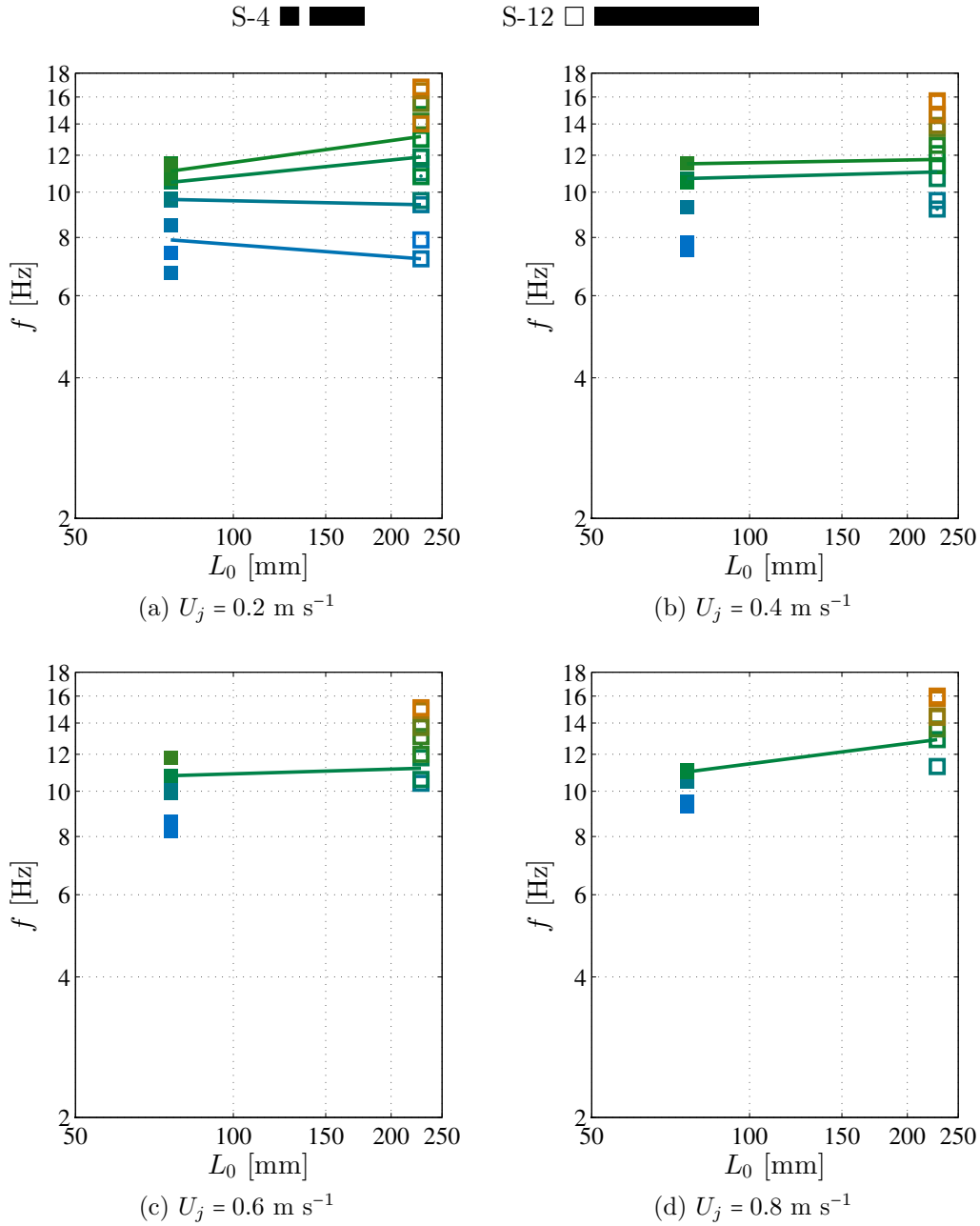

(a) $U_j = 0.2$ m s^{-1} (b) $U_j = 0.4$ m s^{-1}

(c) $U_j = 0.6$ m s^{-1} (d) $U_j = 0.8$ m s^{-1}

Figure 3.9: Plots of the oscillation frequency versus the tube length at four different flow speeds. The marker symbols denote the nozzle being plotted: ■ for S-4 and □ for S-12. The shape, to scale, of the tube is denoted next to its marker above the plots for visual reference. The color indicates the value of C_P. Lines connect the average f within a range of C_P and are intended to help demonstrate the effect of L_0 on f for constant C_P and D_0. The error in the frequency is 0.1 Hz.

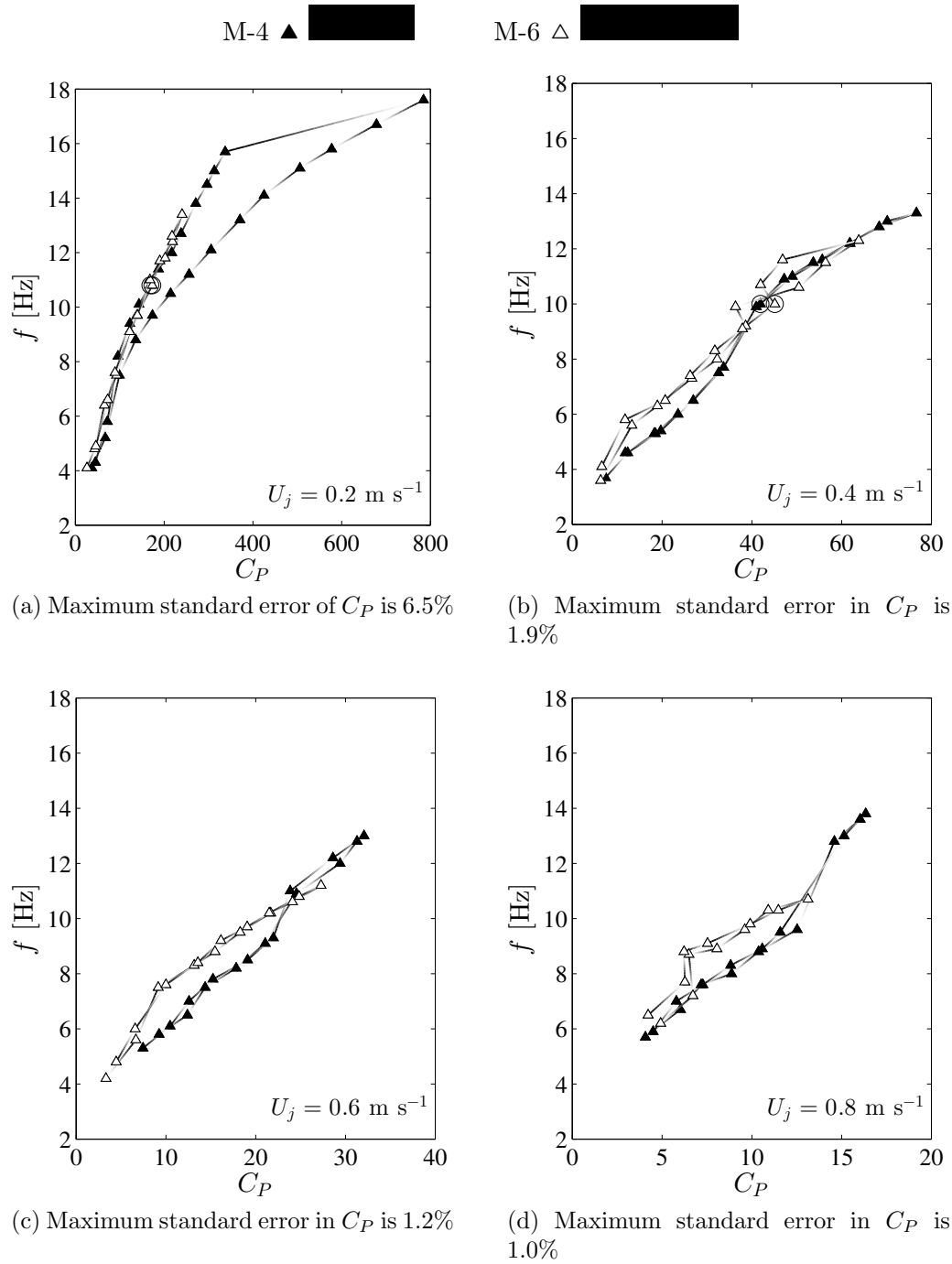

(a) Maximum standard error of C_P is 6.5%

(b) Maximum standard error in C_P is 1.9%

(c) Maximum standard error in C_P is 1.2%

(d) Maximum standard error in C_P is 1.0%

Figure 3.10: Plots of the oscillation frequency versus the pressure coefficient at four different flow speeds. The marker symbols denote the nozzle used: ▲ for M-4 and △ for M-6. The shape, to scale, of the tube is denoted next to its marker above the plots for visual reference. The encircled points are the points of comparison in figure 3.12. Data points are taken only at the marker location and the line connecting the markers indicates direction of movement in parameter space during the experimental run as moving along increasing level of darkness (i.e., direction is from white to black). A connecting line means that the two points were immediately adjacent during the experimental run. Points not connected by lines mean that there are other point(s) in between that are not displayed due to a lack of a dominant frequency. The error in the frequency is 0.1 Hz.

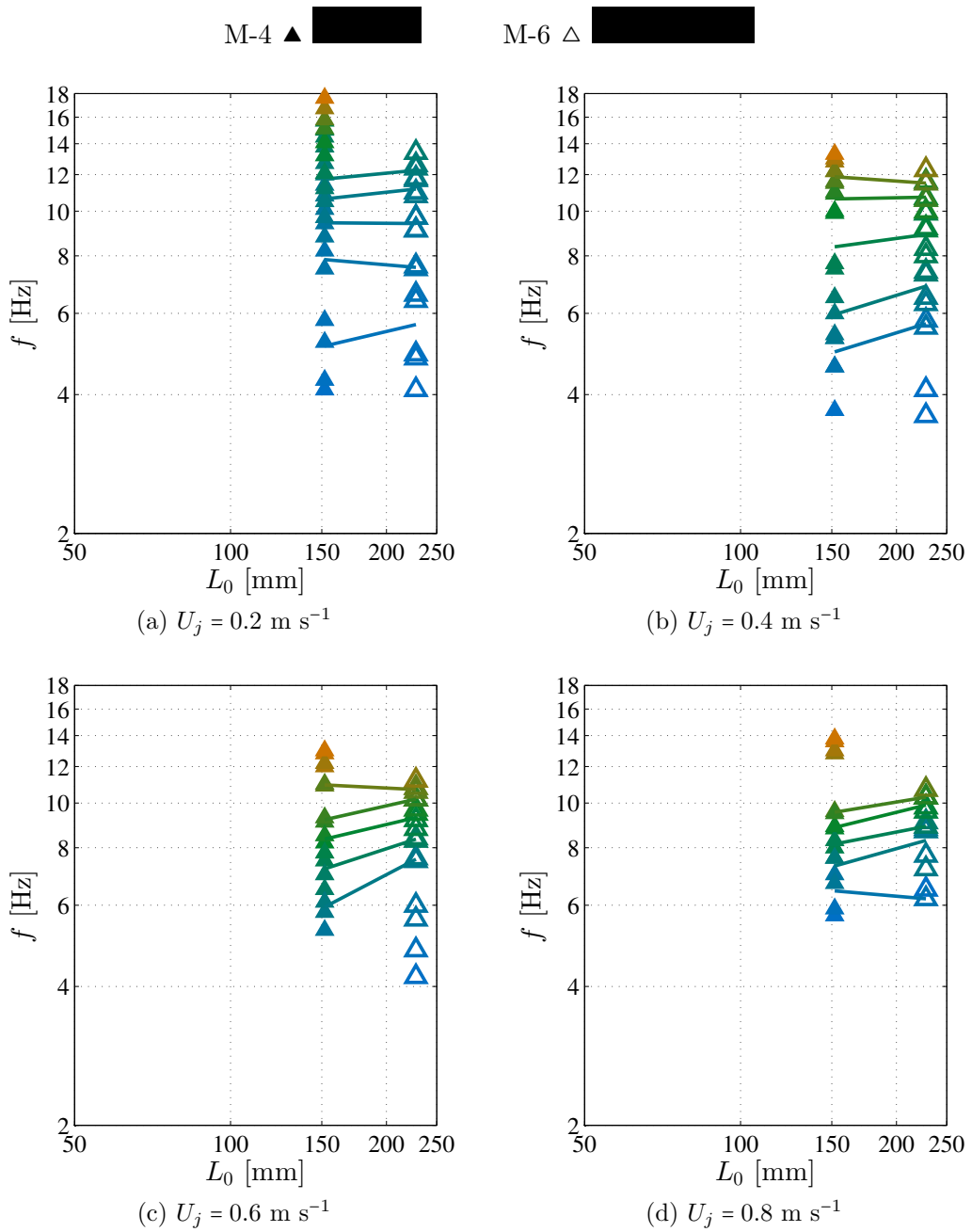

(a) $U_j = 0.2$ m s^{-1} (b) $U_j = 0.4$ m s^{-1}

(c) $U_j = 0.6$ m s^{-1} (d) $U_j = 0.8$ m s^{-1}

Figure 3.11: Plots of the oscillation frequency versus the tube length at four different flow speeds. The marker symbols denote the nozzle being plotted: ▲ for M-4 and △ for M-6. The shape, to scale, of the tube is denoted next to its marker above the plots for visual reference. The color indicates the value of C_P. Lines connect the average f within a range of C_P and are intended to help demonstrate the effect of L_0 on f for constant C_P and D_0. The error in the frequency is 0.1 Hz.

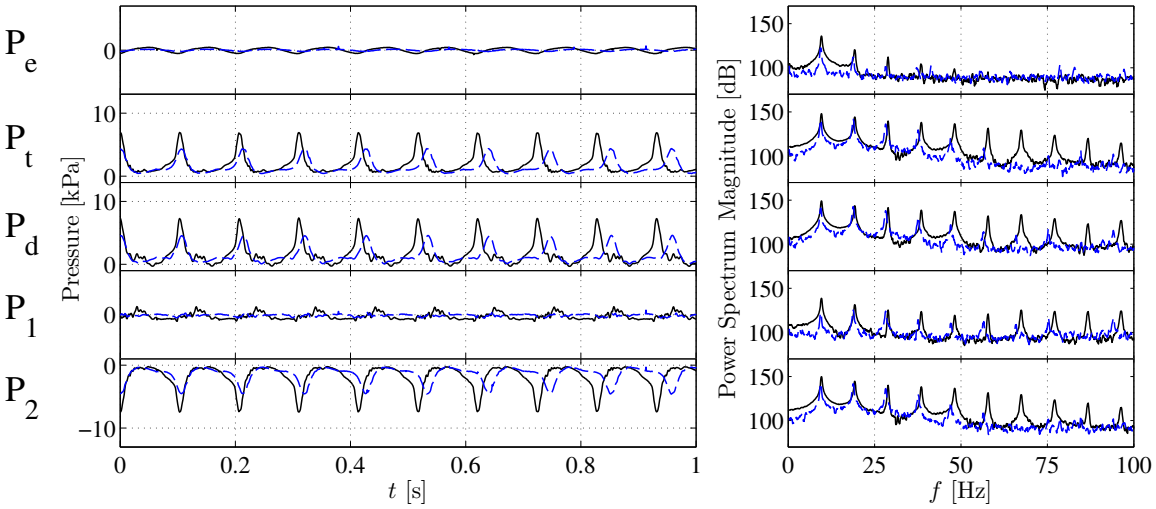

(a) Pair of points from the region in the parameter space of $U_j = 0.2$ m s^{-1}, $f = 9.5$, $C_P = 63$. The chosen points are encircled in figure 3.8(a). The solid black line is for the S-4 nozzle and the dashed blue line for the S-12 nozzle.

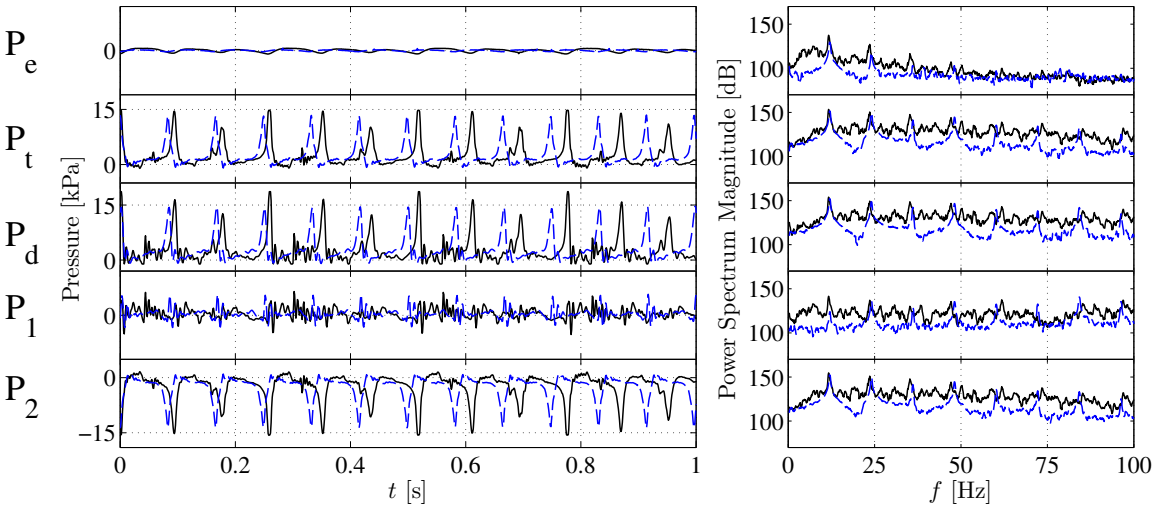

(b) Pair of points from the region in the parameter space of $U_j = 0.6$ m s^{-1}, $f = 12$, $C_P = 16$. The chosen points are encircled in figure 3.8(c). The solid black line is for the S-4 nozzle and the dashed blue line for the S-12 nozzle.

Figure 3.12: Full caption found on page 103

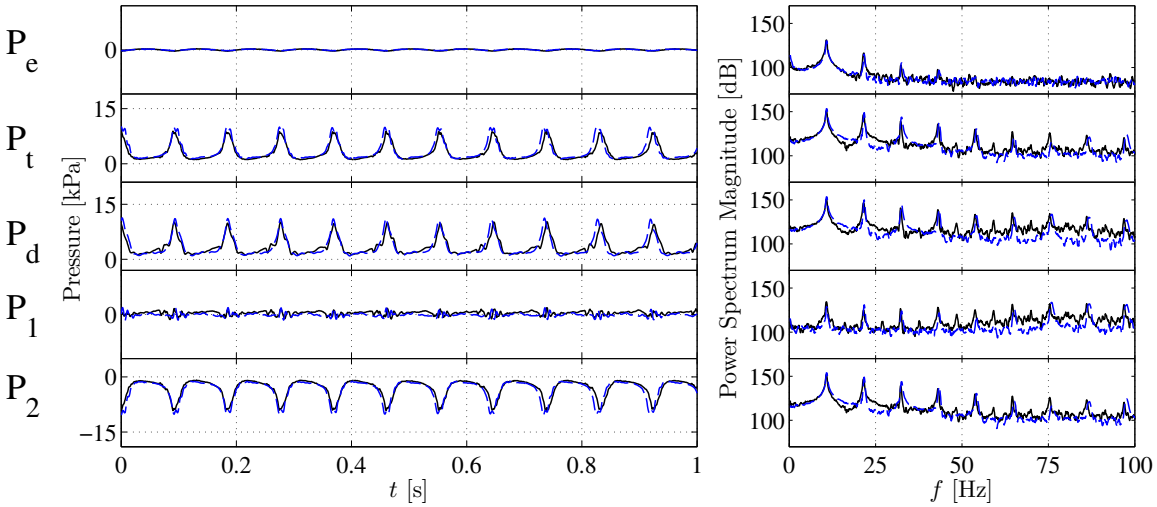

(c) Pair of points from the region in the parameter space of $U_j = 0.2$ m s^{-1}, $f = 11$, $C_P = 170$. The chosen points are encircled in figure 3.10(a). The solid black line is for the M-4 nozzle and the dashed blue line for the M-6 nozzle.

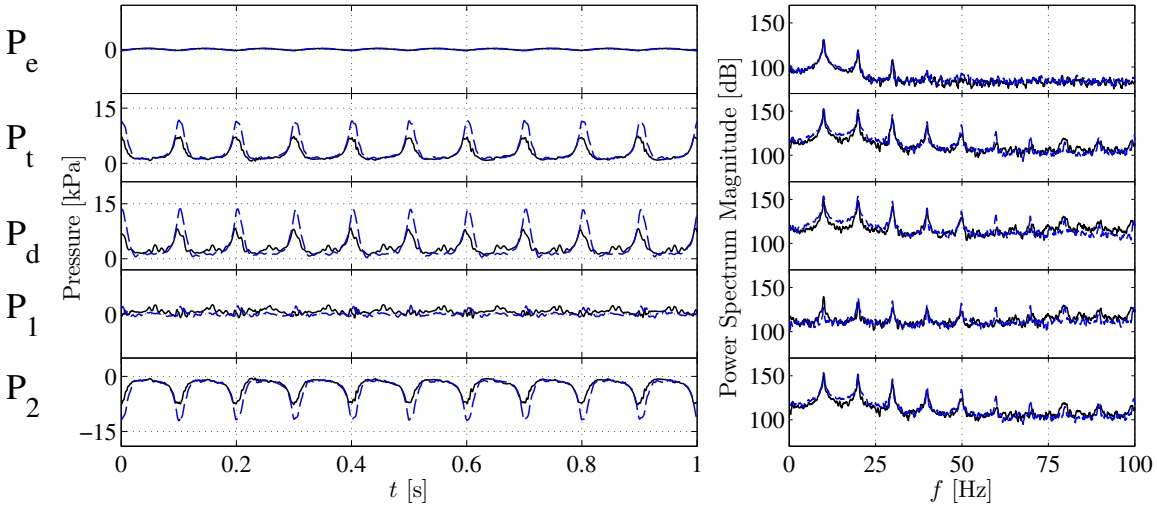

(d) Pair of points from the region in the parameter space of $U_j = 0.4$ m s^{-1}, $f = 10$, $C_P = 43$. The chosen points are encircled in figure 3.10(b). The solid black line is for the M-4 nozzle and the dashed blue line for the M-6 nozzle.

Figure 3.12: Waveform plots of the measured chamber pressure (mean subtracted), P_e, transmural pressure, P_t, driving pressure, P_d, and calculated upstream, P_1, and downstream, P_2, nozzle pressures. To the right of the waveform plots are the power spectra for the pressures with the mean component subtracted. Within each subfigure, the ordinate scales have been matched among all of the waveform and frequency plots, respectively.

or descending branch of the pressure coefficient.

The plots of the oscillation frequency versus diameter for the tubes with constant L_0/D_0 (figure 3.4) seem to indicate that the oscillation frequency is, at best, a weak function of the tube diameter for constant shape tubes. In general it appears that the frequency decreases with increasing tube size, however this is primarily due to the data points from the S-4 nozzle. If these data points were omitted, then there would exist no clear trend between the oscillation frequency and the diameter of the device. However, with their inclusion, it appears that there might be an overall trend of $f \sim D_0^{-1/2}$.

The individual data-point analyses, given in figure 3.7, show some interesting attributes about the operation of the different nozzles with constant L_0/D_0. Firstly, amongst all of the points considered, the oscillation in the external pressure, P_e, is discernible, as expected from equation (2.2). A comparison of the oscillation magnitudes of P_1 and P_2 shows that, in general, the oscillation amplitude of P_1 is significantly lower than that of P_2. This shows that the fluid velocity at the nozzle inlet is relatively steady and does not oscillate as significantly as the velocity in the downstream end of the PVG. The plot of $P_2(t)$ for each of the nozzles shows characteristically the same waveform for the crests, however the depths of the troughs differ. Across all of the sets of points, the depth of the trough (and thus the peak-to-peak magnitude of the overall waveform) decreases with increasing nozzle diameter size.

Figure 3.5 explores the oscillation frequency versus the pressure coefficient for the case of constant length tubes. Again, one finds a nearly linear trend between the oscillation frequency and the pressure coefficient. Here we find that the collapse of the data is not as strong as it was in figure 3.3. The smallest nozzle, S-12, continues to have higher oscillation frequencies than the larger nozzles, as was seen in the constant L_0/D_0 cases; the medium

Table 3.2: Summary of results for scaling the oscillation frequency, f, based on the tube diameter, D_0

Study	x (where $f \sim D_0^x$)
Jensen & Heil (2003)	1/2
Heil & Waters (2008)	–5/2
Cancelli & Pedley (1985)	–5/2
Current Study	–1/2

nozzle, M-6, tends to have oscillation frequencies that are between those of the S-12 and L-4 nozzles.

Consideration of the results from figure 3.6 shows that the frequency is now a noticeable function of the diameter, which explains the greater spread between the different nozzles of figure 3.5. Figure 3.6 indicates that for constant length tubes, that the frequency of oscillation decreases as the diameter of the tube increases. Based on the reference line indicated in figure 3.6, the relationship goes as $f \sim D_0^{-1/2}$, which is far more pronounced for this data set than in figure 3.4.

This result is in contrast to the previous scaling laws that were obtained from the literature (cf. section 1.6). For a review of the scaling of f to D_0, see table 3.2. One can see that the majority of the studies were correct in predicting a negative dependence between the oscillation frequency and the tube diameter. However, the magnitude of the scaling from the current experiments appears to be less than that predicted by the theoretical arguments.

3.5.2 Length Study Discussion

Based on the data collected for the diameter study, it is also possible to do an analysis of the effect of tube length on the oscillation frequency. The results for the smallest diameter are shown in figure 3.8 and 3.9. The results from the S-4 and S-12 tubes shows the influence

that tripling the tube length can have on the oscillation frequency. The frequency for the S-12 tube, in general, is higher than that of the S-4 tube. However, based on the results plotted in figure 3.9, there is not a very strong relationship between the oscillation frequency and the tube length. Thus suggesting that the tube length does not have a significant effect on the oscillation frequency for the conditions tested. It should be noted that the scatter in figure 3.8(a) for the S-12 case is primarily due to experimental difficulties in manually setting the flow rate and the pressure within the chamber.

Another look at the effect of changing tube length comes from a comparison of the M-4 and M-6 data. Figures 3.10 and 3.11 show the results from the M-sized tubes for two different tube lengths. As the difference in tube length is not nearly as large as for the length comparison between amongst the S tubes (factor of 3/2 versus 3), the data collapse in figure 3.10, especially for the two lowest velocities, is much more pronounced. In figure 3.10(a), for example, the overlap is remarkable. The overlap is not quite as pronounced in the higher velocities, but there is no clear trend between the two tubes.

The collapse of the data in figure 3.10 is confirmed by evaluating the plots of f versus L_0 in figure 3.11. The oscillation frequency does not appear to be a strong function of the tube length, however it does appear to increase slightly with increasing tube length. In fact, the oscillation frequency for the M-6 tube must increase if the earlier result that $f \sim D_0^{-1/2}$ is to hold. The increase in the frequency appears most pronounced in figure 3.11(c).

As discussed in section 1.5, the work by Bertram *et al.* (1990) experimentally tested collapsible tubes with different lengths and found only a very weak dependence of the oscillation frequency on tube length. However, as the tube lengths from Bertram *et al.* (1990) increased from $4D_0$ to $34D_0$, the minimum frequency observed decreased from 4.3 to 2.0 Hz. Thus the current results confirm the results of Bertram *et al.* (1990) in that the

oscillation frequency is only a weak function of the tube length, however the sign of this relation appears to be in conflict. Bertram *et al.* (1990) state that the tube length and oscillation frequency are negatively related, whereas the current results for the M-4 and M-6 tubes suggest that the length and frequency may be positively related. This difference clearly warrants more study.

One suggestion for the oscillation mechanism is that waves traveling axially along the tube are responsible for modulating the oscillations. Using the Moens-Kurteweg equation (cf. Fung 1997, pg. 144) for thin-walled (albeit constant diameter) tubes, the speed of traveling waves, c, in the PVG tube goes as $c \sim D_0^{-1}$, since the tube material, tube-wall thickness, and fluid density are all constant. Thus the oscillation frequency should be a function of the wavespeed and the length the wave travels. This would yield $f = c/2L_0$ and gives an inverse relationship between the self-excited oscillation frequency and tube length. Based on this mechanism, we would expect $f \sim D_0^{-2}$ or $f \sim L_0^{-1}$ for the constant shape or constant length experiments, respectively. However, the current work did not find this to be the case experimentally. Our experiments indicate a much weaker dependence on physical dimensions confirming that wave propagation along the full length of the tube is not an explanation for the observed self-excited oscillations.

Considering the pressure waveforms shown in figure 3.12, we can inspect more closely the differences between tubes of different length. Qualitatively, the same conclusions from section 3.5.1 hold, particularly with regards to the relative magnitudes of the P_1 and P_2 oscillations. We can see that amongst all of the tubes considered, that in general there is steady flow entering into the PVG device and pulsed flow exiting.

3.5.3 General Discussion

As a means of elucidating the possible mechanism, let us consider the current results that yield the scaling $f \sim D_0^{-1/2} L_0^0$. Previously, the consideration of traveling waves along the tube suggested that the waves travel upstream and reflect off of the upstream rigid tube before returning to the tube throat. This yields the result that $f = c/2L_0$ where the Moens-Korteweg wavespeed (cf. Fung 1997, pg. 144) is defined as

$$c \equiv \sqrt{\frac{Eh}{\rho D_0}}, \tag{3.4}$$

which we have already shown from the current experiments and the work of Bertram *et al.* (1990) to not be consistent with the experimental findings. However, an alternative mechanism could be such that the traveling waves move downstream of the tube throat. This would result in wave travel distance being the length between the throat of the collapsible tube (the point of minimum cross-sectional area) and the rigid tube connection downstream, defined as l_t. With $2l_t$ as the complete wave travel length, this yields an expression for the predicted frequency such that

$$f_p = \sqrt{\frac{Eh}{4\rho D_0 l_t^2}}, \tag{3.5}$$

and gives us the scaling observed in the experiments, assuming that l_t is not a function of D_0 or L_0. Note, in this assumption, we are neglecting the resistance of the air to the nozzle during its oscillation cycle. This is done as the inner fluid in our experiments was water and is likely to impact the oscillations of the PVG to a far higher degree than the exterior air due to its significantly higher density.

To obtain an approximation of what the length of l_t would be and its relation to D_0 and L_0, let us consider the pressure drop along different collapsible tubes from the experiments,

plotted in figure 3.13. As only the pressure at the upstream, P_1, and downstream, P_2, of the tube were measured, the axial distribution of the pressure has been approximated as a straight line. The values of P_1 and P_2 used the values of the pressure from figures 3.7 and 3.12 at $t = 0$, which is nearly coincident with the point of maximal collapse at the tube throat.

If we further assume that there is a critical pressure, P_{crit}, where the tube is significantly collapsed for $P(x) < P_{crit}$, then this provides an approximation for the length of the downstream collapsed portion of the tube, l_t, where l_t is shown to be the point where $P(x) = P_{crit}$. The value of P_{crit} and the average wave travel distance, $\bar{l}_t$, are shown in figure 3.13. An approximate value of P_{crit} could be obtained from an experiment that yields results similar to that of figure 2.3(a) where P_{crit} would be the onset of significant tube collapse (approximately $P_t/K_{P,\infty} > 10$ for figure 2.3(a)). However the results of figure 2.3(a) were obtained with tubes that were significantly longer than that used in the current experiments ($L_0/D_0 = 43$). It is believed that the much shorter tubes used in the current experiment would follow a different collapse curve. It should be noted that for all of the tubes tested, it was observed that the collapsed portion of the tube was consistently at the downstream end of the tube, which is consistent with figure 3.13. Furthermore, the value of $P(x)$ relative to P_{crit} does not directly indicate the magnitude of the local tube collapse (e.g., for $P(x) > P_{crit}$, the tube is not necessarily fully distended and for $P(x) < P_{crit}$ the tube is not necessarily fully collapsed).

From figure 3.13 one can see that for an assumed P_{crit} of −4 kPa, that the value of l_t does not vary much. This chosen value of P_{crit} is reasonable as it is within the range of observed P_2 (cf. figure 3.13). The average values of the wave travel distance, $\bar{l}_t$, are both $\mathcal{O}(10^{-2})$ m. Thus we can consider that l_t is not a function of D_0 or L_0 and that equation (3.5) is a

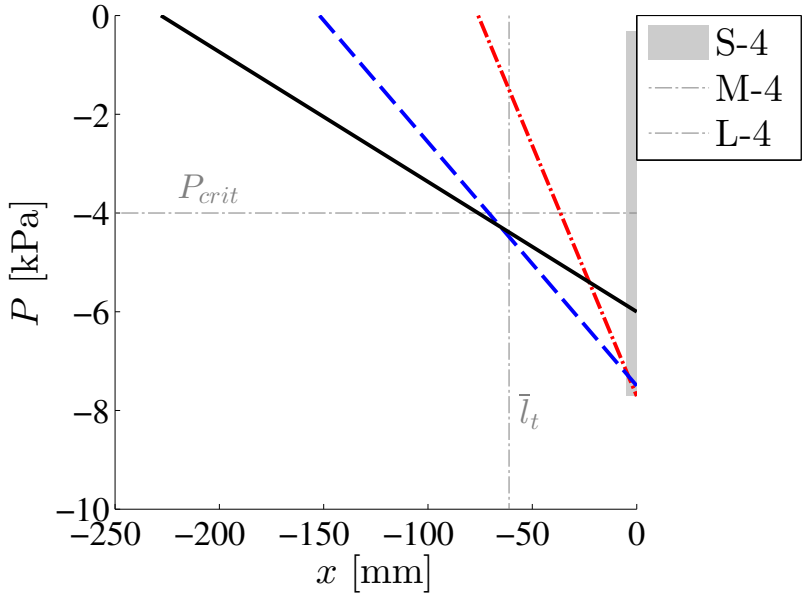

(a) Plot of the S-4, M-4, and L-4 tubes using data from figure 3.7(a) at $t = 0$. This yields $\bar{l}_t = 61$ mm for $P_{crit} = -4$ kPa.

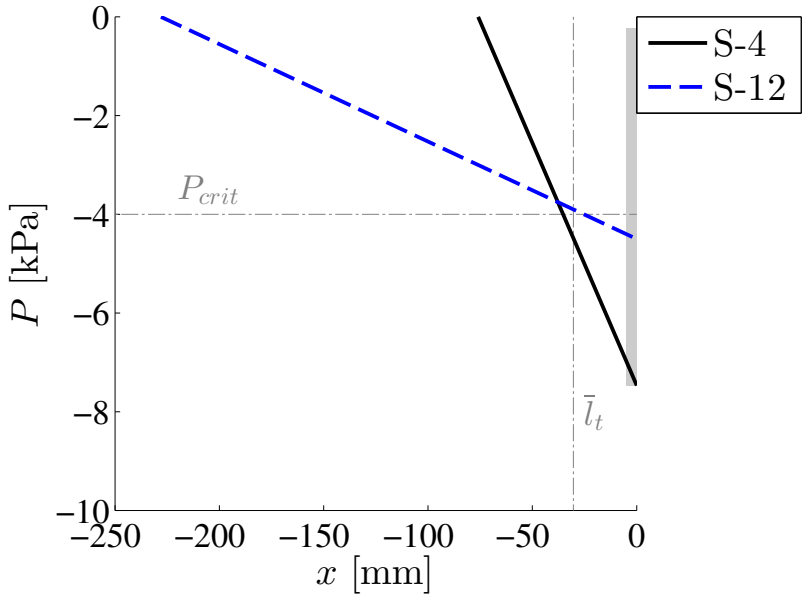

(b) Plot of the S-4 and S-12 tubes using data from figure 3.12(a) at $t = 0$. This yields $\bar{l}_t = 30$ mm for $P_{crit} = -4$ kPa.

Figure 3.13: Plot illustrating the pressure drop as a function of the axial distance, x, along the collapsible tube. The axial distances have been aligned such that the end of the tube indicates $x = 0$. The values of P_1 ($P(x = -L_0)$) and P_2 ($P(x = 0)$) are obtained from figures 3.7 and 3.12 at $t = 0$. The range of $P_2(t)$ for all tubes from the respective data set is indicated by the gray patch on the right hand side of the plot. The location of the mean wave travel distance, $\bar{l}_t$ is also shown.

relation for the oscillation frequency that scales according to the observed experimental results. Even though equation (3.5) may yield the correct scaling, let us consider whether it is quantitatively correct. If one assumes that $l_t = 4$ cm, which is a reasonable value given the results of figure 3.13, this yields $f_p \approx 16$ Hz.* This is within the range of observed frequencies of 10–18 Hz (cf. figures 3.3 and 3.5). Thus this mechanism is reasonable to explain the experimental results observed.

Based on the aforementioned measurements and theory, we propose that the governing mechanism for self-excited oscillations is as follows: the sudden collapse of the tube at the throat due to Bernoulli's effect generates traveling waves; the downstream traveling wave reflects off of the boundary between the collapsible tube and the rigid tube; the reflected wave then travels back upstream and causes the tube throat to open; allowing more fluid to flow due to a lessened restriction on the flow; and then the cycle repeats repeats itself. The significance of the tube throat's axial location, l_t, and traveling waves was also speculated by Cancelli & Pedley (1985) as part of mechanism behind the self-excited oscillations. However, Cancelli & Pedley (1985) indicated that the separation downstream of the throat was a more dominant cause.

*assuming $E = \mathcal{O}(10^6)$ Pa, $h = \mathcal{O}(10^{-4})$ m, $\rho = 1000$ kg m^{-3}, and $D_0 = 38$ mm

Chapter 4

Summary and Recommendations

The present work conducted two series of experiments. The first set of experiments integrated a PVG into a self-propelled autonomous underwater vehicle (AUV). These experiments looked at the hydrodynamic efficiency of the vehicle under various oscillation conditions, controlled by the propeller throttle setting, T, and amount of air in the PVG chamber, related to τ. Furthermore, consideration of the vortex dynamics of the produced vortex rings was addressed. It was found that a maximization of the hydrodynamic efficiency yielded a vortex ring structure was that coincident with the onset of vortex ring pinch-off. This point yielded a 22% increase in the hydrodynamic efficiency of the same system without self-excited oscillations.

The second set of experiments considered the effect of changing physical dimensions on the characteristics of self-excited oscillations produced by a passive vortex generator (PVG). The effect of changing the tube diameter and the tube length were considered. In the end, it was found that changing these two significant physical dimensions appeared to have a weak effect on the frequency of oscillation. This leaves open the possibility of creating devices of varying size with no significant effects on the oscillation characteristics.

This study, however, still leaves some important questions unanswered. In regards to the PVG-integrated AUV, the device was able to obtain a significant increase in the

hydrodynamic efficiency, however the power coefficient (C_p from Ruiz 2010) was worse for the pulsed jet case over the steady jet case. The lack of an increase in the overall efficiency shows that this exact embodiment should be refined before considering implementing this into a future vehicle. However, the results from this work do reinforce the importance of the vortex formation time as being a key factor when designing a vortex-based propulsion system.

Another point that needs additional consideration is the issue of the type of jet that is formed. As mentioned in section 2.3.8, the "robosquid" vehicle has a very different efficiency versus formation time curve from that of the current vehicle and the vehicle of Ruiz (cf. figure 2.30). It has been speculated that this could be due to the wake structure of the vehicles, as "robosquid" generates a fully pulsed jet whereas the current vehicle and the vehicle of Ruiz generate a steady jet with significant perturbations (i.e., U_j does not go to zero between pulses). It is not clear if this is a complete explanation for the difference between the efficiency trends, but two features of the efficiency trends are worth investigating. The first is the discrepancy at low formation time. The work of Moslemi & Krueger (2010, 2011) using "robosquid" found that decreases in $\hat{t}/F$ lead to increase in η_p/η. The opposite was found for the current work. The other feature of the efficiency plots worth investigating is the significant peak in efficiency for the current vehicle for $\hat{t}/F = 1$ (this could also be true for the vehicle of Ruiz (2010)). This is clearly a consequence of maximizing the vortex ring circulation, however, why it is not as pronounced in the "robosquid" results is not clear. Further work into identifying the significance of these wake structures in the context of vehicle propulsion could shed light on these questions.

In regards to the self-excited oscillations, we have shown that for the test conditions explored here that the oscillation frequency goes as $f \sim D_0^{-1/2} L_0^0$. However, the mechanism

of the self-excited oscillations is still not well understood. From an experimental standpoint, part of this issue lies with the difficulty in obtaining optical access to the inside of the tubes to determine the flow field. This could be resolved by building a "two-dimensional" collapsible channel experiment. The construction of a very wide channel with the elastic membrane along the long side of the channel could make the channel two-dimensional enough (invoking an approximation akin to the thin-gap approximation) and yet still enable optical access from the side or bottom for obtaining data for particle image velocimetry. The large width of the channel would allow for the elastic membrane in the center of the channel to have minimal influence from the edges.

Alternatively, recent advances in three-dimensional experimental velocimetry techniques could yield considerable new avenues of research in this field. The techniques include defocused digital particle image velocimetry (Pereira & Gharib 2002), tomographic particle image velocimetry (Elsinga *et al.* 2006), and light-field-based PIV (Lynch 2011). However, all of these techniques are optical techniques that require a careful experiment to ensure that optical access to the particle-laden fluid inside of the tube is not distorted. Should this consideration be accounted for, then the three-dimensional, time-resolved flow field of a collapsible tube undergoing self-excited oscillations would be of considerable significance. A better understanding of the complete fluid flow-field would then enable better descriptions of the mechanism.

In particular, finding experimental proof of the mechanism suggested would be greatly enhanced by obtaining the flow field in the tube downstream of the throat. This is a region of significant tube deformation, and thus an experiment to observe flow in this region must be carefully designed. One could imagine surrounding the collapsible tube with an index-of-refraction-matched liquid and use the same liquid as the working fluid for the oscillations.

This is feasible as there are clear silicones available, however an experiment such as this would sacrifice the kinematics observed in this current work as the fluid surrounding the tube would surely alter the tube kinematics due to the significant density of the fluid compared to the density of air.

Another means of obtaining the flow field downstream of the throat would be to use an open-ended nozzle such as that used in these experiments along with an imaging setup looking upstream directly into the nozzle. This would allow the camera to visualize all of the particles in the flow downstream of the throat, which is suggested to be the region of importance to the self-excited oscillations. This would require a three-dimensional PIV setup to properly obtain the data set, and careful choice of the equipment would be necessary to adequately resolve the out-of-plane component as it would be the dominant velocity in this type of a flow. Should such a setup be obtained, then this would alleviate the need to index-match the fluids and also would preserve the tube kinematics observed in these experiments as the chamber could continue to be filled with only air. One can think of the dynamics of the system being affected through the added-mass from the external fluid affecting the tube wall accelerations and potentially the creation of secondary external flows that could affect the tube's dynamics. These external effects are all proportional to the density of the external fluid and, since the density of air is generally assumed to 815 times less than that of water, these effects have currently been considered to be negligible compared to the internal working fluid.

Because the suggested mechanism relies on traveling waves which would likely have a pressure component to them, the importance of numerical work to this area of study cannot be mitigated as simulations provide the complete flow field as well as the pressure field. As improvements to both computational hardware and algorithms improve, it is likely

that the gap between what the numerics are capable of and what the experiments do will be narrowed over time. However, the current study suggests simulations that are fully three dimensional without any geometry assumptions, as the current experiments found the azimuthal tube buckling to have mode 3 buckling rather than the mode 2 buckling that is commonly proscribed in current simulations.

Appendix A

Schematic Drawings of the PVG-Integrated AUV

This appendix includes schematic drawings of the PVG-integrated AUV. Each figure shows an element of the system with important dimensions indicated. Figure A.1 shows the overall vehicle system. Figure A.2 shows a drawing of the recipient vehicle. Figure A.3 shows a schematic drawing of the inner frame of the PVG where the collapsible tube was mounted. Figure A.4 shows a schematic drawing of the outer cover of the PVG.

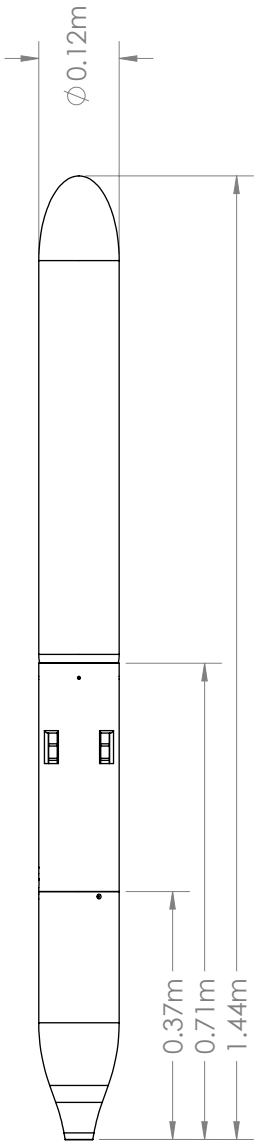

Figure A.1: Schematic drawing of the entire PVG-integrated AUV.

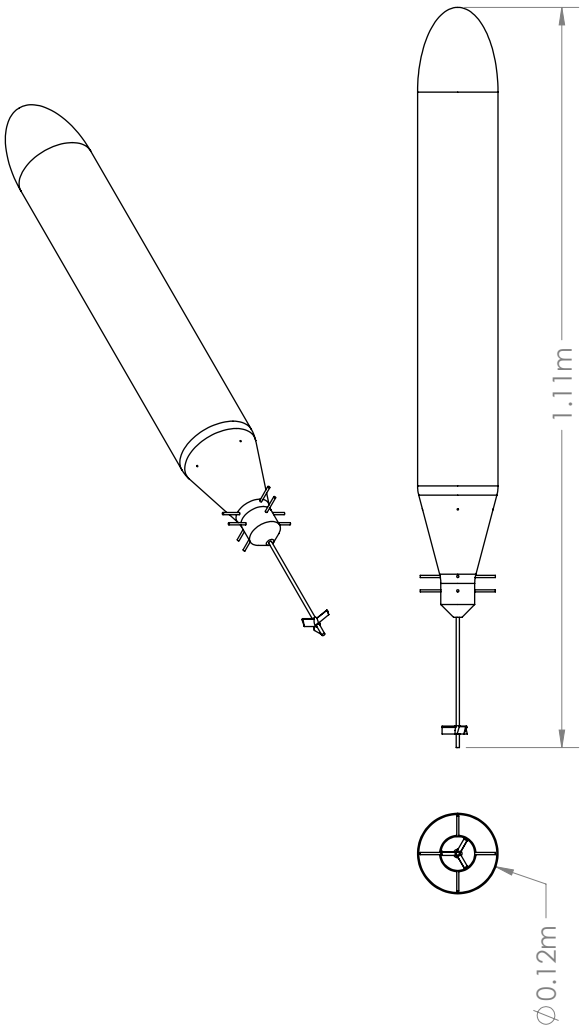

Figure A.2: Schematic drawing of the main vehicle.

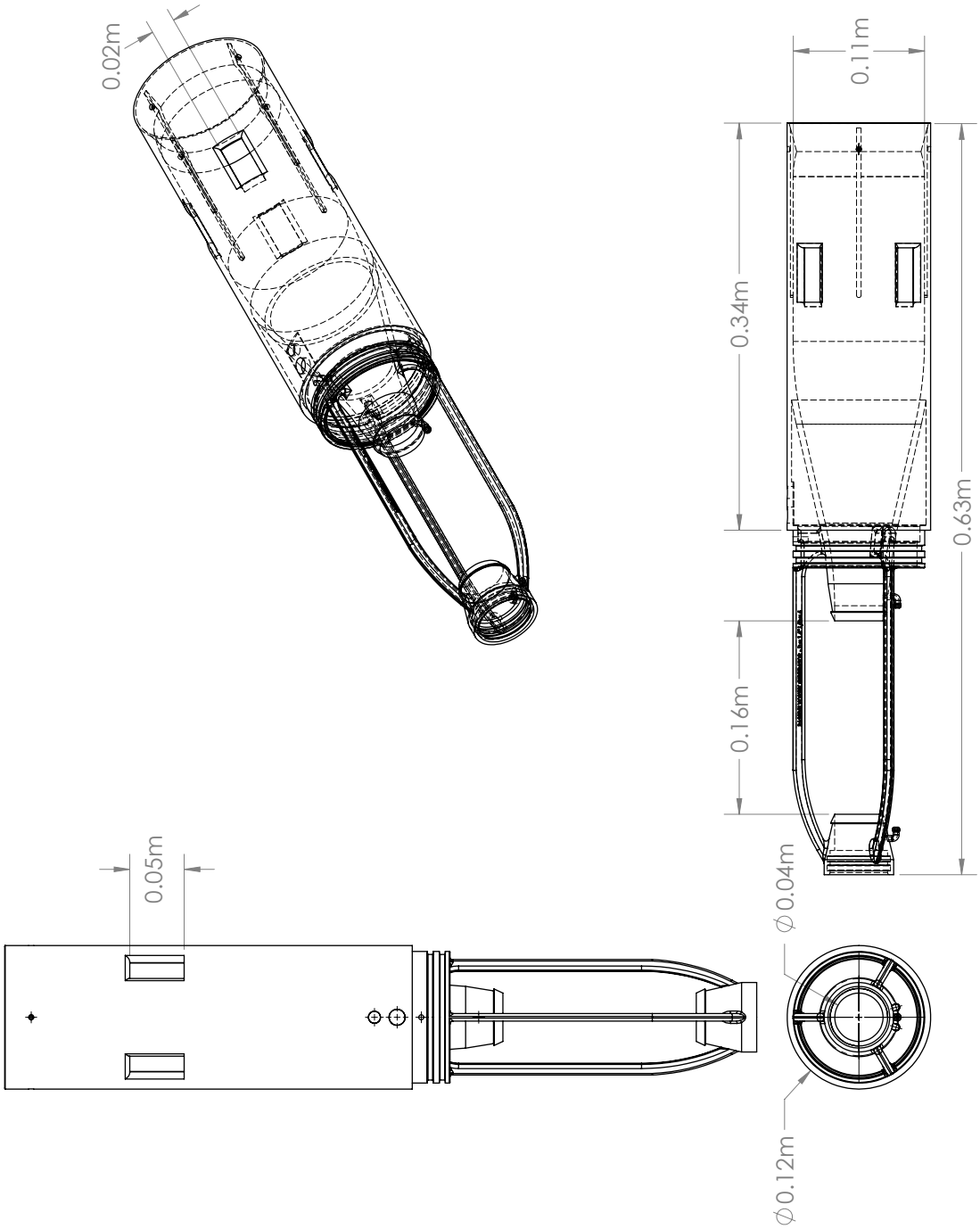

Figure A.3: Schematic drawing of the inner frame of the PVG.

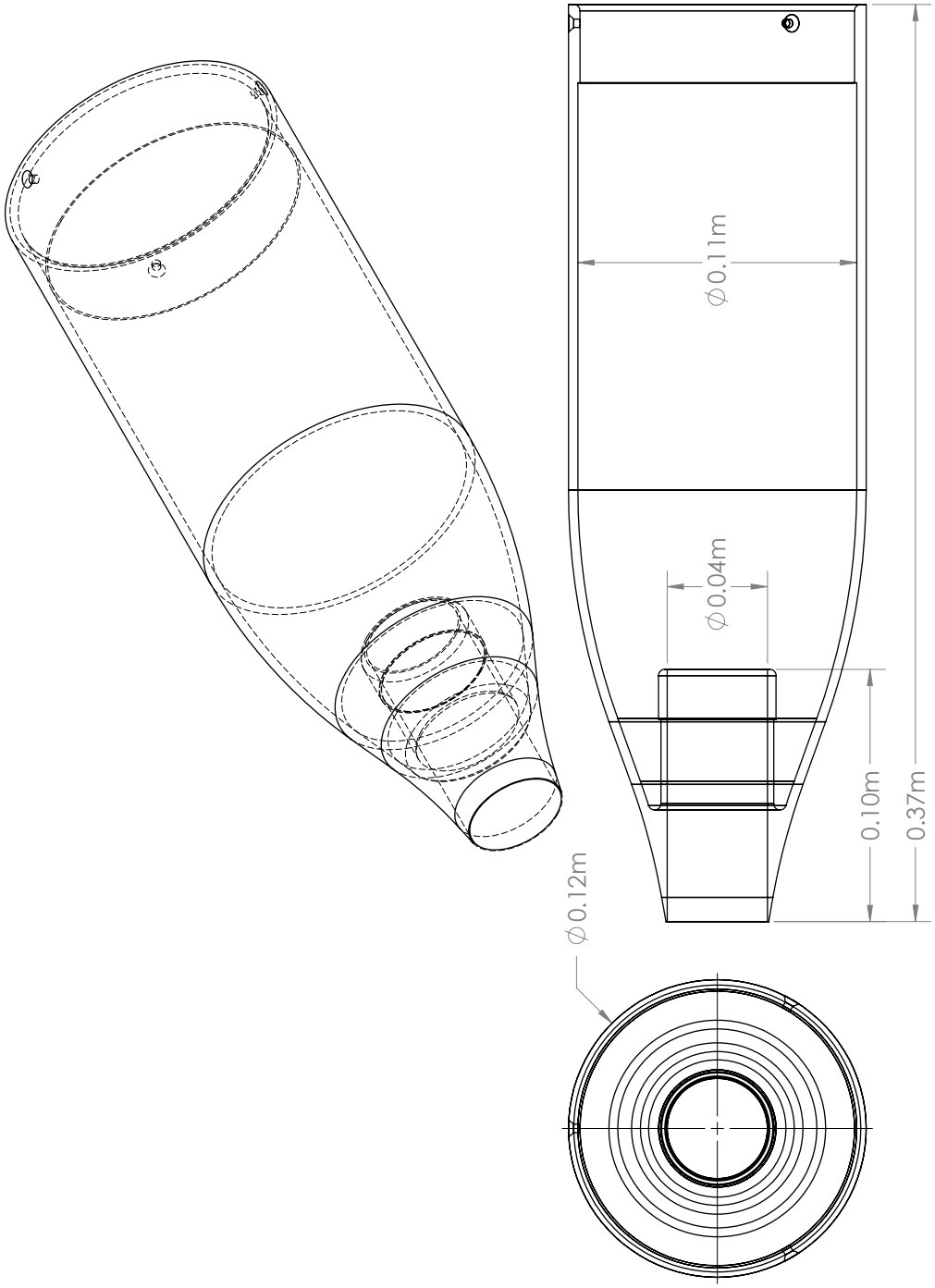

Figure A.4: Schematic drawing of the cover of the PVG.

Appendix B

Volume Ratio Derivation

If we assume that the flow into the collapsible tube has a fixed velocity profile and is not a function of time (since the fluid used in these experiments is water, this is synonymous with having a fixed mass flux) and if we assume that this tube is under going self-excited oscillations then we expect to have a time-varying, periodic mean velocity through the exit. We can then express the volume of fluid within the collapsible tube as

$$V_t(t) = \int_0^t \{U_{in} - U_{out}(t)\}\, A\, dt + \overline{V}_t, \tag{B.1}$$

where $V_t(t)$ is the instantaneous tube volume, U_{in} is the spatially averaged velocity entering the collapsible tube, $U_{out}(t)$ is the spatially averaged, time-varying velocity exiting the collapsible tube, A is the cross-sectional area of the tube at the inlet and outlet ($A = \pi D_0^2/4$), and $\overline{V}_t$ is the average tube volume.

If we assume that the oscillation of the tube is periodic (and experiments show that it generally is), then we can show that during a period of oscillation there is a minimum and maximum of the tube volume, which we will denote as V_t^- and V_t^+, respectively. Then, let

us define a tube-collapse factor, β, such that

$$\beta \equiv 1 - \frac{V_t^-}{V_t^+}, \tag{B.2}$$

which can be interpreted as indicating the amount of tube collapse on a percentage basis and is always less than unity.

The chamber volume changes in time due to the tube volume oscillating. Thus if we assume that the chamber is constructed out of a rigid box with dimensions $L \times W \times H$ and volume V_{box}, then the chamber volume is given by

$$V_c \equiv LWH - V_t(t) = V_{box} - V_t(t), \tag{B.3}$$

and similarly because the tube volume has a minimum and maximum, the chamber volume has a minimum and maximum volume given by

$$V_c^- = V_{box} - V_t^+ \text{ and } V_c^+ = V_{box} - V_t^-, \tag{B.4}$$

respectively.

The size of the chamber affects the kinematics of the system by changing the external pressure, P_e, that forces the tube to collapse. We can model this through the ideal gas law and consider the pressure minimum and maximum during an oscillation cycle as related by

$$\frac{P_e^+}{P_e^-} = \frac{V_c^+}{V_c^-}, \tag{B.5}$$

as the chamber is a closed system.

Let us approximate the maximum tube volume, V_t^+, as equivalent to the nondeformed volume of the tube, i.e., $V_t^+ = \pi D_0^2 L_0/4$, and let us also define a volume ratio, λ, between the chamber volume and the tube volume, such that

$$\lambda \equiv \frac{V_c^-}{V_t^+}, \tag{B.6}$$

which can be calculated *a priori* based on the device geometry. The approximation of the maximum tube volume, V_t^+, will overestimate from the true value of V_t^+ and thus also overestimate the value of β while underestimating the value of λ.

We can solve for the ratio between the maximum and minimum chamber pressures as follows:

$$\frac{P_e^+}{P_e^-} = \frac{V_c^+}{V_c^-}, \tag{B.7}$$

$$\frac{P_e^+}{P_e^-} = \frac{\frac{V_c^+}{V_t^+}}{\frac{V_c^-}{V_t^+}}, \tag{B.8}$$

$$\frac{P_e^+}{P_e^-} = \frac{\left(\frac{V_{box} - V_t^-}{V_t^+}\right)}{\lambda}, \tag{B.9}$$

$$\frac{P_e^+}{P_e^-} = \frac{\left\{\frac{\left(V_{box} - V_t^+\right) + \left(V_t^+ - V_t^-\right)}{V_t^+}\right\}}{\lambda}, \tag{B.10}$$

$$\frac{P_e^+}{P_e^-} = \frac{\frac{V_{box} - V_t^+}{V_t^+} + \frac{V_t^+ - V_t^-}{V_t^+}}{\lambda}, \tag{B.11}$$

$$\frac{P_e^+}{P_e^-} = \frac{\frac{V_c^-}{V_t^+} + 1 - \frac{V_t^-}{V_t^+}}{\lambda}, \tag{B.12}$$

and end up with the simple expression that

$$\frac{P_e^+}{P_e^-} = \frac{\lambda + \beta}{\lambda}, \tag{B.13}$$

which can be expressed as a percent change where $\Delta P_e \equiv (P_e^+ - P_e^-)/P_e^-$ to find

$$\Delta P_e = \frac{\beta}{\lambda}, \tag{B.14}$$

and that $\Delta P_e \sim 1/\lambda$. Let us remember that $0 < \beta < 1$ and thus one can see that for sufficiently large λ, that the chamber pressure remains essentially unchanged during an oscillation period. One can obtain a conservative prediction of the pressure ratio between the minimum and maximum pressure during an oscillation if one assumes that $\beta = 1$. This assumes that the tube oscillates between a nominally distended volume (equal to a cylinder with volume $V_t^+ = \pi D_0^2 L_0/4$) and zero volume. Figure B.1 shows a plot using this conservative prediction of the expected pressure change for a range of volume ratio, λ. From this plot, it is clear that a volume ratio of at least 100 ensures a negligible amount of variation of the chamber pressure during an oscillation cycle (1%, to be exact). However, as the volume ratio decreases, the pressure change quickly increases.

For low volume ratios, $\lambda < 10$, it is more likely that the varying chamber pressure will play a significant role in the dynamics of the system. This is because as the tube volume decreases (due to a positive transmural pressure), the chamber pressure will decrease and ultimately cease the collapse of the tube (as the transmural pressure would have gone to zero). It is possible that for very small volume ratios one could imagine this interaction as a plausible mechanism for the self-excited oscillations, however because $\lambda > 10$ in the current work, it is not a likely mechanism for the oscillations exhibited in the current work.

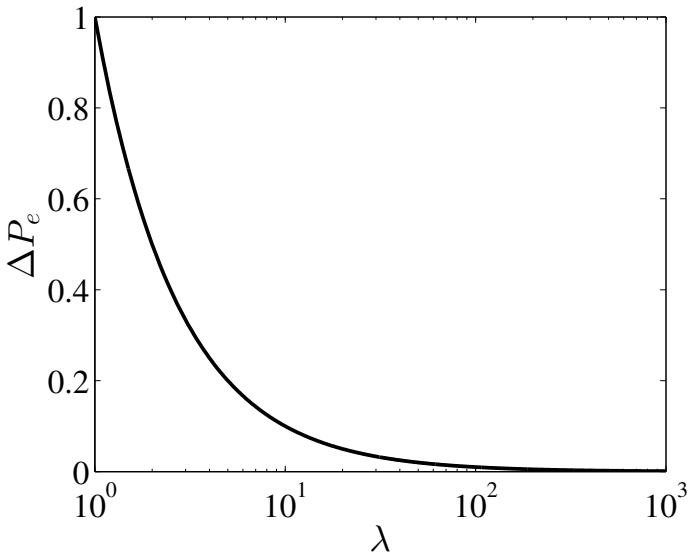

Figure B.1: Plot of equation (B.13) with $\alpha = 1$ to be conservative.

Appendix C

Derivation of Co-Flow Formation Time

A derivation of the co-flow formation time (equation (2.11)) can be shown as follows: The slug model for vortex ring formation from a piston-cylinder apparatus, where the vortex ring ejection is modeled as a slug of fluid with length L and diameter D_0, uses a control volume as shown in figure C.1. The control volume is assumed to extend to infinity in the positive r and x directions (i.e., $r \to \infty$ along "2" and $x \to \infty$ along "3").

Following the derivation from Krueger (2001, appendix D) for the growth of the total circulation ejected from the nozzle, we find that integrating the vorticity equation over the control volume of Figure C.1 yields only contributions from the line marked "1." The

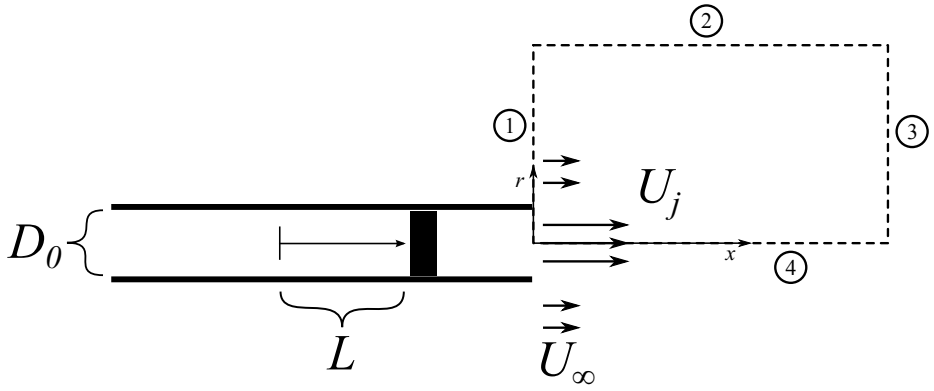

Figure C.1: Schematic of vortex ring generator and the control volume used in the slug model derivation.

contribution from "1" can be shown to only depend on the vorticity flux across the control volume's surface and is equal to

$$\frac{\partial \Gamma}{\partial t} = \int_0^\infty \left[-u_x \frac{1}{2} \frac{\partial u_x}{\partial r} - \frac{\partial u_r}{\partial t} - \frac{1}{\rho} \frac{\partial P}{\partial r} \right] \Bigg|_{x=0} dr, \tag{C.1}$$

under assumptions of axisymmetry and that $\vec{u} \to 0$ at (∞, ∞) and $u_r = 0$ at $r = 0$. The subscripts indicate flow velocity direction, e.g., u_x is parallel to the x-axis. The circulation growth can be integrated to obtain

$$\frac{\partial \Gamma}{\partial t} = -\frac{1}{2} u_x^2 \Big|_0^\infty - \frac{1}{\rho} P \Big|_0^\infty. \tag{C.2}$$

Now, for the slug model we assume that the pressure across the jet is constant and thus $P(r = 0) = P(r = \infty)$ and we obtain simply

$$\frac{\partial \Gamma}{\partial t} = \frac{1}{2} \left[u_x(r = 0)^2 - u_x(r = \infty)^2 \right], \tag{C.3}$$

or based on flow depicted in Figure C.1

$$\frac{\partial \Gamma}{\partial t} = \frac{1}{2} \left(U_j^2 - U_\infty^2 \right). \tag{C.4}$$

The nondimensional circulation growth was shown by Rosenfeld *et al.* (1998) to be equal to:

$$\frac{\partial \hat{\Gamma}}{\partial \hat{t}} = \frac{1}{2}, \tag{C.5}$$

where hats indicate non-dimensionalized quantities.

If we nondimensionalize the circulation, Γ, by the shear layer strength for our co-flow con-

ditions, $(U_j - U_\infty)D_0$, and if we seek to match the scaling of the nondimensional circulation growth used by Rosenfeld *et al.* (1998) we can calculate the required nondimensionalization of time as follows

$$\frac{\partial \Gamma}{\partial t} = \frac{1}{2}\left(U_j^2 - U_\infty^2\right), \tag{C.6}$$

$$\frac{\partial \hat{\Gamma}}{\partial t} = \frac{1}{2}\frac{\left(U_j^2 - U_\infty^2\right)}{(U_j - U_\infty)D_0}, \tag{C.7}$$

$$\frac{\partial \hat{\Gamma}}{\partial \hat{t}}\frac{\partial \hat{t}}{\partial t} = \frac{1}{2}\frac{\left(U_j^2 - U_\infty^2\right)}{(U_j - U_\infty)D_0}, \tag{C.8}$$

$$\frac{\partial \hat{\Gamma}}{\partial \hat{t}}\frac{\partial \hat{t}}{\partial t} = \frac{1}{2}\frac{(U_j - U_\infty)\,(U_j + U_\infty)}{(U_j - U_\infty)D_0}, \tag{C.9}$$

$$\frac{1}{2}\frac{\partial \hat{t}}{\partial t} = \frac{1}{2}\frac{(U_j - U_\infty)\,(U_j + U_\infty)}{(U_j - U_\infty)D_0}, \tag{C.10}$$

$$\frac{\hat{t}}{t} = \frac{(U_j + U_\infty)}{D_0}, \tag{C.11}$$

$$\hat{t} = \frac{(U_j + U_\infty)\,t}{D_0}. \tag{C.12}$$

Thus we can see that the proper non-dimensional time requires the addition of the jet velocity, U_j, to the ambient freestream velocity, U_∞.

Appendix D

Derivation of Pulsed Formation Time

The assumption of using the frequency in equation (2.11) should be considered. The formation time of a vortex ring is defined by Gharib *et al.* (1998) as

$$\hat{t}_{GRS} = \frac{L}{D_0}, \tag{D.1}$$

where D_0 is the diameter of the cylinder used to form the vortex ring and L is the length of the fluid slug ejected. The length, L, is defined as

$$L = \int_0^{t_p} U_p(t)\ dt, \tag{D.2}$$

where t_p is the duration of the jet pulsation and $U(t)$ is the speed of the fluid ejection (i.e., the speed of the piston ejecting the fluid). Let us now consider the case of a pulsing jet where there are many pulses and that it may be easier to calculate the average jet velocity, given by U_j, and the period of oscillation, T, rather than the individual pulse characteristics t_p and U_{max}; as shown in figure D.1. This assumes constant velocity pulses where $T = 2t_p$.

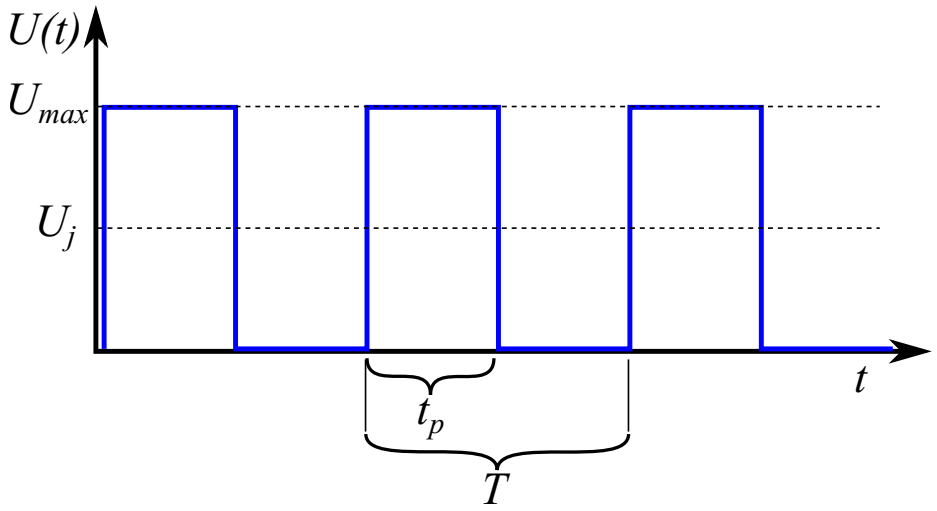

Figure D.1: Plot of the velocity of the jet, U, as a function of time, t. The maximum jet velocity achieved during a pulse is U_{max} and the average jet velocity is U_j. The pulsation duration is given by t_p and the oscillation period is T.

The definition given in the present work for the pulsed jet formation time is

$$\hat{t} = \frac{(U_j + U_\infty)}{fD_0}, \tag{D.3}$$

which we can decompose as

$$\hat{t} = \frac{U_j}{fD_0} + \frac{U_\infty}{fD_0}, \tag{D.4}$$

$$\hat{t} = \hat{t}_{jet} + \hat{t}_{co-flow}. \tag{D.5}$$

Using the assumed pulsing conditions given in figure D.1, let us construct the formation time as follows

$$\hat{t_{GRS}} = \frac{L}{D_0}, \tag{D.6}$$

$$\hat{t_{GRS}} = \frac{\int_0^{t_p} U \; dt}{D_0}. \tag{D.7}$$

Let us now consider the definition of a time average for U_j:

$$U_j = \frac{1}{T}\int_0^T U(t)\ dt, \tag{D.8}$$

$$U_j = \frac{1}{T}\int_0^{t_p} U(t)\ dt + \frac{1}{T}\int_{t_p}^T U(t)\ dt, \tag{D.9}$$

which for our assumed pulse profile reduces to

$$U_j = \frac{1}{T}\int_0^{t_p} U(t)\ dt + \frac{1}{T}\cancelto{0}{\int_{t_p}^T U(t)\ dt}, \tag{D.10}$$

$$U_j = \frac{1}{T}\int_0^{t_p} U(t)\ dt, \tag{D.11}$$

and plugging equation (D.11) into (D.7) we obtain

$$\hat{t_{GRS}} = \frac{TU_j}{D_0}, \tag{D.12}$$

and as $f = 1/T$, we obtain

$$\hat{t_{GRS}} = \frac{U_j}{fD_0}, \tag{D.13}$$

$$\hat{t_{GRS}} = \hat{t}_{jet}. \tag{D.14}$$

Thus for pulsed jets in quiescent ambient fluid (no co-flow), $\hat{t}_{jet}$, which uses the pulse frequency is identical to the formation time, $\hat{t}_{GRS}$, defined by Gharib *et al.* (1998).

However, the pulsed formation time in this work is defined using the co-flow approach (cf. Equation D.5). Thus we have to consider the $\hat{t}_{co-flow}$ term. For the $\hat{t}_{jet}$ term, because one is trading off the higher U_{max} and lower t_p for the lower U_j and the higher $1/f$, the term is equivalent to $\hat{t}_{GRS}$. However, should we encounter a fully pulsed jet (like that shown in

figure D.1) in the prescence of co-flow, then replacing U_j with U_∞ in the derivation shows that we cannot neglect its contributions between pulses (as U_∞ is constant). This will create an error by using $1/f$ rather than t_p in the $\hat{t}_{coflow}$ term. Let us consider the significance of that error.

We find the definition of the co-flow portion of the formation time from Krueger *et al.* (2003) as follows, using the current nomenclature

$$\hat{t}_{KDG,coflow} = \frac{U_\infty t_p}{D_0}, \tag{D.15}$$

$$\hat{t}_{KDG,coflow} = \frac{U_\infty}{f D_0}\frac{t_p}{T}, \tag{D.16}$$

$$\hat{t}_{KDG,coflow} = \hat{t}_{co-flow}\frac{t_p}{T}, \tag{D.17}$$

which we can find the relative error in these two terms as

$$\frac{\hat{t}_{co-flow} - \hat{t}_{KDG,co-flow}}{\hat{t}_{KDG,co-flow}} = \frac{T}{t_p} - 1. \tag{D.18}$$

Thus for the example in figure D.1, $t_p/T = 0.5$ and the formation time of just the co-flow portion is being overestimated by 100%. We can see the influence on the overall pulsed formation time by considering the complete definition for the co-flow formation time given by Krueger *et al.* (2003) as

$$\hat{t}_{KDG} = \frac{t_p U_j}{D_0} + \frac{t_p U_\infty}{D_0} \tag{D.19}$$

in the current nomenclature. This can be rewritten as

$$\hat{t}_{KDG} = \hat{t}_{jet} + \hat{t}_{co-flow}\frac{t_p}{T}. \tag{D.20}$$

We can find the relative error, ϵ, between the definition given by Krueger *et al.* (2003) versus the current definition as

$$\epsilon \equiv \frac{\hat{t}}{\hat{t}_{KDG}} - 1, \tag{D.21}$$

$$\epsilon = \frac{\hat{t}_{jet} + \hat{t}_{co-flow}}{\hat{t}_{jet} + \hat{t}_{co-flow}\frac{t_p}{T}} - 1, \tag{D.22}$$

$$\epsilon = \frac{\hat{t}_{jet} + \hat{t}_{jet}\frac{U_\infty}{U_j}}{\hat{t}_{jet} + \hat{t}_{jet}\frac{U_\infty}{U_j}\frac{t_p}{T}} - 1, \tag{D.23}$$

and using the definition of the velocity ratio, R_v, this becomes

$$\epsilon = \frac{1 + R_v}{1 + R_v\frac{t_p}{T}} - 1. \tag{D.24}$$

This gives us the magnitude of the relative error in the formation number as a function of the velocity ratio R_v and the pulse duty cycle t_p/T. For the case presented in figure D.1 where $t_p/T = 0.5$ and if we assume $R_v = 0.5$, then we find $\epsilon = 0.2$. So the overestimate of the co-flow term can certainly be significant, however let us consider the case of the current experiments.

For the current work, R_v ranged from 0.02 to 0.45 (cf. figure 2.20). To find the duty cycle of the pulses from the current work, let us consider the velocity trace of the PVG-integrated AUV shown in figure D.2. From this plot, one can see that the velocity trace is nearly sinuisoidal, and never touches the x-axis, which yields that $t_p/T = 1$ and thus $\epsilon = 0$.

This derivation shows that for unsteady jets, such as that used in the current work, that the definition of the formation time given by $\hat{t}$ is the correctly defined. However, for fully pulsed jets, where $t_p/T < 1$, the formation time definition given here will yield an overprediction of the exact formation time, with its magnitude modulated by the value of

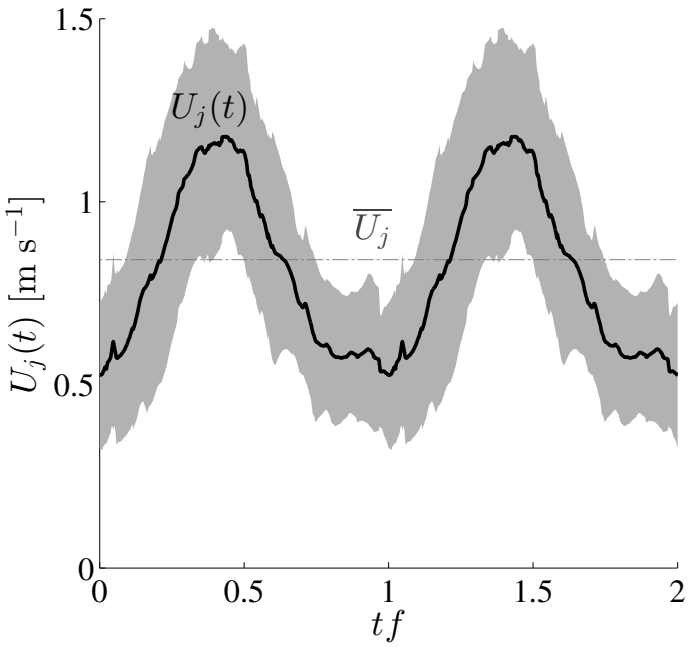

Figure D.2: Plot of the phase-averaged velocity from the PVG integrated AUV for $T = 1450$ and $\tau = 9$ alongside the average jet velocity given as the dot-dashed line in grey. The phase-averaged velocity used the pressure transducer data for obtaining the frequency and is averaged over 20 periods with the standard deviation of the data from each phase indicated by the light gray band.

R_v. For higher values of R_v, this overprediction is diminished, however as the values of R_v decrease, this overprediction will increase.

Appendix E

Discussion of Unsteady versus Steady Froude Efficiencies

The Froude efficiency definition used in the current work (equation 1.4) makes several assumptions for its derivation. The one assumption that is immediately invalidated is the assumption of steady flow. Because of this invalidated assumption, let us consider a more thorough derivation of the Froude efficiency for unsteady flows. To begin, consider the control volume around a propeller depicted in figure E.1.

The control depicted shows fluid moving at the freestream velocity, U_∞, entering the control volume over area 1 and exiting the control volume at the jet velocity, U_j, over area 2. A general form of the derivation for the Froude efficiency compares the useful work, given by the product of the thrust force, F_T, and the freestream velocity, U_j, to the power

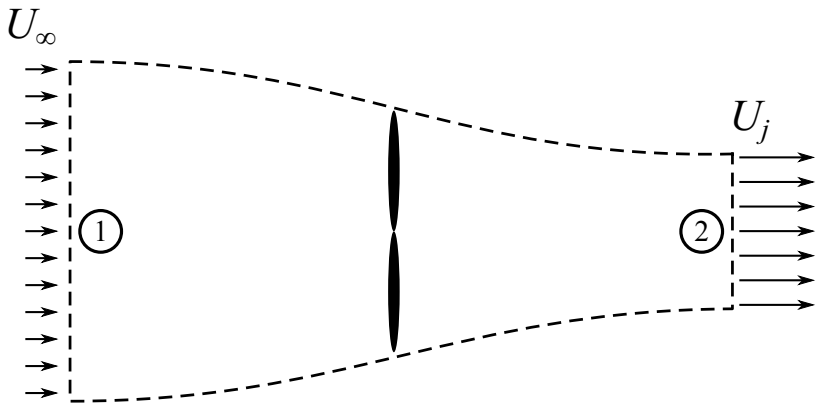

Figure E.1: Drawing of the control volume around a propeller

consumed by the propeller, P, which can be found by balancing the energy entering and exiting the control volume. This yields a general relation for the Froude efficiency, η, as

$$\eta = \frac{F_T U_\infty}{P}. \tag{E.1}$$

We can substitute the thrust force for the momentum that has been added to the flow and similarly for the power, P, we can substitute the energy added to the flow as

$$\eta = \frac{\rho\left(A_2 U_j^2 - A_1 U_\infty^2\right) U_\infty}{\frac{\rho}{2}\left(A_2 U_j^3 - A_1 U_\infty^3\right)}, \tag{E.2}$$

where A_1 and A_2 are the areas of the control volume over the surfaces 1 and 2, respectively. We have thus far assumed that U_j and U_∞ are spatially uniform over surfaces 1 and 2 and that there is no flow through the sides of the control volume, only at the inlet and exit. Let us now decompose the jet velocity into a time-averaged component and a time-varying component, which we will assume is a sinusoid with dimensional magnitude γ', such that

$$U_j = \overline{U}_j + U_j'(t), \tag{E.3}$$

$$U_j = \overline{U}_j + \gamma' \sin(t), \tag{E.4}$$

where the overline indicates a time average. We can nondimensionalize the magnitude of the sinusoid as $\gamma' = \gamma \overline{U}_j$ and obtain

$$U_j = \overline{U}_j \left(1 + \gamma \sin(t)\right). \tag{E.5}$$

Thus the value of γ' is the exact value magnitude of the oscillation amplitude whereas γ

is the value of the oscillation amplitude relative to the magnitude of the time-averaged jet velocity, $\overline{U}_j$. This relation can be replaced into our efficiency equation which now is integrated over one period of oscillation to find

$$\overline{\eta}' = \frac{2}{T}\int_0^T \frac{\left(A_2\overline{U}_j^2\left(1+\gamma\sin(t)\right)^2 - A_1U_\infty^2\right)U_\infty}{A_2\overline{U}_j^3\left(1+\gamma\sin(t)\right)^3 - A_1U_\infty^3}dt, \tag{E.6}$$

where the overline and prime has been added to the left-hand side to indicate the time-average of the time-varying Froude efficiency.

We can now consider the conservation of mass through the control volume to find $\rho A_1 U_\infty = \rho A_2 \overline{U}_j$ such that our efficiency expression now becomes

$$\overline{\eta}' = \frac{2}{T}\int_0^T \frac{\left(\overline{U}_j\left(1+\gamma\sin(t)\right)^2 - U_\infty\right)U_\infty}{\overline{U}_j^2\left(1+\gamma\sin(t)\right)^3 - U_\infty^2}dt. \tag{E.7}$$

Let us make another nondimensional parameter for the velocity where we nondimensionalize the average jet velocity, $\overline{U}_j$, by the freestream velocity, U_∞, where $\mu = \overline{U}_j/U_\infty$ to obtain another form of our unsteady efficiency

$$\overline{\eta}' = \frac{2}{T}\int_0^T \frac{\mu\left(1+\gamma\sin(t)\right)^2 - 1}{\mu^2\left(1+\gamma\sin(t)\right)^3 - 1}dt. \tag{E.8}$$

One cannot easily obtain an analytical expression for this definite integral, and thus we have chosen to evaluate this expression numerically. However, let us consider the form of this integral for our unsteady efficiency. First, we find that for certain values of μ and γ, that the denominator, which is normally positive, can become negative. The zero-crossing of the denominator causes the integrand to become unbounded and thus we restrict ourselves to values of μ and γ which ensure that the denominator is always positive and thus never

equals 0. The range of allowable values can be found from evaluating

$$\mu^2 \left(1 + \gamma \sin(t)\right)^3 - 1 > 0, \tag{E.9}$$

to obtain the maximum γ allowed as

$$\gamma_{max} = 1 - \mu^{-2/3}, \tag{E.10}$$

under consideration of the range of values of $\sin(t)$ and that $\mu > 1$ for self-propelled vehicles. Thus we restrict $\gamma < \gamma_{max}$. This criteria can physically be thought of as restricting the system to ensure that power is delivered to the fluid, rather than extracted from the fluid. If the system generates power, then the denominator would be negative and the vehicle would not be self-propelled.

We can obtain an estimate of the error, ϵ_η in the steady Froude efficiency, η, compared to our unsteady Froude efficiency, $\overline{\eta}'$, such that $\epsilon_\eta = (\eta - \overline{\eta}')/\overline{\eta}'$. Values of $\epsilon_\eta > 0$ indicate that the steady efficiency overestimates the unsteady efficiency whereas $\epsilon_\eta < 0$ indicates that the steady efficiency underestimates the unsteady efficiency, $\overline{\eta}'$. A plot of ϵ_η is given in figure E.2 for a range of μ from 2 to 64 and γ from 0 to γ_{max}. The results of figure E.2 show that the overall trend for γ varies depending on the value of μ. For $\mu = 8$, the steady Froude efficiency, $\eta = 0.22$, approximates well the unsteady form of the Froude efficiency, $\overline{\eta}'$, for many values of γ. However, for lower and higher values of μ, the error in the use of the steady efficiency can be quite large and the sign of the error varies as well.

It should be noted that as γ nears γ_{max}, the behavior of the function $\overline{\eta}'$ becomes rather unusual. As seen in figure E.2, the error appears to increase rapidly as γ increases, however there is actually a vertical asymptote in γ after which the values of ϵ_η come from negative

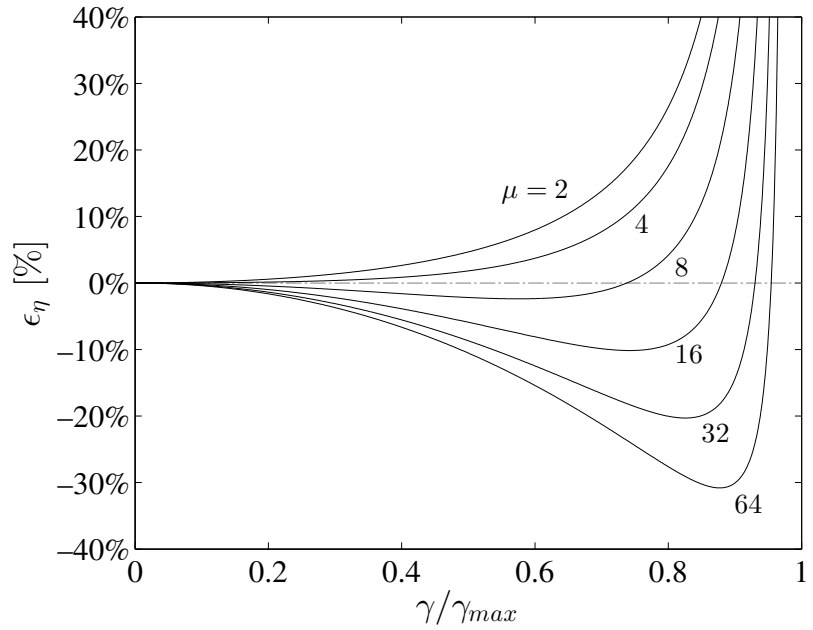

Figure E.2: Plot of the error in the steady efficiency, ϵ_η, versus the relative jet velocity oscillation magnitude, γ, normalized by γ_{max}. The lines indicate varying values of μ ranging from 2 to 64.

infinity and finally $\epsilon_\eta \to -100\%$ as $\gamma/\gamma_{max} \to 1$ (this other "branch" in the curve is not visible in figure E.2). We define the value of the asymptote as γ_{crit} such that $\lim_{\gamma \to \gamma_{crit}^-} \epsilon_\eta \to +\infty$ and $\lim_{\gamma \to \gamma_{crit}^+} \epsilon_\eta \to -\infty$.

This asymptotic behavior is driven by the trough of the numerator approaching 0^+ which causes the unsteady efficiency value to drop, thus yielding high values of ϵ_η. This can be seen by evaluating figure E.3; especially through comparing the relative magnitude of the troughs between figures E.3(c) for lower γ and E.3(d) for higher γ. For $\gamma_{crit} < \gamma < \gamma_{max}$, as in figure E.3(d), the trough of the numerator becomes negative while the trough of the denominator is positive, but very small, as it approaches 0^+. The trough region causes the integrand to have significant negative contributions to the resulting integral as shown in figure E.3(d). As $\gamma \to \gamma max$, $\overline{\eta}' \to -\infty$ which results in $\epsilon_\eta \to -100\%$ as mentioned previously. A plot of the values of γ_{max} and γ_{crit} versus μ is shown in figure E.4.

For the self-propelled experiments conducted in this current work, μ ranged from 2.25–

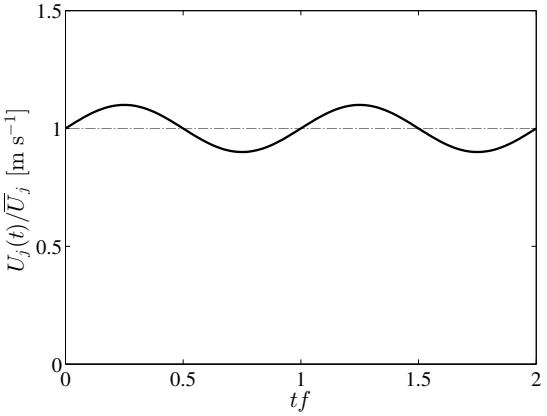

(a) Plot of $U_j(t)$ normalized by $\overline{U}_j$ over two periods of the oscillation cycle for μ = 2 and γ = 0.1. For these conditions, $\gamma < \gamma_{crit} < \gamma_{max}$.

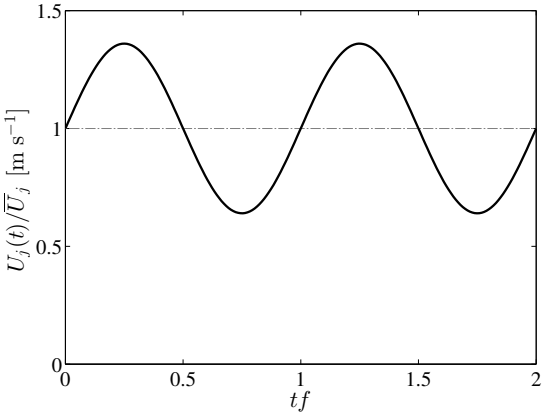

(b) Plot of $U_j(t)$ normalized by $\overline{U}_j$ over two periods of the oscillation cycle for μ = 2 and γ = 0.36. For these conditions, $\gamma_{crit} < \gamma < \gamma_{max}$.

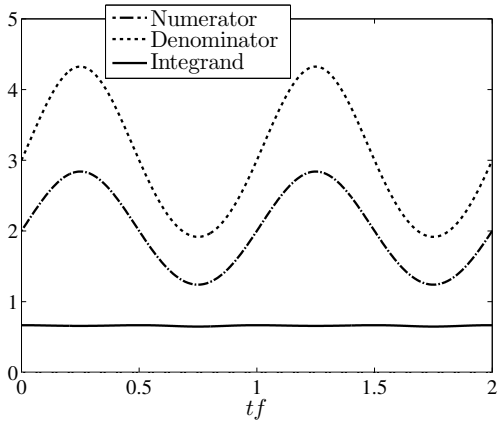

(c) Plot of the numerator and denominator contributions and the resulting integrand over two oscillation cycles for μ = 2 and γ = 0.1. For these conditions, $\gamma < \gamma_{crit} < \gamma_{max}$.

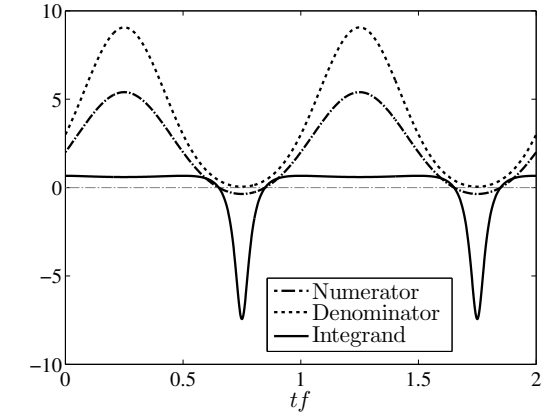

(d) Plot of the numerator and denominator contributions and the resulting integrand over two oscillation cycles for μ = 2 and γ = 0.36. For these conditions, $\gamma_{crit} < \gamma < \gamma_{max}$. Zero is indicated by a gray dot-dashed line.

Figure E.3: Plots of the jet velocity and components of the integrand in $\overline{\eta}'$ for μ = 2 and two values of γ.

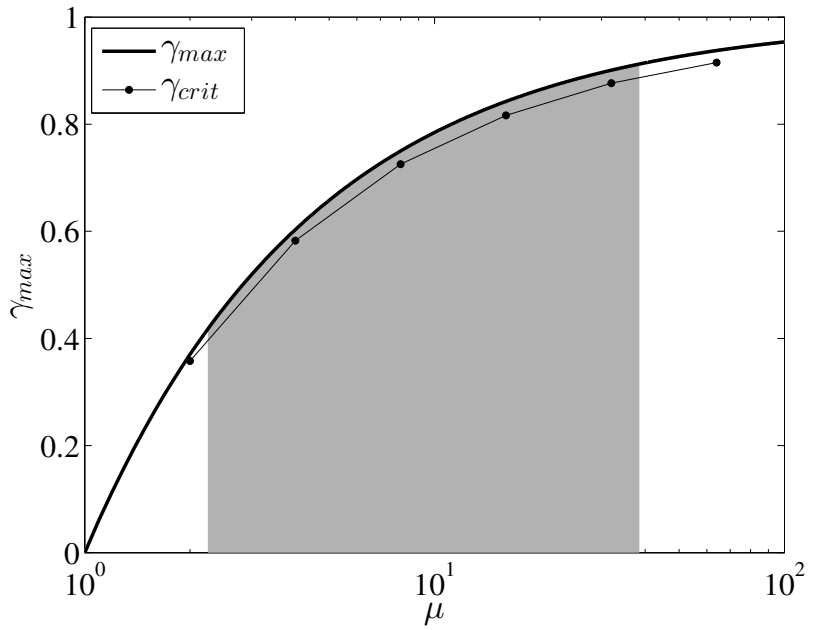

Figure E.4: Plot of γ_{max} and γ_{crit} versus μ. The darkened region indicates the range of μ observed in the self-propelled PVG experiments.

38.5. However, the actual error in the the Froude efficiency is a function of γ, which was not calculated for every self-propelled run of the PVG-integrated AUV. However, a qualitative evaluation of figure 2.16 shows that γ can range from 0–1 just by evaluating the results for the T = 1500 conditions. A particular condition of interest are the conditions of T = 1700,τ = 10 s, which yielded the peak in the normalized efficiency, $\eta/\overline{\eta}_6$. For T = 1700 and τ = 10 s, we find μ = 2.3 and by inferring that half the peak-to-peak amplitude of the phase-average jet velocity signal is γ' we find γ = 0.25. This yields ϵ_η = 6.9%. For reference, the conservative error bars in figure 2.23 give the range of efficiency improvement for T = 1700, τ = 10 to be 7.4%–34.8%; thus even with a correction for the unsteadiness in the Froude efficiency, the concluding result of this work that pulsed jets with vortex rings improve the hydrodynamic efficiency of a vehicle over steady jets remains unchanged.

Appendix F

Phase-Averaged Dye Visualizations

Figure F.1: Averaged dye visualization for T = 1300 and τ = 0 s. Phase-averaged frame consists of 51 frames are stacked.

Figure F.2: Averaged dye visualization for T = 1300 and τ = 4 s. Phase-averaged frame consists of 51 frames are stacked.

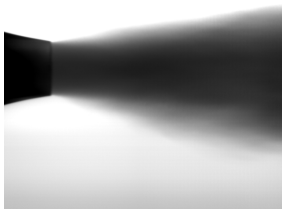

Figure F.3: Averaged dye visualization for T = 1300 and τ = 6 s. Phase-averaged frame consists of 69 frames are stacked.

Figure F.4: Averaged dye visualization for T = 1300 and τ = 8 s. Phase-averaged frame consists of 105 frames are stacked.

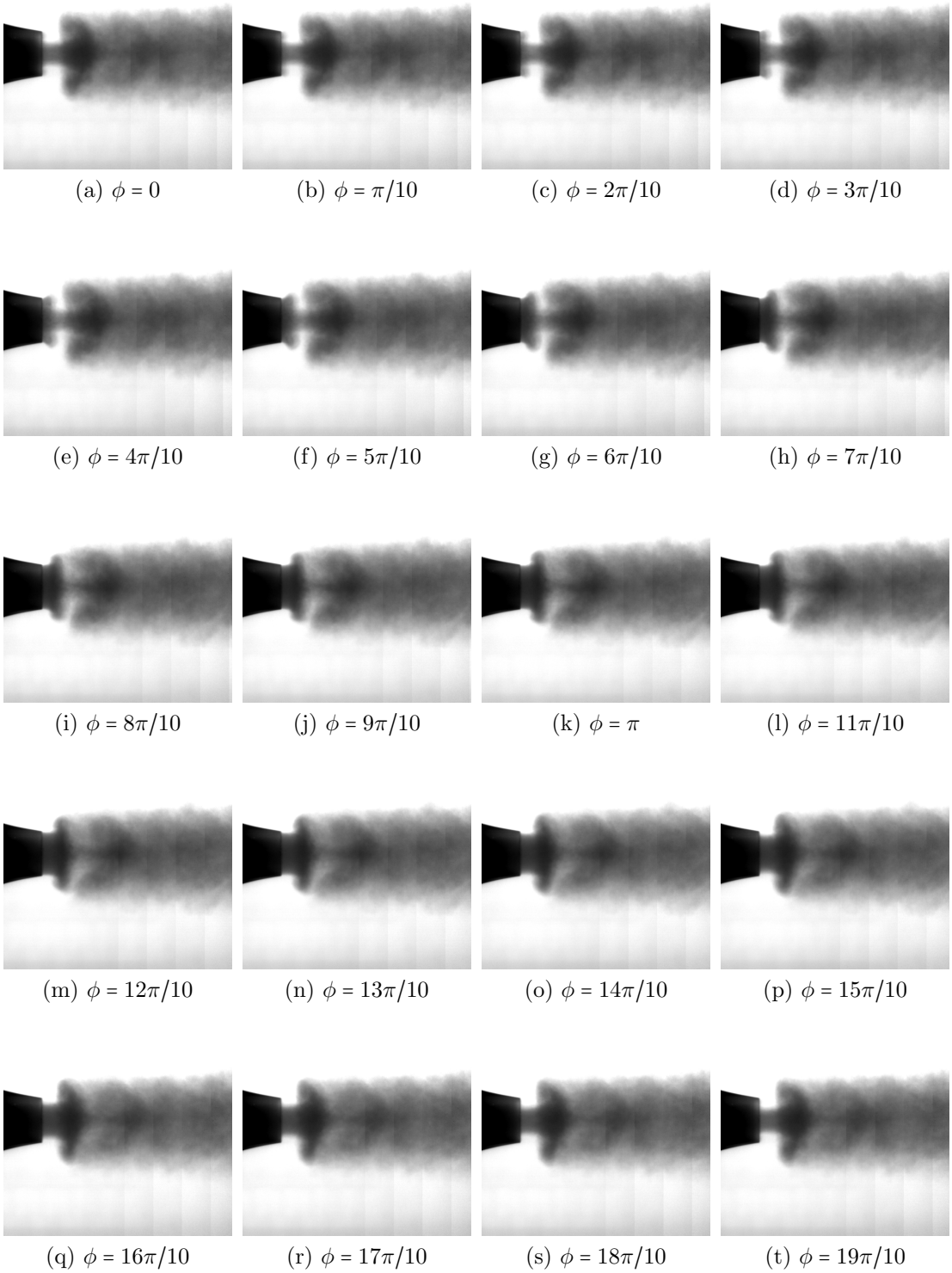

(a) $\phi = 0$ (b) $\phi = \pi/10$ (c) $\phi = 2\pi/10$ (d) $\phi = 3\pi/10$

(e) $\phi = 4\pi/10$ (f) $\phi = 5\pi/10$ (g) $\phi = 6\pi/10$ (h) $\phi = 7\pi/10$

(i) $\phi = 8\pi/10$ (j) $\phi = 9\pi/10$ (k) $\phi = \pi$ (l) $\phi = 11\pi/10$

(m) $\phi = 12\pi/10$ (n) $\phi = 13\pi/10$ (o) $\phi = 14\pi/10$ (p) $\phi = 15\pi/10$

(q) $\phi = 16\pi/10$ (r) $\phi = 17\pi/10$ (s) $\phi = 18\pi/10$ (t) $\phi = 19\pi/10$

Figure F.5: Phase-averaged dye visualization with $T = 1300$ and $\tau = 10$ s. This yielded a normalized formation time of $\hat{t}/F = 0.70$ and a normalized Froude efficiency of $\eta/\eta_0 = 0.78$. Each phase-averaged frame consists of 7–8 frames stacked and are 0.008 seconds apart (recorded at 125 Hz).

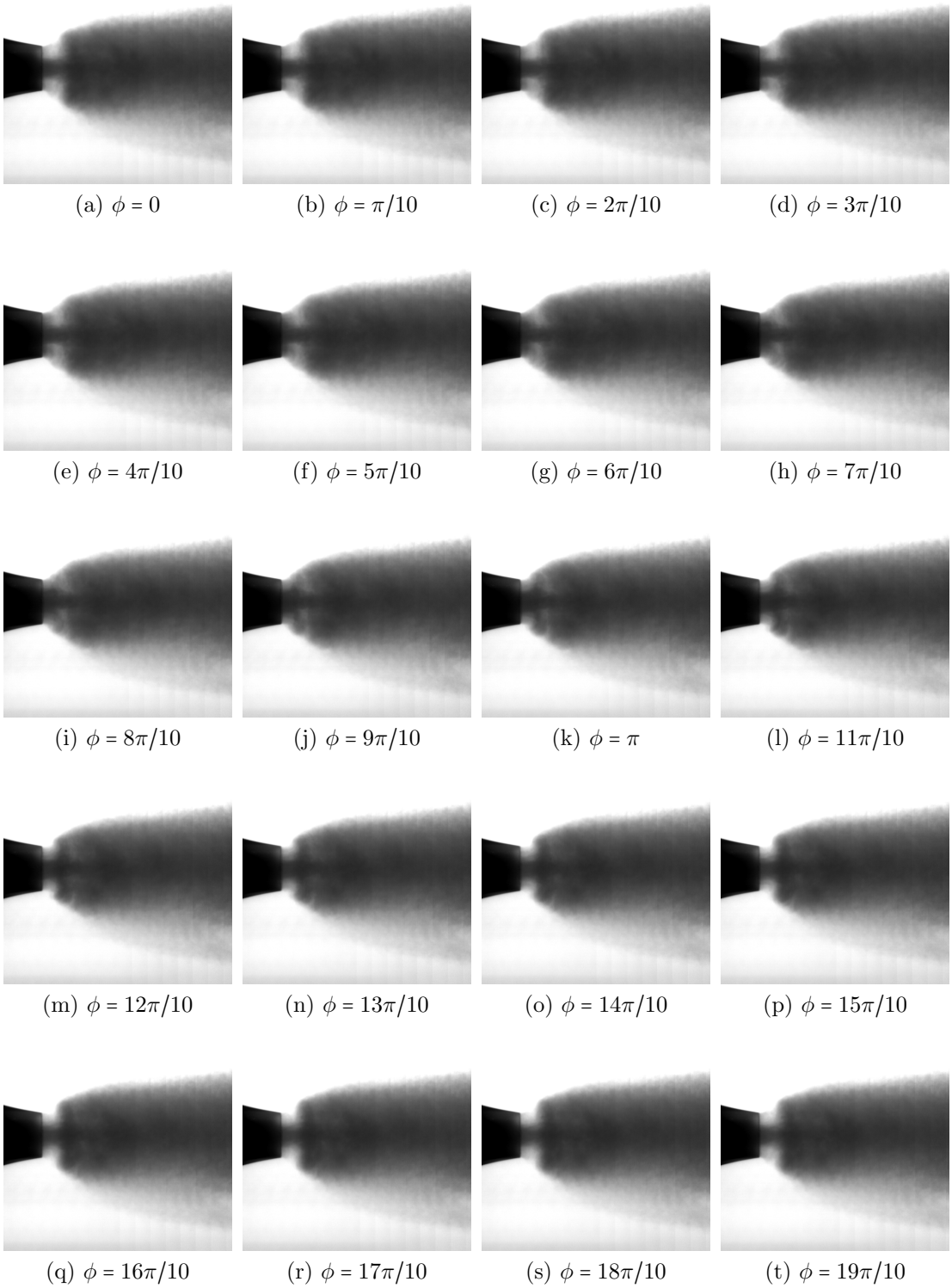

(a) $\phi = 0$ (b) $\phi = \pi/10$ (c) $\phi = 2\pi/10$ (d) $\phi = 3\pi/10$

(e) $\phi = 4\pi/10$ (f) $\phi = 5\pi/10$ (g) $\phi = 6\pi/10$ (h) $\phi = 7\pi/10$

(i) $\phi = 8\pi/10$ (j) $\phi = 9\pi/10$ (k) $\phi = \pi$ (l) $\phi = 11\pi/10$

(m) $\phi = 12\pi/10$ (n) $\phi = 13\pi/10$ (o) $\phi = 14\pi/10$ (p) $\phi = 15\pi/10$

(q) $\phi = 16\pi/10$ (r) $\phi = 17\pi/10$ (s) $\phi = 18\pi/10$ (t) $\phi = 19\pi/10$

Figure F.6: Phase-averaged dye visualization with $T = 1300$ and $\tau = 12$ s. This yielded a normalized formation time of $\hat{t}/F = 0.43$ and a normalized Froude efficiency of $\eta/\eta_0 = 0.69$. Each phase-averaged frame consists of 13–14 frames stacked and are 0.008 seconds apart (recorded at 125 Hz).

Figure F.7: Averaged dye visualization for T = 1500 and τ = 0 s. Phase-averaged frame consists of 53 frames are stacked.

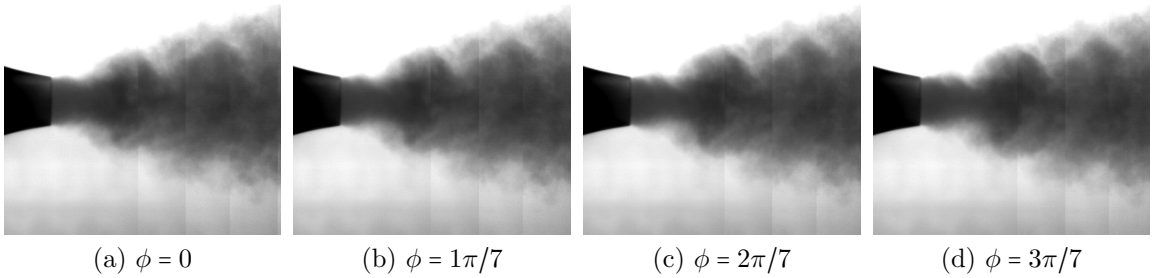

(a) $\phi = 0$ (b) $\phi = 1\pi/7$ (c) $\phi = 2\pi/7$ (d) $\phi = 3\pi/7$

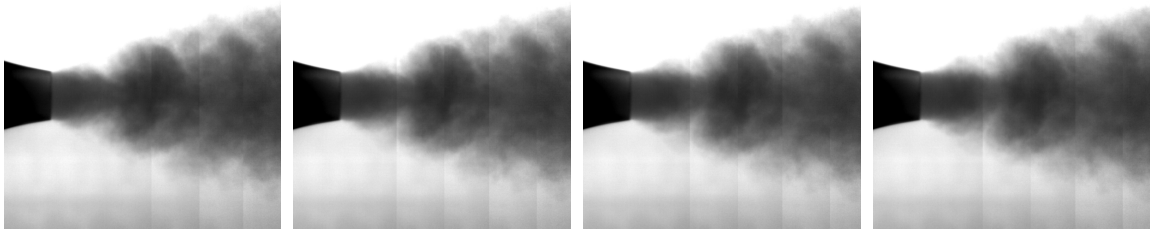

(e) $\phi = 4\pi/7$ (f) $\phi = 5\pi/7$ (g) $\phi = 6\pi/7$ (h) $\phi = \pi$

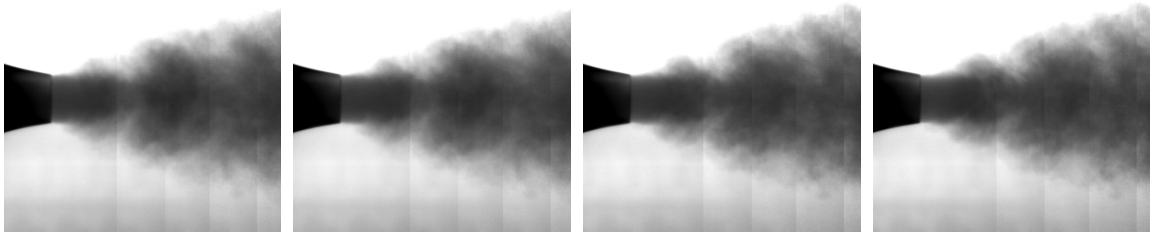

(i) $\phi = 8\pi/7$ (j) $\phi = 9\pi/7$ (k) $\phi = 10\pi/7$ (l) $\phi = 11\pi/7$

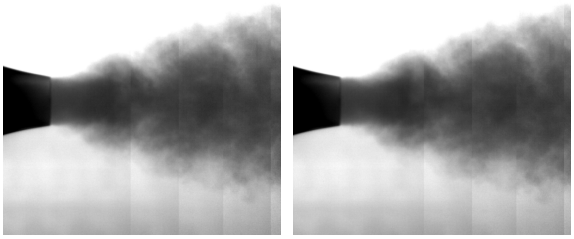

(m) $\phi = 12\pi/7$ (n) $\phi = 13\pi/7$

Figure F.8: Phase-averaged dye visualization with $T = 1500$ and $\tau = 8$ s. This yielded a normalized formation time of $\hat{t}/F = 1.33$ and a normalized Froude efficiency of $\eta/\eta_0 = 1.04$. Each phase-averaged frame consists of 6–7 frames stacked and are 0.008 seconds apart (recorded at 125 Hz).

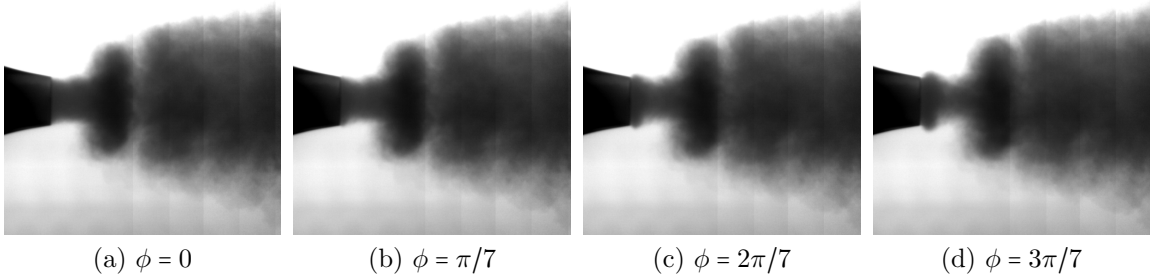

(a) $\phi = 0$ (b) $\phi = \pi/7$ (c) $\phi = 2\pi/7$ (d) $\phi = 3\pi/7$

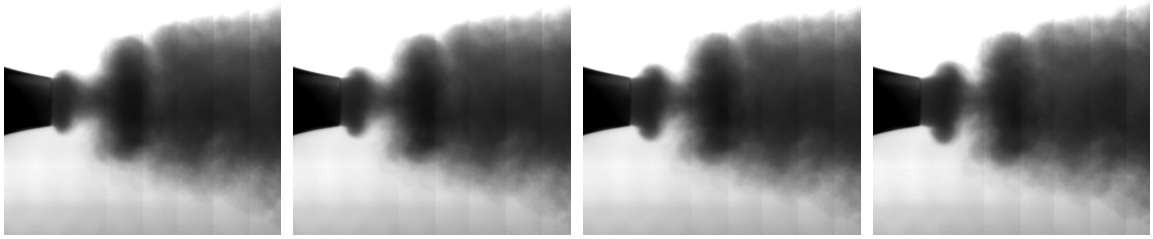

(e) $\phi = 4\pi/7$ (f) $\phi = 5\pi/7$ (g) $\phi = 6\pi/7$ (h) $\phi = \pi$

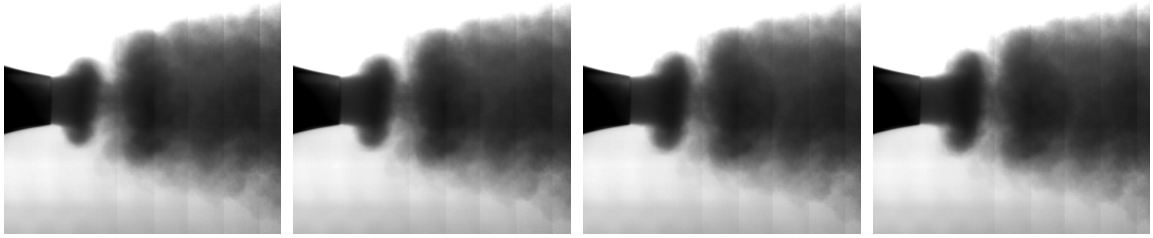

(i) $\phi = 8\pi/7$ (j) $\phi = 9\pi/7$ (k) $\phi = 10\pi/7$ (l) $\phi = 11\pi/7$

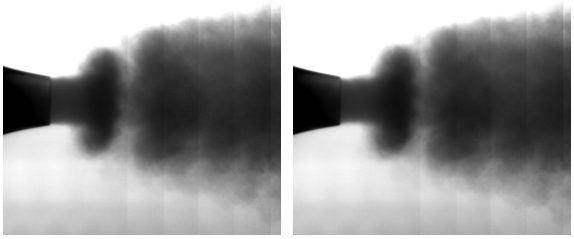

(m) $\phi = 12\pi/7$ (n) $\phi = 13\pi/7$

Figure F.9: Phase-averaged dye visualization with $T = 1500$ and $\tau = 9$ s. This yielded a normalized formation time of $\hat{t}/F = 1.09$ and a normalized Froude efficiency of $\eta/\eta_0 = 1.14$. Each phase-averaged frame consists of 8–9 frames stacked and are 0.008 seconds apart (recorded at 125 Hz).

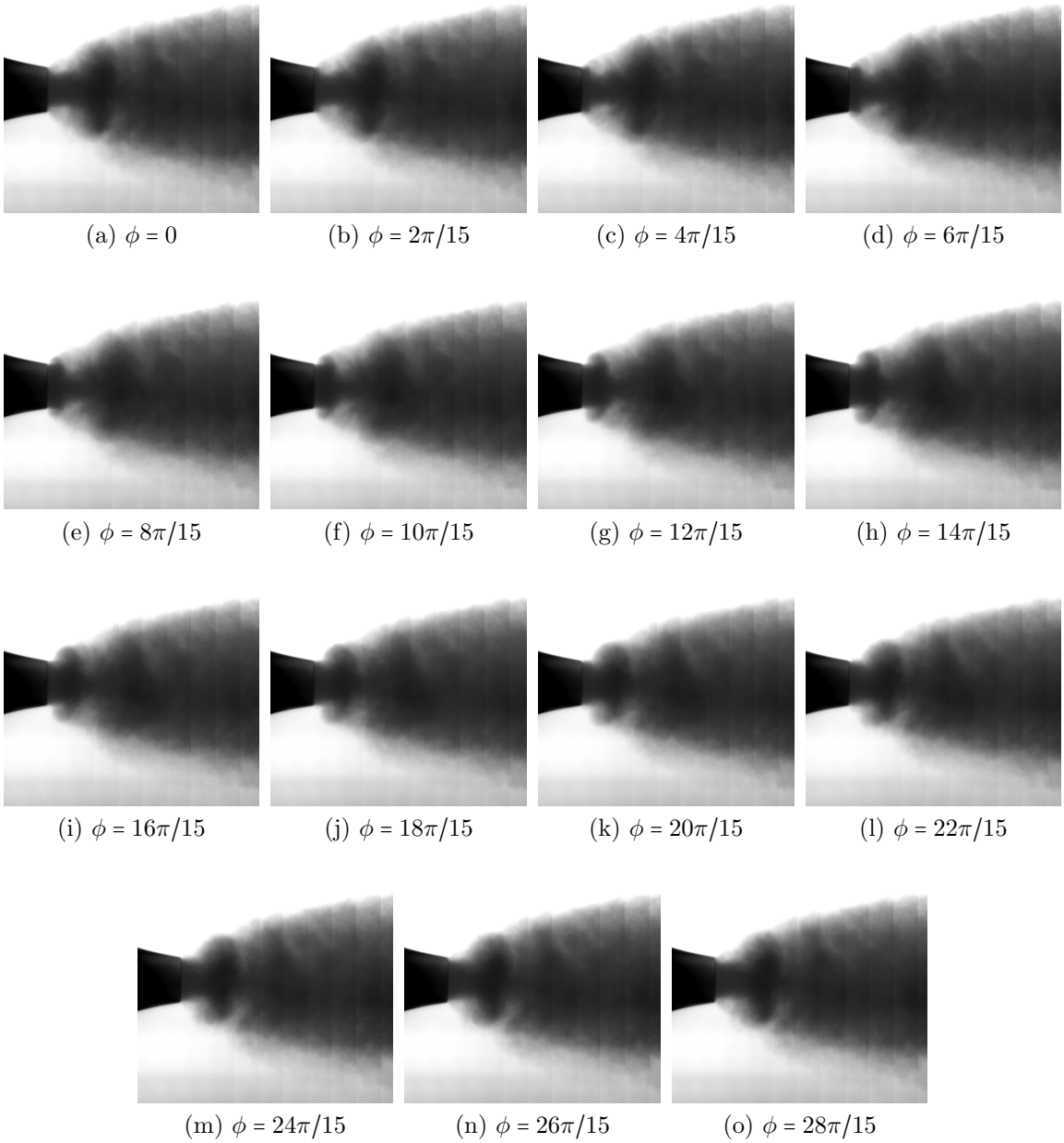

(a) $\phi = 0$ (b) $\phi = 2\pi/15$ (c) $\phi = 4\pi/15$ (d) $\phi = 6\pi/15$

(e) $\phi = 8\pi/15$ (f) $\phi = 10\pi/15$ (g) $\phi = 12\pi/15$ (h) $\phi = 14\pi/15$

(i) $\phi = 16\pi/15$ (j) $\phi = 18\pi/15$ (k) $\phi = 20\pi/15$ (l) $\phi = 22\pi/15$

(m) $\phi = 24\pi/15$ (n) $\phi = 26\pi/15$ (o) $\phi = 28\pi/15$

Figure F.10: Phase-averaged dye visualization with $T = 1500$ and $\tau = 10$ s. This yielded a normalized formation time of $\hat{t}/F = 0.89$ and a normalized Froude efficiency of $\eta/\eta_0 = 1.07$. Each phase-averaged frame consists of 11–12 frames stacked and are 0.008 seconds apart (recorded at 125 Hz).

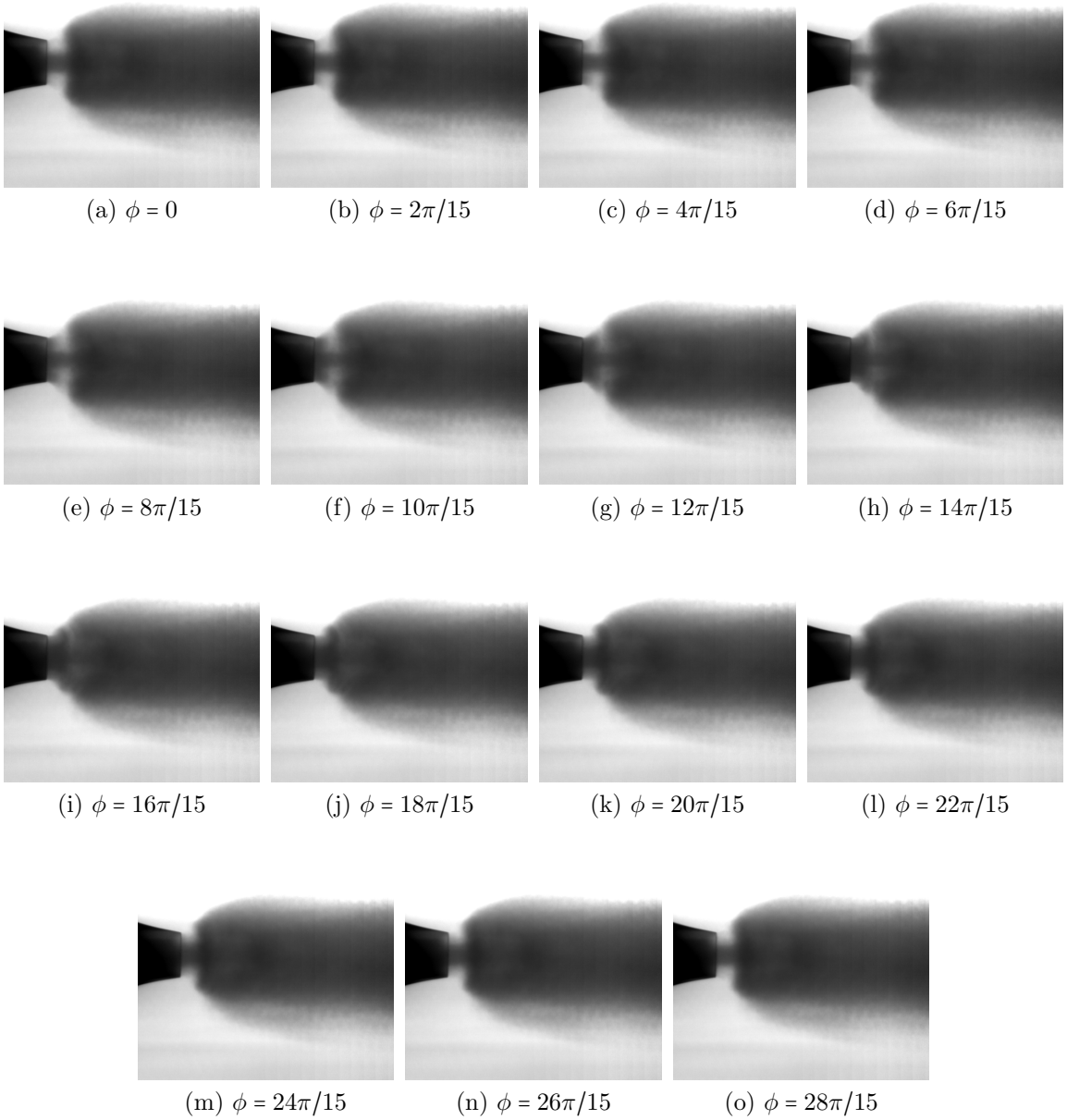

(a) $\phi = 0$ (b) $\phi = 2\pi/15$ (c) $\phi = 4\pi/15$ (d) $\phi = 6\pi/15$

(e) $\phi = 8\pi/15$ (f) $\phi = 10\pi/15$ (g) $\phi = 12\pi/15$ (h) $\phi = 14\pi/15$

(i) $\phi = 16\pi/15$ (j) $\phi = 18\pi/15$ (k) $\phi = 20\pi/15$ (l) $\phi = 22\pi/15$

(m) $\phi = 24\pi/15$ (n) $\phi = 26\pi/15$ (o) $\phi = 28\pi/15$

Figure F.11: Phase-averaged dye visualization with $T = 1500$ and $\tau = 14$ s. This yielded a normalized formation time of $\hat{t}/F = 0.31$ and a normalized Froude efficiency of $\eta/\eta_0 = 0.72$. Each phase-averaged frame consists of 19–20 frames stacked and are 0.008 seconds apart (recorded at 125 Hz).

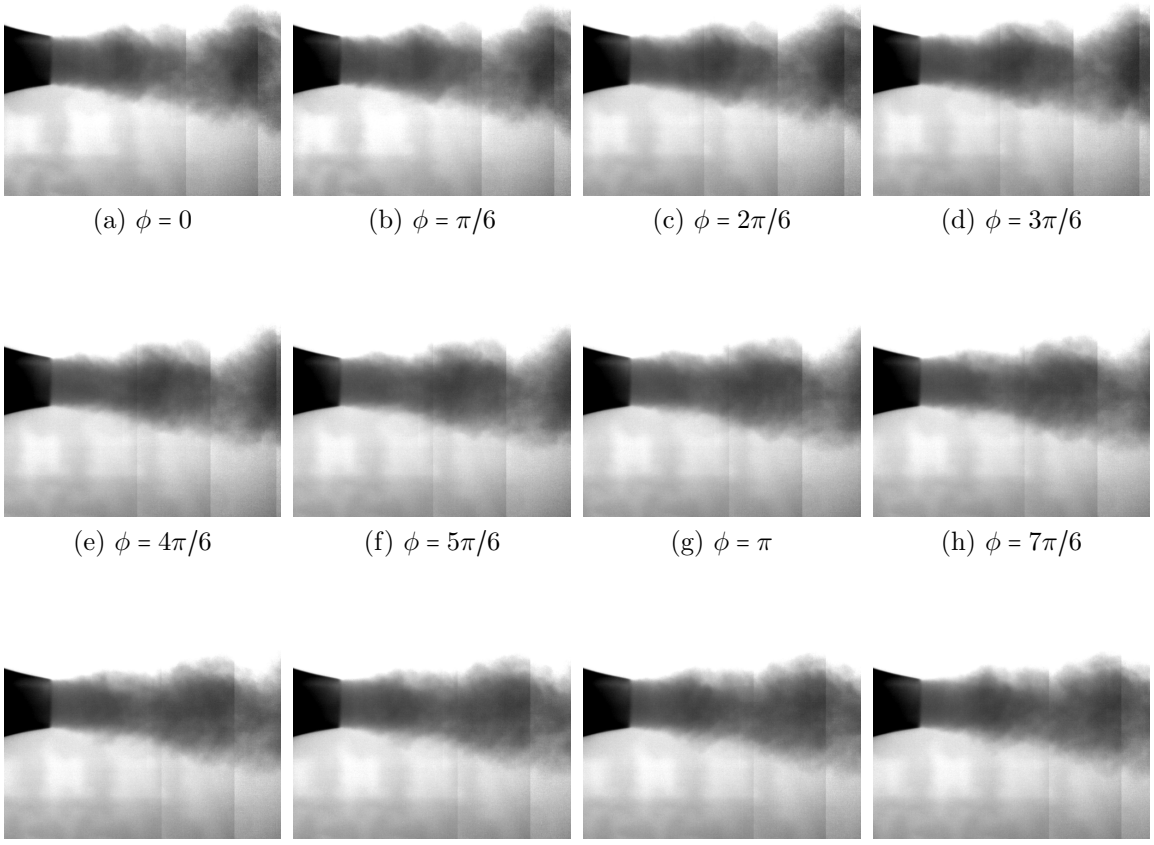

(a) $\phi = 0$ (b) $\phi = \pi/6$ (c) $\phi = 2\pi/6$ (d) $\phi = 3\pi/6$

(e) $\phi = 4\pi/6$ (f) $\phi = 5\pi/6$ (g) $\phi = \pi$ (h) $\phi = 7\pi/6$

(i) $\phi = 8\pi/6$ (j) $\phi = 9\pi/6$ (k) $\phi = 10\pi/6$ (l) $\phi = 11\pi/6$

Figure F.12: Phase-averaged dye visualization with $T = 1700$ and $\tau = 5$ s. This yielded a normalized formation time of $\hat{t}/F = 1.77$. Each phase-averaged frame consists of 3–4 frames stacked and are 0.008 seconds apart (recorded at 125 Hz).

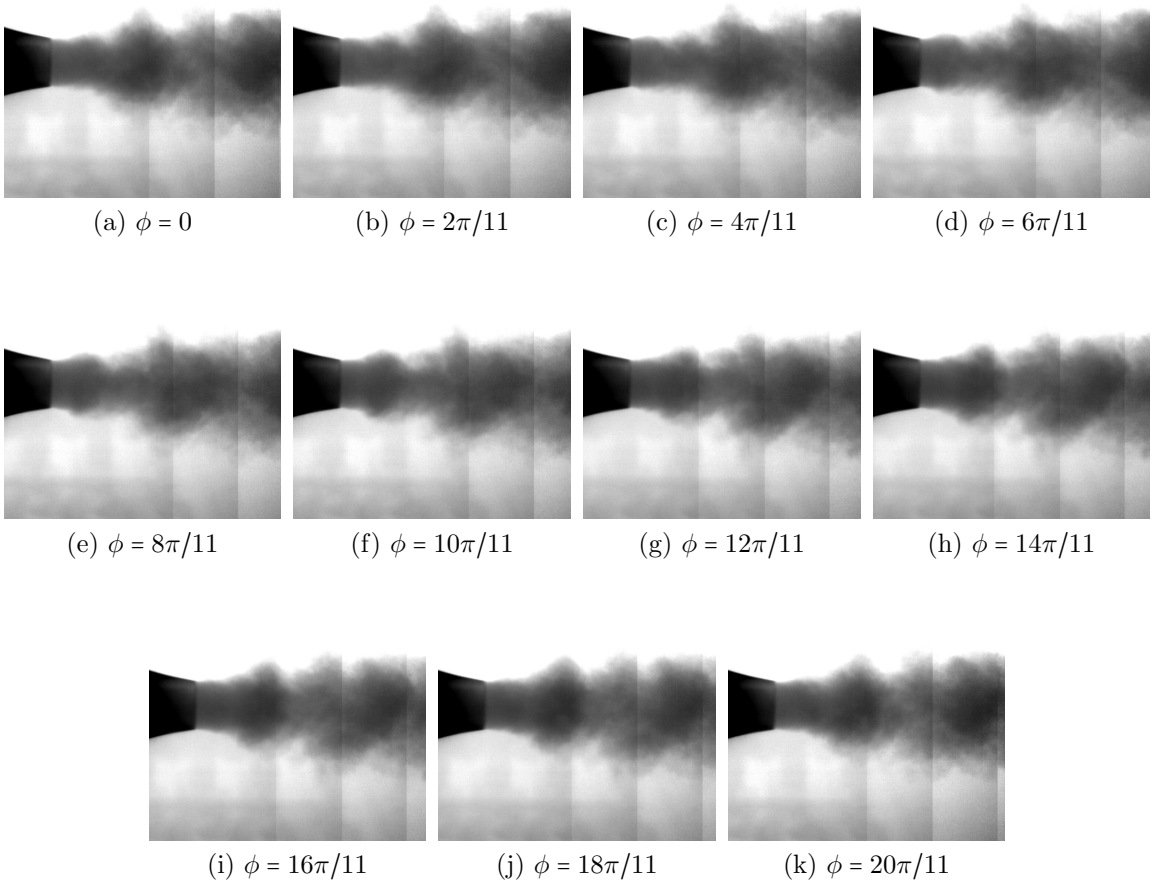

(a) $\phi = 0$ (b) $\phi = 2\pi/11$ (c) $\phi = 4\pi/11$ (d) $\phi = 6\pi/11$

(e) $\phi = 8\pi/11$ (f) $\phi = 10\pi/11$ (g) $\phi = 12\pi/11$ (h) $\phi = 14\pi/11$

(i) $\phi = 16\pi/11$ (j) $\phi = 18\pi/11$ (k) $\phi = 20\pi/11$

Figure F.13: Phase-averaged dye visualization with $T = 1700$ and $\tau = 6$ s. This yielded a normalized formation time of $\hat{t}/F = 1.59$. Each phase-averaged frame consists of 4–5 frames stacked and are 0.008 seconds apart (recorded at 125 Hz).

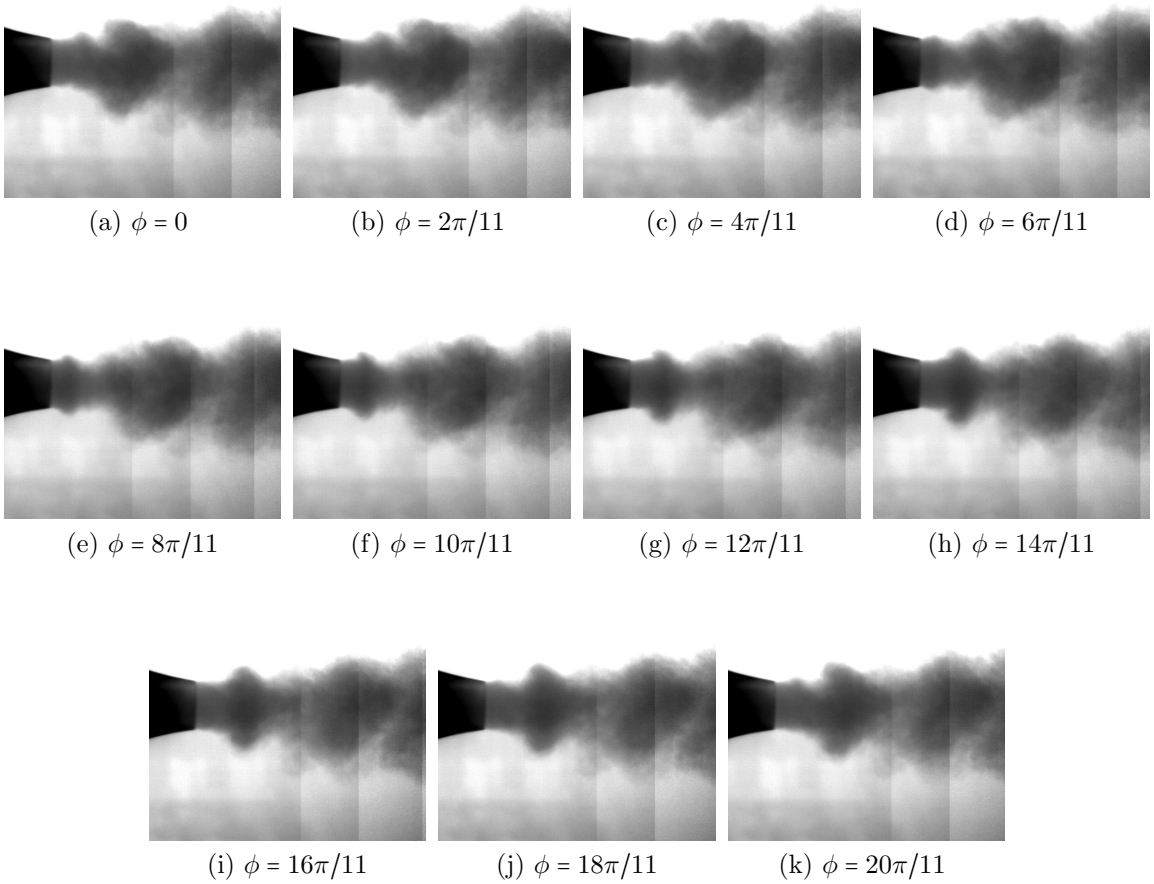

(a) $\phi = 0$ (b) $\phi = 2\pi/11$ (c) $\phi = 4\pi/11$ (d) $\phi = 6\pi/11$

(e) $\phi = 8\pi/11$ (f) $\phi = 10\pi/11$ (g) $\phi = 12\pi/11$ (h) $\phi = 14\pi/11$

(i) $\phi = 16\pi/11$ (j) $\phi = 18\pi/11$ (k) $\phi = 20\pi/11$

Figure F.14: Phase-averaged dye visualization with $T = 1700$ and $\tau = 7$ s. This yielded a normalized formation time of $\hat{t}/F = 1.48$. Each phase-averaged frame consists of 4–5 frames stacked and are 0.008 seconds apart (recorded at 125 Hz).

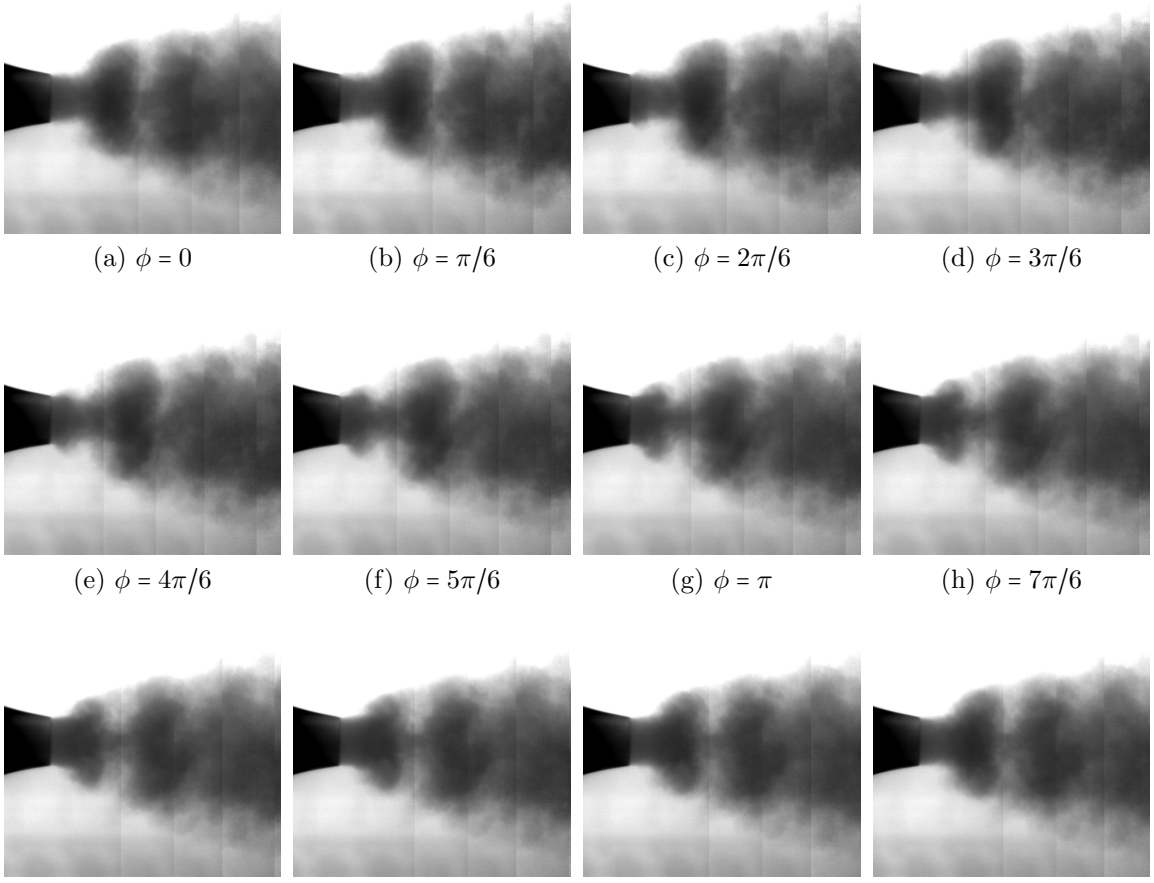

(a) $\phi = 0$ (b) $\phi = \pi/6$ (c) $\phi = 2\pi/6$ (d) $\phi = 3\pi/6$

(e) $\phi = 4\pi/6$ (f) $\phi = 5\pi/6$ (g) $\phi = \pi$ (h) $\phi = 7\pi/6$

(i) $\phi = 8\pi/6$ (j) $\phi = 9\pi/6$ (k) $\phi = 10\pi/6$ (l) $\phi = 11\pi/6$

Figure F.15: Phase-averaged dye visualization with $T = 1700$ and $\tau = 10$ s. This yielded a normalized formation time of $\hat{t}/F = 0.96$. Each phase-averaged frame consists of 5–6 frames stacked and are 0.008 seconds apart (recorded at 125 Hz).

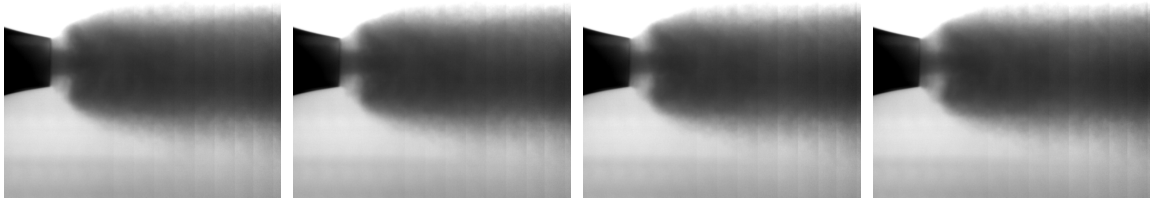

(a) $\phi = 0$ (b) $\phi = 2\pi/11$ (c) $\phi = 4\pi/11$ (d) $\phi = 6\pi/11$

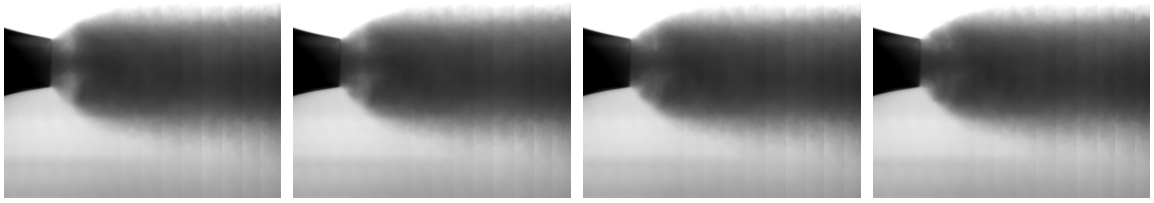

(e) $\phi = 8\pi/11$ (f) $\phi = 10\pi/11$ (g) $\phi = 12\pi/11$ (h) $\phi = 14\pi/11$

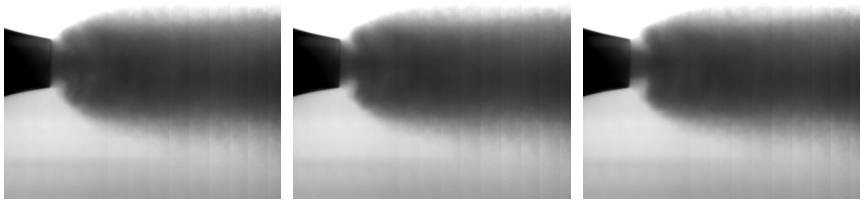

(i) $\phi = 16\pi/11$ (j) $\phi = 18\pi/11$ (k) $\phi = 20\pi/11$

Figure F.16: Phase-averaged dye visualization with $T = 1700$ and $\tau = 16$ s. This yielded a normalized formation time of $\hat{t}/F = 0.24$. Each phase-averaged frame consists of 14–15 frames stacked and are 0.008 seconds apart (recorded at 125 Hz).

Appendix G

Plots of Parameter Study Results

In this appendix, the choice of the plotting variables using in the present work (f vs. C_P) is considered via plotting a myriad of possible parameter combinations. To save space and declutter the pages, the axes ticks have been removed. This is reasonable as we are currently just considering relationships, rather than exact values. In particular, one is looking for plots that collapse the data well.

The data plotted is from figure 3.3(a) of S-4, M-4, and L-4 where $U_j = 0.2$ m s^{-1}. For nondimensionalizing the frequency, the Strouhal number and Wormersley number were both considered and are defined as

$$St' = \frac{fD_0}{U_j} \tag{G.1}$$

and

$$\alpha' = D_0\sqrt{\frac{f}{\nu}} \tag{G.2}$$

respectively. An additional form of the Strouhal number was considered, where the velocity used was the Moens-Korteweg wavespeed, and is defined as

$$St'_c = \frac{fD_0}{c}, \tag{G.3}$$

where c is the Moens-Korteweg wavespeed and $c = \sqrt{Eh/\rho D_0}$.

In general, the results plotted in figure G.1 show that the selected plotting variables of f versus C_P yield a good collapse of the data. Many of the other variable combinations tested and shown in figure G.1 do not yield as good of a collapse of the data. However, of note are the plots of α' versus the pressures non-dimensionalized by the bending stiffness parameters, P_t/K_P, $P_t/K_{P,\infty}$, P_d/K_P, and $P_d/K_{P,\infty}$. The lines appear to follow a nice trend, however the different nozzles do not identically overlap as they do with the f versus C_P plots. This is perhaps difficult to see at this scale, but one can make out that the markers (indicating different nozzles) are different at different points along the curve.

We can explore why these variables make such a seemingly nice collapse of the data by considering the formulation of α' and P_t/K_P. For ease in this derivation, let us consider that $P_t/K_P = \xi$, which yields:

$$\alpha' = D_0\sqrt{\frac{f}{\nu}}, \qquad \xi = \frac{P_t}{\frac{\pi^2 Eh^3}{6(1-\sigma^2)D_0 L_0^2}}. \tag{G.4}$$

Based on the plot of f versus P_t in figure G.1, let us make the assumption that $f \sim P_t$ such that $f \approx \gamma P_t$ where γ is a constant. Thus:

$$\alpha' = D_0\sqrt{\frac{\gamma P_t}{\nu}}, \tag{G.5}$$

$$\alpha' = D_0\sqrt{\frac{\gamma\xi\pi^2 Eh^3}{\nu 6\left(1-\sigma^2\right) D_0 L_0^2}}, \tag{G.6}$$

$$\frac{\alpha'}{D_0} = \sqrt{\frac{\gamma\xi\pi^2 Eh^3}{\nu 6\left(1-\sigma^2\right) D_0 L_0^2}}, \tag{G.7}$$

$$\frac{\alpha'^2}{D_0^2} = \frac{\gamma\xi\pi^2 Eh^3}{\nu 6\left(1-\sigma^2\right) D_0 L_0^2}. \tag{G.8}$$

$$\alpha'^2 = \frac{\gamma\pi^2 Eh^3}{\nu 6\left(1-\sigma^2\right)}\frac{D_0}{L_0^2}\xi \tag{G.9}$$

For all of the tubes tested, $\gamma\pi^2 Eh^3/\nu 6\left(1-\sigma^2\right)$ is constant and is replaced by $\aleph^2$ for convenience.

$$\alpha'^2 = \aleph^2 \frac{D_0}{L_0^2}\xi, \tag{G.10}$$

$$\alpha'^2 = \aleph^2 \frac{D_0^2}{L_0^2 D_0}\xi, \tag{G.11}$$

$$\alpha'^2 = \aleph^2 \left(\frac{L_0}{D_0}\right)^{-2} \frac{\xi}{D_0}, \tag{G.12}$$

$$\alpha' = \aleph \left(\frac{L_0}{D_0}\right)^{-1} \sqrt{\frac{\xi}{D_0}}, \tag{G.13}$$

and replacing ξ with the original variable yields

$$\alpha' = \aleph \left(\frac{L_0}{D_0}\right)^{-1} \sqrt{\frac{1}{D_0}}\sqrt{\frac{P_t}{K_P}}. \tag{G.14}$$

The same procedure for the other bending stiffness parameters yields

$$\alpha' = \aleph \left(\frac{L_0}{D_0}\right)^{-1} \sqrt{\frac{1}{D_0}}\sqrt{\frac{P_d}{K_P}}, \tag{G.15}$$

$$\alpha' = \aleph' \sqrt{\frac{1}{D_0}}\sqrt{\frac{P_t}{K_{P,\infty}}}, \tag{G.16}$$

$$\alpha' = \aleph' \sqrt{\frac{1}{D_0}}\sqrt{\frac{P_d}{K_{P,\infty}}}, \tag{G.17}$$

where $\aleph' = 4\aleph$. As P_t and P_d both span four orders of magnitude ($\mathcal{O}(10^0$–$10^4)$), they dominate in these expressions and simply yield

$$\begin{aligned} \alpha' &\sim \sqrt{P_t/K_P}, \qquad \alpha' \sim \sqrt{P_t/K_{P,\infty}}, \\ \alpha' &\sim \sqrt{P_d/K_P}, \qquad \alpha' \sim \sqrt{P_d/K_{P,\infty}}. \end{aligned} \tag{G.18}$$

Thus the seemingly good collapse of the data for α' versus the bending stiffness parameters is simply a result of the choice of nondimensional variables.

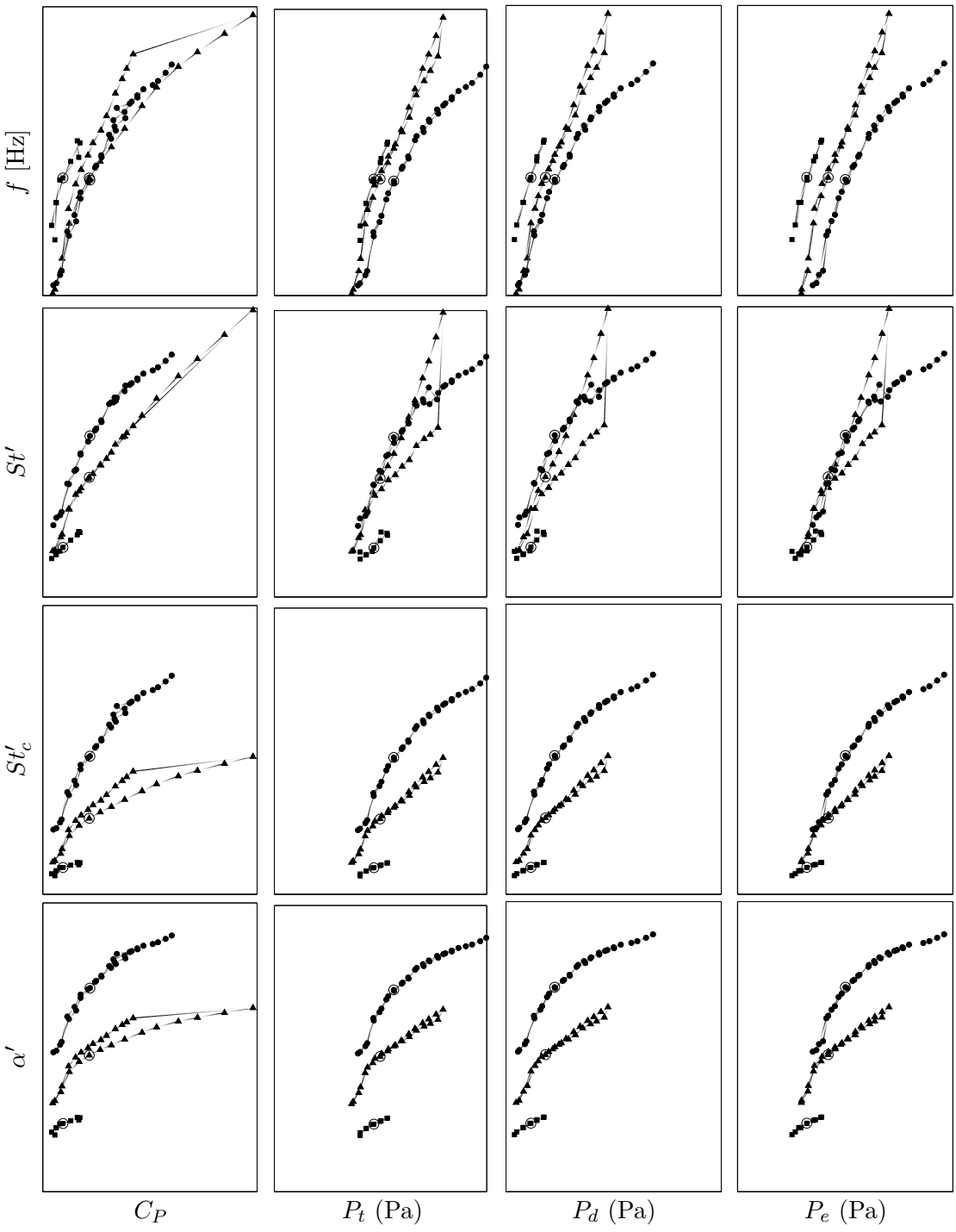

Figure G.1: Array of plots showing various relations between different expressions for the frequency of oscillation (on the vertical axis) and different independent variables (on the horizontal axis). Plot ticks and axis labels have been removed for clarity. The rows of the plot array correspond to the frequency expression denoted on the left-hand side of the plot array and the columns of the plot array correspond to the independent variable denoted at the bottom of each plot array column.

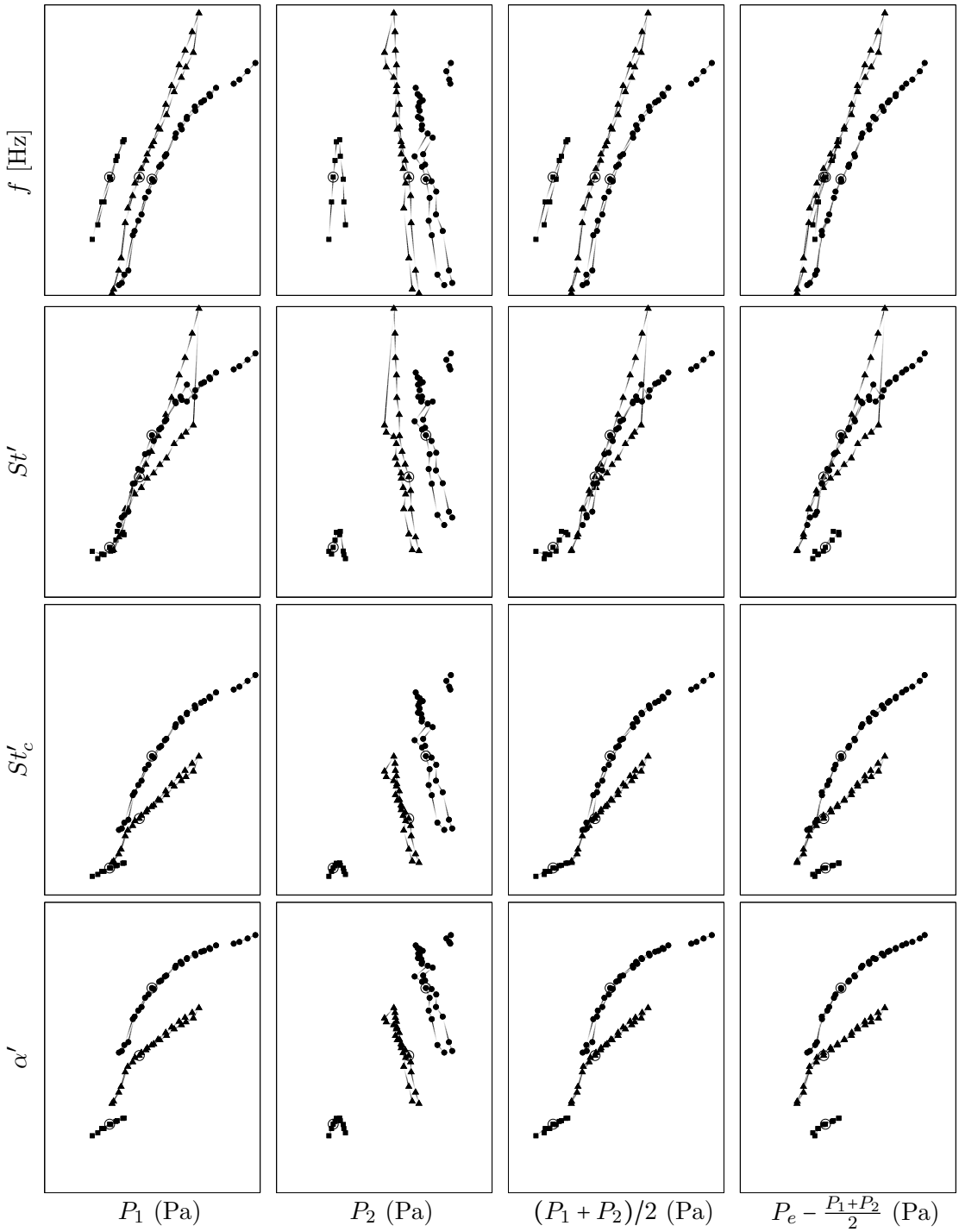

Figure G.1: Full caption available on page 161

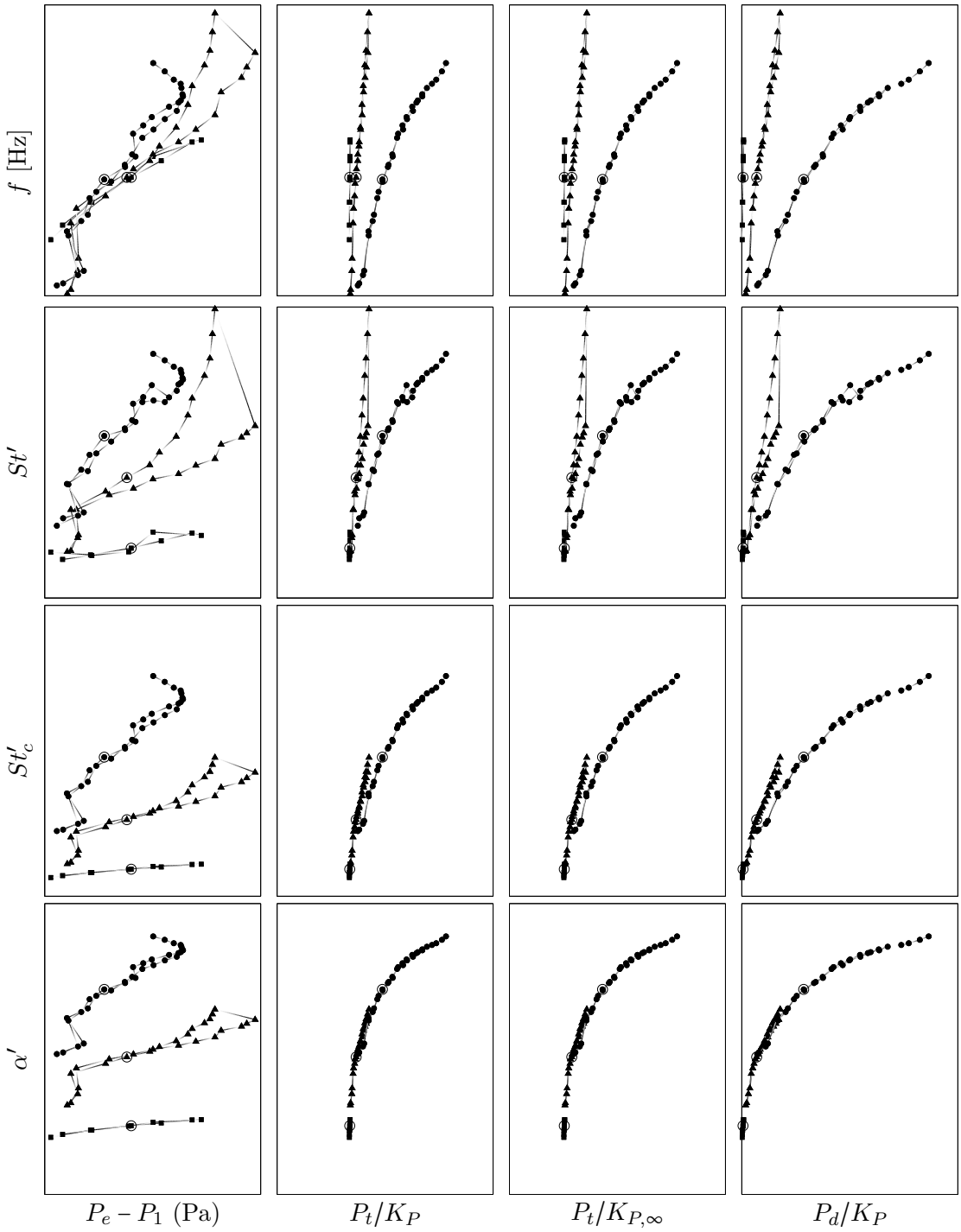

Figure G.1: Full caption available on page 161

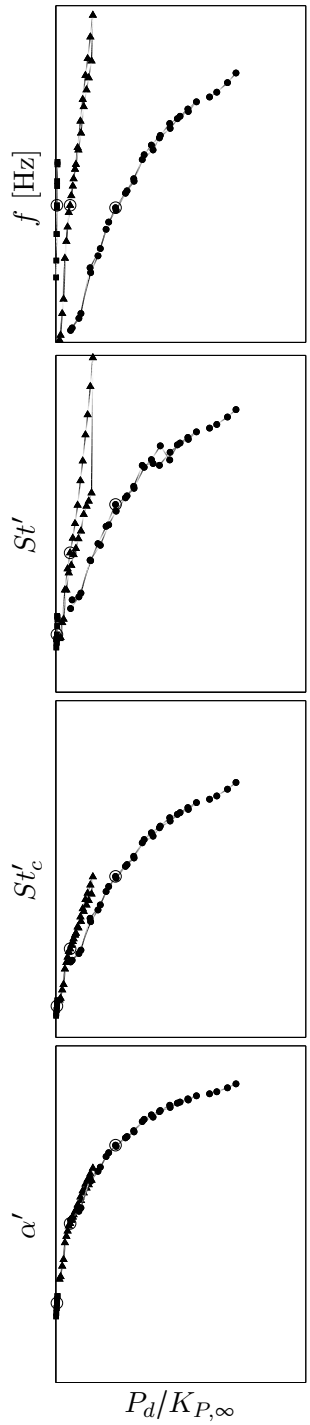

Figure G.1: Full caption available on page 161

Bibliography

Anderson, J. M. & Chhabra, N. K. 2002 Maneuvering and stability performance of a robotic tuna. *Integrative & Comparative Biology* **42**, 118–26.

Avrahami, I. & Gharib, M. 2008 Computational studies of resonance wave pumping in compliant tubes. *Journal of Fluid Mechanics* **608**, 139–60.

Ayers, J., Wilbur, C. & Olcott, C. 2000 Lamprey robots. In *Proceedings of the International Symposium on Aqua Biomechanisms*.

Bainbridge, R. 1961 Problems of fish locomotion. *Symposia of the Zoologica Society of London* **5**, 13–32.

Batdorf, S. B. 1947 A simplified method of elastic-stability analysis for thin cylindrical shells. *Tech. Rep.*. NACA Report 874.

Beckwith, T. G., Marangoni, R. D. & V, J. H. L. 2007 *Mechanical Measurements*. Pearson Prentice Hall.

Bertram, C. D. 1986 Unstable equilibrium behaviour in collapsible tubes. *Journal of Biomechanics* **19** (1), 61–69.

Bertram, C. D. 2003 *Flow Past Highly Compliant Boundaries and in Collapsible Tubes*, chap. Experimental studies of collapsible tubes, pp. 51–65. Springer.

Bertram, C. D. & Castles, R. J. 1999 Flow limitation in uniform thick-walled collapsible tubes. *Journal of Fluids and Structures* **13**, 399–418.

Bertram, C. D., Diaz de Tuesta, G. & Nugent, A. H. 2001 Laser-doppler measurement of velocities just downstram of a collapsible tube during flow-induced oscillations. *Journal of Biomechanical Engineering* **123**, 493–9.

Bertram, C. D. & Godbole, S. A. 1995 Area and pressure profiles for collapsibe-tube oscillations of three types. *Journal of Fluids and Structures* **9**, 257–77.

Bertram, C. D. & Nugent, A. H. 2005 The flow field downstream of an oscillating collapsed tube. *Journal of Biomechanical Engineering* **127**, 39–45.

Bertram, C. D. & Pedley, T. J. 1982 A mathematical model of unsteady collapsibe tube behaviour. *Journal of Biomechanics* **15**, 39–50.

Bertram, C. D., Raymond, C. J. & Pedley, T. J. 1990 Mapping of instabilities for flow through collapsed tubes of differing length. *Journal of Fluids and Structures* **4**, 125–153.

Bertram, C. D., Raymond, C. J. & Pedley, T. J. 1991 Application of nonlinear dynamics and concepts to the analysis of self-excited oscillations of a collapsible tube conveying a fluid. *Journal of Fluids and Structures* **5**, 391–426.

Bertram, C. D., Sheppeard, M. D. & Jensen, O. E. 1994 Prediction and measurement of the area-distance profile of collapsed tubes during self-excited oscillation. *Journal of Fluids and Structures* **8**, 637–60.

Bertram, C. D., Truong, N. K. & Hall, S. D. 2008 Piv measurement of the flow field just downstream of an oscillating collapsible tube. *Journal of Biomechanical Engineering* **130**, 061011.

Bertram, C. D. & Tscherry, J. 2006 The onset of flow-rate limitation and flow-induced oscillations in collapsible tubes. *Journal of Fluids and Structures* **22**, 1029–45.

Brackenbury, J. 2001 The vortex wake of the free-swimming larva and pupa of *Culex pipiens* (diptera). *Journal of Experimental Biology* **204**, 1855–67.

Brackenbury, J. 2002 Kinematics and hydrodynamics of an invertebrate undulatory swimmer: the damsel-fly larva. *Journal of Experimental Biology* **205**, 627–39.

Brackenbury, J. 2003 Escape manoeuvres in damsel-fly llarva: kinematics and dynamics. *Journal of Experimental Biology* **206**, 389–97.

Brackenbury, J. 2004 Kinematics and hydrodynamics of swimming in the mayfly larva. *Journal of Experimental Biology* **207**, 913–22.

Brecher, G. A. 1956 *Venous Return*. Grune & Stratton.

Brodsky, A. K. 1991 Vortex formation in the thethered flight of the peacock butterfly *inachis io* l. (leipidoptera, nymphalidae) and some aspects of insect flight evolution. *Journal of Expeirmental Biology* **161**, 77–95.

Cancelli, C. & Pedley, T. J. 1985 A separated-flow model for collapsible-tube oscillations. *Journal of Fluid Mechanics* **157**, 375–404.

Choutapalli, I. M. 2007 *An Experimental Study of a Pulsed Jet Ejector*. PhD Thesis, Florida State University.

Conrad, W. A. 1969 Pressure-flow relationships in collapsible tubes. *IEEE Transactions on Bio-medical Engineering* **BME-16** (4), 284–295.

Dabiri, J. O. 2009 Optimal vortex formation as a unifying principle in biological propulsion. *Annual Review of Fluid Mechanics* **41**, 17–33.

Dabiri, J. O. & Gharib, M. 2004*a* Delay of vortex ring pinchoff by an imposed bulk counterflow. *Physics of Fluids* **16**, L28–30.

Dabiri, J. O. & Gharib, M. 2004*b* Fluid entrainment by isolated vortex rings. *Journal of Fluid Mechanics* **511**, 311–331.

Dickinson, M. H. 1996 Unsteady mechanisms of force generation in aquatic and aerial locomotion. *American Zoologist* **36** (6), 537–54.

Ellington, C. P. 1978 *Comparative Physiology: Water, Ions and Fluid Mechanics*, chap. The aerodynamics of normal hovering flight: three approaches, pp. 327–45. Cambridge University Press.

Elsinga, G. E., Scarano, F., Wieneke, B. & van Oudheusden, B. W. 2006 Tomographic particle image velocimetry. *Experiments in Fluids* **41**, 933–47.

Finio, B. M. & Wood, R. J. 2012 Open-loop roll, pitch and yaw torques for a robotic bee. In *2012 IEEE/RSJ International Conference on Intelligent Robots and Systems (IROS)*.

Finley, T. J. & Mohseni, K. 2004 Micro pulsatile jets for thrust optimization. In *Proceedings of IMECE2004, 2004 ASME International Mechanical Engineering Congress and Exposition*.

Fung, Y. C. 1997 *Biomechanics: Circulation*. Springer.

Gadre, A., Maczka, D., Spinello, D., McCarter, B., Stilwell, D., Neu, W., Roan, M. & Hennage, J. 2008 Cooperative localization of an acoustic source using towed hydrophone arrays. In *Autonomous Underwater Vehicles, 2008. AUV 2008. IEEE/OES*, pp. 1–8.

Gharib, M., Rambod, E. & Shariff, K. 1998 A universal time scale for vortex ring formation. *Journal of Fluid Mechanics* **360**, 121–140.

Glezer, A. & Amitay, M. 2002 Synthetic jets. *Annual Review of Fluid Mechanics* **34**, 503–29.

Green, G. 1835 Researches on the vibration of pendulums in fluid media. *Transactions of the Royal Society of Edinburgh* **13** (1), 54–62.

Hayashi, S., Hayase, T. & Kawamura, H. 1998 Numerical analysis for stability and self-excited oscillation in collapsible tube flow. *Journal of Biomechanical Engineering* **120**, 468–75.

Hedenström, A., Johansson, L. C., Wolf, M., von Busse, R., Winter, Y. & Spedding, G. 2007 Bat flight generates complex aerodynamics tracks. *Science* **316**, 894–7.

Heil, M. & Boyle, J. 2010 Self-excited oscillations in three-dimensional collapsible tubes: simulating their onset and large-amplitude oscillations. *Journal of Fluid Mechanics* **652**, 405–26.

Heil, M. & Hazel, A. L. 2011 Fluid-structure interaction in internal physiological flows. *Annual Review of Fluid Mechanics* **43**, 141–162.

Heil, M. & Jensen, O. E. 2003 *Flow Past Highly Compliant Boundaries and in Collapsible Tubes*, chap. Flows in deformable tubes and channels: theoretical models and biological applications, pp. 15–49. Springer.

Heil, M. & Waters, S. L. 2006 Transverse flows in rapidly oscillating elastic cylindrical shells. *Journal of Fluid Mechanics* **547**, 185–214.

Heil, M. & Waters, S. L. 2008 How rapidly oscillating collapsible tubes extract energy from a viscous mean flow. *Journal of Fluid Mechanics* **601**, 199–227.

Hickerson, A. I., Rinderknecht, D. & Gharib, M. 2005 Experimental study of the behavior of a valveless impedance pump. *Experiments in Fluids* **38**, 534–40.

Ho, C.-M. & Gutmark, E. 1987 Vortex induction and mass entrainment in a small-aspect-ratio elliptic jet. *Journal of Fluid Mechanics* **179**, 383–405.

Holt, J. P. 1941 The collapse factor in the measurement of venous pressure, the flow of fluid through collapsible tubes. *American Journal of Physiology* **134**, 292–9.

Hu, H. 2006 Biologically inspired design of autonomous robotic fish at essex. In *Proceedings of the IEEE SMC UK-RI Chapter Conference 2006 on Advances in Cybernetic Systems*.

Ichiklzaki, T. & Yamamoto, I. 2007 Development of robotic fish with various swimming functions. In *Symposium on Underwater Technology and Workshop on Scientific Use of Submarine Cables and Related Technologies*.

Jensen, O. E. & Heil, M. 2003 High-frequency self-excited oscillations in a collapsible-channel flow. *Journal of Fluid Mechanics* **481**, 235–268.

Johansson, L. C. & Lauder, G. V. 2004 Hydrodynamics of surface swimming in leopard frogs (*Rana pipiens*). *Journal of Experimental Biology* **207**, 3945–58.

Johansson, L. C. & Norberg, R. A. 2003 Delta-wing function of webbed feet gives hydrodynamic lift for swimming propulsion in birds. *Nature* **424**, 65–68.

Kececioglu, I., Mcclurken, M. E., Kamm, R. D. & Shapiro, A. H. 1981 Steady, supercritical flow in collapsible tubes. part 1. experimental observations. *Journal of Fluid Mechanics* **109**, 367–389.

Knowlton, F. P. & Starling, E. H. 1912 The influence of variations in termperature and blood-pressure on the performance of the isolated mammalian heart. *Journal of Physiology* **44** (3), 206–19.

Kounanis, K. & Mathioulakis, D. S. 1999 Experimental flow study wiwith a self oscillating collapsible tube. *Journal of Fluids and Structures* **13**, 61–73.

Krieg, M., Coley, C., Hart, C. & Mohseni, K. 2005 Synthetic jet thrust optimization for application in underwater vehicles. In *International Symposium on Unmanned Untethered Submersible Technology (UUST)*.

Krieg, M. & Mohseni, K. 2008 Thrust characterization of a bioinspired vortex ring thruster for locomotion of underwater robots. *IEEE Journal of Oceanic Engineering* **33** (2), 123–32.

Krieg, M. & Mohseni, K. 2010 Dynamic modeling and control of biologically inspired vortex ring thrusters for underwater robot locomotion. *IEEE Transactions on Robotics* **26** (3), 542–54.

Krieg, M. & Mohseni, K. 2013 Modelling circulation, impulse and kinetic energy of starting jets with non-zero radial velocity. *Journal of Fluid Mechanics* **719**, 488–526.

Krishnan, G. & Mohseni, K. 2009*a* Axisymmetric synthetic jets: An experimental and theoretical examination. *AIAA Journal* **47** (10), 2273–83.

Krishnan, G. & Mohseni, K. 2009*b* An experimental and analytical investigation of rectangular synthetic jets. *Journal of Fluids Engineering* **131**, 121101.

Krueger, P. S. 2001 *The significance of vortex ring formation and nozzle exit overpressure to pulsatile jet propulsion*. PhD Thesis, California Institute of Technology.

Krueger, P. S., Dabiri, J. O. & Gharib, M. 2003 Vortex ring pinchoff in the presence of simultaneously initiated uniform background co-flow. *Physics of Fluids* **15** (7), L49–L52.

Krueger, P. S., Dabiri, J. O. & Gharib, M. 2006 The formation number of vortex rings formed in uniform background co-flow. *Journal of Fluid Mechanics* **556**, 147–166.

Krueger, P. S. & Gharib, M. 2005 Thrust augmentation and vortex ring evolution in a fully-pulsed jet. *AIAA Journal* **43** (4), 792–801.

Krueger, P. S., Moslemi, A. A., Nichols, J. T., Bartol, I. K. & Stewart, W. J. 2008 Vortex rings in bio-inspired and biological jet propulsion. *Advances in Science and Technology* **58**, 237–46.

Liepmann, D. & Gharib, M. 1992 The role of streamwise vorticity in the near-field entrainment of round jets. *Journal of Fluid Mechanics* **245**, 643–68.

Lighthill, M. J. 1960 Note on the swimming of slender fish. *Journal of Fluid Mechanics* **9**, 305–17.

Liu, H. F., Luo, X. Y. & Cai, Z. X. 2011 Stability and energy budget of pressure-driven collapsible channel flows. *Journal of Fluid Mechanics* **705**, 348–70.

Liu, H. F., Luo, X. Y., Cai, Z. X. & Pedley, T. J. 2009 Sensitivity of unsteady collapsible channel flows to modelling assumptions. *Communications in Numerical Methods in Engineering* **25**, 483–504.

Love, A. E. H. 1944 *A treatise on the mathematical theory of elasticity*. Dover Publications.

Low, K. H. 2006 Locomotion and depth control of a robotic fish with modular undulating fins. *International Journal of Automation and Computing* **4**, 348–357.

Luo, X. Y., Cai, Z. X., Li, W. G. & Pedley, T. J. 2008 The cascade structure of linear instability in collapsible channel flows. *Journal of Fluid Mechanics* **600**, 45–76.

Luo, X. Y. & Pedley, T. J. 1995 A numerical simulation of steady flow in a 2-d collapsible channel. *Journal of Fluids and Structures* **9**, 149–74.

Luo, X. Y. & Pedley, T. J. 1998 The effects of wall inertia on flow in a two-dimensional collapsible channel. *Journal of Fluid Mechanics* **363**, 253–280.

Luo, X. Y. & Pedley, T. J. 2000 Multiple solutions and flow limitation in collapsible channel flows. *Journal of Fluid Mechanics* **420**, 301–24.

Lynch, K. 2011 *Development of a 3-D Fluid Velocimetry Technique based on Light Field Imaging*. PhD Thesis, Auburn University.

Man, S. G. K., Phillips, A. B., Boyd, S. W., Blake, J. I. R. & Griffiths, G. 2012 Bio-inspired aquatic flight propulsion system for agile and manoeuverable underwater vehicles. In *OCEANS, 2012 - Yeosu*.

Marzo, A., Luo, X. Y. & Bertram, C. D. 2005 Three-dimensional collapse and steady flow in thick-walled flexible tubes. *Journal of Fluids and Structures* **20**, 817–35.

Maxworthy, T. 1972 The structure and stability of vortex rings. *Journal of Fluid Mechanics* **51**, 15–32.

Mohseni, K. 2004 Zero-mass pulsatile jets for unmanned underwater vehicle maneuvering. In *AIAA 3rd "Unmanned Unlimited" Technical Conference, Workshop & Exhibit*.

Mohseni, K. 2006 Pulsatile vortex generators for low-speed maneuvering of small underwater vehicles. *Ocean Engineering* **33**, 2209–2223.

Mohseni, K., Ran, H. & Colonius, T. 2001 Numerical experiments on vortex ring formation. *Journal of Fluid Mechanics* **430**, 267–82.

Moslemi, A. A. 2010 *Propulsive efficiency of a biomorphic pulsed-jet underwater vehicle*. PhD Thesis, Southern Methodist University.

Moslemi, A. A. & Krueger, P. S. 2009 Effect of stroke ratio and duty cycle on propulsive efficiency of a pulsed jet underwater vehicle. In *38th AIAA Fluid Dynamics Conference*.

Moslemi, A. A. & Krueger, P. S. 2010 Propulsive efficiency of a biomorphic pulsed-jet underwater vehicle. *Bioinspiration & Biomimetics* **5** (3), 036003.

Moslemi, A. A. & Krueger, P. S. 2011 The effect of reynolds number on the propulsive efficiency of a biomorphic pulsed-jet underwater vehicle. *Bioinspiration & Biomimetics* **6** (2), 026001.

Muggeridge, K. & Hinchey, M. J. 1992 A new jet propulsion device for small subsea robots. In *Proceedings of the 1992 Symposium on Autonomous Underwater Vehicle Technology, 1992. AUV '92.*.

Müller, M. O., Bernal, L. P., Miska, P. K., Washabaugh, P. D., Chou, T.-K. A., Parviz, B. A., Zhang, C. & Najafi, K. 2001 Flow structure and performance of axisymmetric synthetic jets. In *AIAA 39th Aerospace Sciences Meeting & Exhibit*.

Müller, M. O., Bernal, L. P., Moran, R. P., Washabaugh, P. D., Parviz, B. A., Chou, T.-K. A., Zhang, C. & Najafi, K. 2000a Thrust performance of micromachined synthetic jets. In *AIAA Fluids 2000 Conference*.

Müller, M. O., Bernal, L. P., Moran, R. P., Washabaugh, P. D., Parviz, B. A. & Najafi, K. 2000b Micromachined acoustic resonators for microjet propulsion. In *AIAA 38th Aerospace Sciences Meeting & Exhibit*.

Nawroth, J. C., Lee, H., Feinberg, A. W., Ripplinger, C. M., McCain, M. L., Grosberg, A., Dabiri, J. O. & Parker, K. K. 2012 A tissue-engineered jellyfish with biomimetic propulsion. *Nature Biotechnology* **30** (8), 792–7.

Nichols, J. T. 2011 *The Effect of Vehicle Configuration on the Performance of Pulsed Jet Propulsion*. PhD Thesis, Southern Methodist University.

Nichols, J. T. & Krueger, P. S. 2012 Effect of vehicle configuration on the performance of a submersible pulsed-jet vehicle at intermediate reynolds number. *Bioinspiration & Biomimetics* **7** (3), 036010.

Nichols, J. T., Moslemi, A. A. & Krueger, P. S. 2008 Performance of a self-propelled pulsed-jet vehicle. In *AIAA 38th Fluid Dynamics Conference and Exhibit*.

Ohba, K., Sakurai, A. & Oka, J. 1989 Self-excited oscillation of flow in collapsible tube. IV (laser doppler measurement of local flow field). *Tech. Rep.* 31. Kansai University.

Ohba, K., Sakurai, A. & Oka, J. 1997 Laser doppler measurement of local flow field in collapsible tube during self-excited oscillation. *JSME International Journal, Series C* **40** (4), 665–70.

Olcay, A. B. & Krueger, P. S. 2008 Measurement of ambient fluid entrainment during laminar vortex ring formation. *Experiments in Fluids* **44**, 235–247.

Pereira, F. & Gharib, M. 2002 Defocusing digital particle image velocimetry and the three-dimensional characterization of two-phase flows. *Measurement Science and Technology* **13**, 683–694.

Petrich, J. 2009 *Improved Guidance, Navigation, and Control for Autonomous Underwater Vehicles: Theory and Experiment*. PhD Thesis, Virginia Polytechnic Institute and State University.

Petrich, J., Neu, W. & Stilwell, D. 2007 Identification of a simplified auv pitch axis model for control design: Theory and experiments. In *OCEANS 2007*, pp. 1–7.

Petrich, J. & Stilwell, D. J. 2010 Model simplification for auv pitch-axis control design. *Ocean Engineering* **37** (7), 638 – 651.

Polsenberg Thomas, A., Burdick, J. & Mohseni, K. 2005*a* An experimental study of voice-coil driven synthetic jet propulsion for underwater vehicles. In *OCEANS, 2005. Proceedings of MTS/IEEE*, pp. 923–7.

Polsenberg Thomas, A., Milano, M., G'Sell, M. G., Fischer, K. & Burdick, J. 2005*b* Synthetic jet propulsion for small underwater vehicles. In *Proceedings of the 2005 IEEE International Conference on Robotics and Automation*.

Prandtl, L. 1952 *Essentials of Fluid Dynamics: With Applications to Hydraulics, Aeronautics, Meteorology and other Subjects*. Hafner.

Rayner, J. M. V. 1979a A vortex theory of animal flight. Part 2. the forward flight of birds. *Journal of Fluid Mechanics* **91**, 731–63.

Rayner, J. M. V. 1979b A new approach to animal flight mechanics. *Journal of Experimental Biology* **80**, 17–54.

Rayner, J. M. V. 1988 Form and function in avian flight. *Current Ornithology* **5**, 1–66.

Reynolds, W. C., Parekh, D. E., Juvet, P. J. D. & Lee, M. J. D. 2003 Bifurcating and blooming jets. *Annual Review of Fluid Mechanics* **35**, 295–315.

Rosen, M. W. 1959 Water flow about a swimming fish. *Tech. Rep.* NOTS TP 2298. U.S. Naval Ordance Test Station. (also MS Thesis, UCLA).

Rosenfeld, M., Rambod, E. & Gharib, M. 1998 Circulation and formation number of laminar vortex rings. *Journal of Fluid Mechanics* **376**, 297–318.

Ruiz, L. A. 2010 *The role of unsteady hydrodynamics in the propulsive performance of a self-propelled bioinspired vehicle*. PhD Thesis, California Institute of Technology.

Ruiz, L. A., Whittlesey, R. W. & Dabiri, J. O. 2011 Vortex-enhanced propulsion. *Journal of Fluid Mechanics* **668**, 5–32.

Saffman, P. G. 1995 *Vortex Dynamics*. Cambridge University Press.

Sakurai, A., Ohba, K., Futagami, Y. & Tsujimoto, M. 1996 The effect of longitudial tension on flow in collapsible tube. *JSME International Journal, Series B* **39**, 361–367.

Serchi, F. G., Arienti, A. & Laschi, C. 2013 Biomimetic vortex propulsion: Toward the new paradigm of soft unmanned underwater vehicles. *IEEE/ASME Transactions on Mechatronics* **18** (2), 484–93.

Shadden, S. C., Dabiri, J. O. & Marsden, J. E. 2006 Lagrangian analysis of fluid transport in empirical vortex ring flows. *Physics of Fluids* **18**, 047105.

Shariff, K. & Leonard, A. 1992 Vortex rings. *Annual Review of Fluid Mechanics* **24**, 235–79.

Siekmann, J. 1962 On a pulsating jet from the end of a tube, with application to the propulsion of certain aquatic animals. *Journal of Fluid Mechanics* **15** (03), 399–418.

Singer, J., Arbocz, J. & Weller, T. 1998 *Buckling Experiments: Experimental Methods in Buckling of Thin-Walled Structures, Vol. 1*. John Wiley & Sons, Inc.

Spedding, G. R., Rayner, J. M. V. & Pennycuick, C. J. 1984 Momentum and energy in the wake of a pigeon (*Columba livia*) in slow flight. *Journal of Experimental Biology* **111**, 81–102.

Stewart, P. S., Heil, M., Waters, S. L. & Jensen, O. E. 2010 Slostube and slamming oscillations in a collapsible channel flow. *Journal of Fluid Mechanics* **662**, 288–319.

Stewart, P. S., Waters, S. L. & Jensen, O. E. 2009 Local and global instabilities of flow in a flexible-walled channel. *European Journal of Mechanics B/Fluids* **28**, 541–57.

Tadesse, Y., Brennan, J., Smith, C., Long, T. E. & Priya, S. 2010 Synthesis and characterization of polypyrrole composite actuator for jellyfish unmanned undersea vehicle. In *Proc. SPIE 7642, Electroactive Polymer Actuators and Devices (EAPAD) 2010*.

Tadesse, Y., Villanueva, A., Haines, C., Novitski, D., Baughman, R. & Priya, S. 2012 Hydrogen-fuel-powered bell segments of biomimetic jellyfish. *Smart Materials and Structures* **21**, 045013.

Taylor, G. K., Nudds, R. L. & Thomas, A. L. R. 2003 Flying and swimming animals cruise at a strouhal number tuned for high power efficiency. *Nature* **425**, 707–11.

Tian, X., Iriarte-Diaz, J., Middleton, K., Galvao, R., Israeli, E., Roemer, A., Sullivan, A., Song, A., Swartz, S. & Breuer, K. 2006 Direct measurements of the kinematics and dynamics of bat flight. *Bioinspiration & Biomimetics* **1**, 10–18.

Valdivia y Alvarado, P., Chin, S., Larson, W., Mazumdar, A. & Youcef-Toumi, K. 2010 A soft body under-actuated approach to multi degree of freedom biomimetic robots: A stingray example. In *2010 3rd IEEE RAS and EMBS International Conference on Biomedical Robotics and Biomechatronics (RioRob)*.

Villanueva, A., Smith, C. & Priya, S. 2011 A biomimetic robotic jellyfish (robojelly) actuated by shape memory alloy composite actuators. *Bioinspiration & Biomimetics* **6**, 036004.

Wang, Y., Wang, Z. & Li, J. 2011 Initial design of a biomimetic cuttlefish robot actuated by sma wires. In *2011 Third International Conference on Measuring Technology and Mechatronics Automation (ICMTMA)*.

Weihs, D. 1977 Periodic jet propulsion of aquatic creatures. *Fortschr. Zool.* **24**, 171.

Whittaker, R. J., Heil, M., Boyle, J., Jensen, O. E. & Waters, S. L. 2010*a* The energetics of flow through a rapidly oscillating tube. part 2. application to an elliptical tube. *Journal of Fluid Mechanics* **648**, 123–53.

Whittaker, R. J., Waters, S. L., Jensen, O. E., Boyle, J. & Heil, M. 2010*b* The energetics of flow through a rapidly oscillating tube. part 1. general theory. *Journal of Fluid Mechanics* **648**, 83–121.

Whittlesey, R. W. 2011 Wake-based unsteady modeling of the aquatic beetle *Dytiscus marginalis*. *Journal of Theoretical Biology* **291**, 14–21.

Wood, R. J. 2008 The first takeoff of a biologically inspired at-scale robotic insect. *IEEE Transactions on Robotics* **24**, 341–7.

Wu, T. Y.-T. 1961 Swimming of a waving plate. *Journal of Fluid Mechanics* **10**, 321–44.

Yamaki, N. & Otomo, K. 1973 Experiments on the postbuckling behavior of circular cylindrical shells under hydrostatic pressure. *Experimental Mechanics* **13** (7), 299–304.

Yeom, S.-W. & Oh, I.-K. 2009 A biomimetic jellyfish robot based on ionic polymer metal composite actuators. *Smart Materials and Structures* **085002**.